Departamento de Física de la Materia Condensada
Universidad Autónoma de Madrid.

Wiring economy in the first step of visual processing in *Drosophila melanogaster.*

Memoria de Tesis doctoral presentada ante la Facultad de Ciencias,
de la Universidad Autónoma de Madrid, por

Marta Rivera Alba

para la obtención del título de Doctora
en el programa de Doctorado Oficial en Biofísica.

Trabajo dirigido por el

Dr. Gonzalo García de Polavieja Embid
Científico Titular del Consejo Superior de Investigaciones Científicas.

Trabajo tutorizado por el

Dr. Raúl Guantes Navacerrada
Profesor Contratado Doctor de la Universidad Autónoma de Madrid.

Madrid, Mayo de 2011.

A Mijuanchi, a mis padres y a Hope.

Agradecimientos

En primer lugar quiero agradecer a mi director de tesis Gonzalo García de Polavieja haberme dado la oportunidad de hacer la tesis con él en su laboratorio. También quería agradecer a Mitya Chklovskii y a todo su grupo y concretamente a Shiv Vitaladevuni y a Shinya Takemura el haberme acogido como una más desde el primer día. También quiero dar un agradecimiento especial a Ian Meinertzhagen por compartir sus conocimientos conmigo y a Zhyuan Lu por su increíble trabajo. También como no, a Aljoscha Nern por compartir imágenes, inquitudes y largas charlas conmigo. Y por último, un cariñoso agradecimiento a toda la gente de FIJI y TrakEM2 especialmente a Albert Cardona e Ignacio Arganda-Carreras por toda su ayuda.

Agradezco también a los viejos y nuevos miembros del labo en Madrid Sara (mil veces gracias), Amanda, Bea, Alfonso, Ángel, Robert y Julián (al final os voy a echar de menos), del Nicolás Cabrera Pablo, Paloma, Javi, Raúl, Marisela, Silvia, Ricardo, Judith y Marta (a vosotros os echo de menos ya) por todos esos momentos juntos de risas y por todo el apoyo que me habéis dado en todos estos años y a la gente del Cajal por acogernos tan bien. Y a toda la gente de Janelia por estar siempre pendiente de mis visitas y por atenderme tan bien: Steffi, Satoko, Christen, Amanda, Andy, Eric, Steffen, Shinya, Jasper, Sara, Marcos, Eugenia, Sergi... (thank you guys, you really made it easier).

Un besazo también a todos mis amigos del pueblo que, aunque son muchos, les va a encantar ver su nombre así que ahí van: Alicia, Alejandra, Noelia, María, Laura, Merce, Esther, Sagrario, Isa, Raquel, Sandra,

Quique, César, Edu, Álvaro, Javi, Ricky, Pedro, Fabián y Sergio. Gracias luqueros por puliros tan siertería. (¿Será esta la primera frase en gacería en una tesis?)

Agradecimiento muy especial por aguantarme a mi compañeros de la carrera Carmen, Elsa, Elena, Arturo, Fer, Elena y Javi (Mates). Y todo el resto de la gente que se van incorporando a mi vida para quedarse espero que muchos años Miguel, Ainhoa, Rodrigo, Christelle, María José, Merche Hernando, Javi, Casco, Marco, Manso, Davi, Vicky, Jaime, Ana, Lucía, Isa y Álvaro. También un beso muy fuerte para Manolo, Teresa, Carmen, Miguel, David, Paloma, Gumer y los pequeños Manolito (que ya no es tan pequeño), Diego y Óliver por esos dibujos tan maravillosos que me han hecho me hacen y me harán.

Agradecimientos a mi familia, a mis padres, a mi abuela, a mis tíos y a mis primos, por el amor incondicional que sólo la familia sabe darte. Y a Juan para el que cualquier cosa que pueda decir va a ser poqui.

A todos, gracias.

Summary

The analysis of the anatomy of the nervous systems is the description of the organization and connectivity of the neurons and it is crucial in order to understand the function and dynamics of the nervous systems. Traditionally, anatomical studies described how the nervous systems are organized, but only a few tried to explain why they are how they are. The economy laws of matter, volume and conductance time, that were proposed by Santiago Ramón y Cajal more than a century ago [1], tried to explain the anatomy of the nervous systems. This theory is simple: nervous systems are organized in functional structures that, at the same time, tend to minimize the total volume, the matter used and the conductance time of nerve impulses. Despite its simplicity, this theory has so far only been tested on a few systems [2–11] because the anatomical data necessary was only available for these sytems. Therefore, in order to be able to apply the optimization theory of the nervous systems, we decided to obtain our own anatomical data of a subunit – cartridge – in the *Drosophila melanogaster* lamina.

The *Drosophila* optic lobe is organized into several distinct layers of processing. Lamina is the first step in the visual processing in optic lobes

and it consists of many repeated subunits called cartridges. Each cartridge receives information from a point in the panorama and processes it almost independently [12]. In total, lamina is composed of around 750 cartridges. Each one receives branches from around 30 different neurons [13, 14]. The cartridges in *Drosophila* have a cylindrical shape of approximately 6 microns in diameter and 25 microns high. Therefore, they have a suitable size to be reconstructed with the present techniques in a reasonable time [15]. Using a semi-automatic reconstruction protocol from serial section transmission electron microscopy [16] we were able to obtain a complete reconstruction of a lamina cartridge in *Drosophila melanogaster*. This reconstruction includes, for the first time, the positions and shapes of all the cells contained in a cartridge. Apart from that, the connectivity of the cells and the positions of the synapses are also described.

In order to test the optimization theory on the cartridge reconstruction, we have developed our own theoretical paradigm. Given the actual sizes and connectivities of the neurons, we have calculated the configuration in the lowest local minimum of the cost function and we have compared it to the experimentally obtained one. As the number of possible configurations is too high for an exhaustive analysis of the cost function we used a heuristic iterative algorithm that we initiated in the actual configuration and that explores the configuration space to converge in a local minimum. In our paradigm we have approximated the cartridge by its 2 dimensional representation by projecting the neurons on a plane. The paradigm searched for the lowest local minimum of a sum of pairwise cost functions established between each pair of neurons. These functions include an attractive term proportional to the number of synapses between the neurons. The higher

the number of synapses the stronger the attraction. In addition, to avoid the optimal trivial solution where all the neurons have collapsed into one point, which is not physically meaningful, we included a repulsive term in the functions. This repulsive term is introduced in this study for the first time and depends on the size of the neurons such that two different neurons can not occupy the same position in space.

In order to compare the lowest local minimum found when initiating the algorithm in the actual configuration to the rest of local minima of the cost function, we initiated the algorithm in 240 different configurations and obtained 240 final configurations in different local minima. Among all of them, the configuration with least cost is the one initiated in the experimental configuration. In addition, this was also the closest to the experimental configuration. In other words, the actual configuration resembles most the lowest local minimum found. In addition, by perturbing the experimental system we show that the two main influential anatomical features are the relative sizes of the neurons and the general structure of the connectivity, but no the specific number of synapses.

In order to improve the model we have adapted it from 2 to 3 dimensions. Due to the high quality of our reconstruction we could identify three horizontal layers in the cartridge. Each layer was projected on a different horizontal plane and these planes were connected through their common neurons. Ideally, we could use as many layers as we wanted, but this would increase the complexity of the calculation. To test that the 3 layers approximation is meaningful, we checked that the connectivity inside each layer was homogeneous and different from layer to layer. Then, we applied the heuristic algorithm to the three layers, connecting them vertically by their

common neurons. The configuration in 3D in the lowest local minimum was also found to be similar to the actual configuration of the neurons. This is the first 3 dimensional wiring economy model. We showed that the configuration in each layer is controlled by the relative sizes of the neurons, their connectivity and, also, by their own vertical consistency.

Resumen

El análisis de la anatomía de los sistemas nerviosos es la descripción de la organización y conectividad de las neuronas y es indispensables para lograr entender la función y la dinámica de los sistemas nerviosos. Tradicionalmente, los estudios anatómicos describen cómo son los sistemas nerviosos pero muy pocos estudios se preocupan de porqué son como son. Las leyes de economía de volumen, materia y tiempo de conducción propuestas por Santiago Ramón y Cajal hace más de un siglo [1] intentan explicar el porqué de la anatomía de los sistemas nerviosos. Esta teoría es simple: establece que los sistemas nerviosos tienden a organizanizarse en estructuras funcionales que, al mismo tiempo, tienden a minimizar el volumen total, la materia utilizada y el tiempo de conducción del impulso nervioso. A pesar de su simplicidad, esta teoría solo se ha podido aplicar a unos pocos sistemas nerviosos [2–11] dado que solo se poseen datos anatómicos de estos sistemas. Por ello, para poder aplicar la teoría de optimización de sistemas nerviosos, decidimos obtener nuestros propios datos anatómicos de una subunidad o cartucho de lámina en *Drosophila melanogaster*.

El lóbulo óptico de *Drosophila melanogaster* está organizado en diferen-

tes etapas de procesamiento. Lámina es el primer centro de procesamiento visual en el lóbulo óptico y posee una estructura retinotópica cuya subunidad fundamental se llama cartucho. Cada cartucho recibe información visual de un punto del espacio y la procesa casi independientemente [12]. En total, lámina está compuesta por unos 750 cartuchos que reciben ramificaciones de unas 30 neuronas diferentes cada uno [13, 14]. Los cartuchos en *Drosophila* tienen forma cilíndrica, de unas 6 micras de diámetro y unas 25 micras de altura. Tienen, por tanto, un tamaño adecuado para poder ser reconstruidos con las técnicas disponibles actualmente y en un tiempo razonable [15]. Haciendo uso de un protocolo semi-automático de reconstrucción de sistemas nerviosos a partir de imágenes seriadas de microscopía electrónica [16], hemos sido capaces de obtener una reconstrucción completa de un cartucho en lámina de *Drosophila melanogaster*. Esta reconstrucción incluye, por primera vez, la posición y forma de todas las neuronas que constituyen un cartucho además de la conectividad y la posición de cada una de las sinapsis.

Para aplicar la teoría de optimización de cableado a la reconstrucción del cartucho hemos desarrollado nuestro propio paradigma teórico. Dados los tamaños y la conectividad real de las neuronas del cartucho, hemos calculado la configuración en el mínimo local más bajo para compararla con la real. Como el número de configuraciones posibles es demasiado grande para un análisis exhaustivo de la función de coste, hemos usado un algoritmo heurístico iterativo que hemos iniciado en la configuración real y que explora el espacio de configuraciones para converger en un mínimo local. En nuestro paradigma hemos aproximado el cartucho a una representación en 2 dimensiones al proyectar las neuronas en un plano. El paradigma

busca el mínimo local mas bajo de una superposición de funciones de coste que se establece para cualquier par de neuronas. Dichas funciones incluyen un término atractivo proporcional al número de conexiones entre dichas neuronas, de tal forma que cuánto mayor sea el número de sinapsis entre ellas más fuerte será su atracción. Para evitar la solución óptima trivial y sin sentido físico, en la que todas las neuronas colapsan en un punto, incluimos un término repulsivo en las funciones. Dicho término, original de este trabajo, depende del tamaño de cada neurona y evita que dos neuronas puedan ocupar la misma región del espacio.

Para poder comparar el mínimo local más bajo de los que hemos encontrado al iniciar el algoritmo en la configuración real con el resto de mínimos locales, hemos iniciado el algoritmo en 240 configuraciones diferentes obteniendo 240 configuraciones finales en diferentes mínimos locales. De entre todas ellas, la configuración final con menos coste es la iniciada en la configuración real. Esta configuración es además la que más se parece a la configuración real. Es decir, la configuración real se encuentra muy cercana a un mínimo local, que además es el más bajo de entre todos los obtenidos. De esta forma mostramos que el cartucho real se encuentra en una configuración de bajo cable. Además, alterando el sistema original, mostramos que los dos factores anatómicos más importantes del sistema son los tamaños relativos de las neuronas y la estructura global de la conectividad, pero no el número concreto de sinapsis entre neuronas.

Para mejorar el modelo lo hemos ampliado de 2 a 3 dimensiones. Gracias a la calidad de la reconstrucción indentificamos 3 capas horizontales dentro del cartucho. Cada capa se proyecta en un plano horizontal diferente y estos planos se conectan entre sí a través de las neuronas comunes. Idealmente,

podríamos utilizar tantas capas como quisiéramos, pero esto aumentaría enormemente la complejidad del cálculo. Para comprobar que la aproximación a 3 capas es significativa, hemos comprobado que su anatomía interna es muy homogénea y a la vez diferente de capa a capa. Entonces, aplicamos el algoritmo heurístico a las tres capas que hemos conectado verticalmente por sus neuronas comunes. La configuración de menor coste encontrada para estas 3 capas también se acerca a la configuración real de las neuronas, lo que supone el primer estudio de este tipo en 3 dimensiones. Mostramos que la configuración de cada capa está controlada por los tamaños relativos de las neuronas, por su conectividad en cada capa y además, por la consistencia vertical de las propias neuronas.

Contents

List of Figures

List of Tables

Chapter 1

Introduction

1.1 Wiring economy

Neurons are organized to set up functional neural networks, but an infinite number of neural configurations can give rise to the same neural network. Santiago Ramón y Cajal proposed more than a century ago that the nervous systems are organized following the Economy Laws of space, matter and conductance time [1]. This means that among all the possible configurations that a nervous system can adopt, evolution has selected those configurations that minimize the volume occupied, the total wire used and the conductance time of the neural impulse. Although the neural shapes influences the way that a neural impulse is transmitted inside the neurons, understanding which parts of the anatomical structure of the neurons do not depend on the neural computation, but on the Cajal's Economy Laws, will improve our knowledge about the relationship between structure and function in the

nervous systems.

In this section, we introduce some previous anatomical studies of optimization in nervous systems. We first show that the main statistical features of the neurons in the cortex minimizes the cortex volume. Also, we explain how optimal graphs reproduce the statistics of the morphology of individual neurons. Then, for more complete models, that include the neural connectivity, we show that areas in the macaque cortex, the ganglia in *C. elegans* and, even, the individual neurons also in *C. elegans* are organized in low wire configurations, for their given connectivity.

First, we discuss how the fundamental features of the cortex neurons have been shown to minimize the total physical volume [7]. The volume occupied by neurons in the cerebral cortex can be calculated as the volume occupied by their branches [7]. The most common neurons of cerebral cortex, the pyramidal neurons, have two kind of branches: dendrites that are postsynaptic and axons, that are presynaptic. The total volume of the system has been calculated for four different synthetic models of the system have been generated by changing the properties of the branches [7]:

1. Point-to-point axons: 1 synapse per axon. Each neuron sends as many axons as neurons.

2. Branching axons: Multiple synapses per axons.

3. Branching axons and dendrites: Axons and dendrites have different sizes and contact multiple neurons.

4. Branching axons and spiny dendrites: Dendrites have short transversal spines that increase the volume available to synapse them.

Assuming an all to all connectivity and for the experimental values of the radii of axons and dendrites found in the mouse neocortex only the fourth model, which is the more realistic, presents a total volume in the same order of magnitude as the actual one. The rest of the models predict a much higher volume to set up the same neural network [7]. This result suggests that three fundamental features of the cortical neurons, i.e., axons and dendrites differences, branching processes and the existence of dendritic spines minimize the total volume of the cortex. However, it must be considered that this observation is based on statistical data of the tissue. So, it is a global result and no predictions on individual neurons can be made with this kind of calculations.

More recently, to be able to explain the morphology of individual neurons it has been used a model that minimizes at the same time the cost of material and the conduction time [17]. The neurons are modelled as locally optimized graphs. The graphs grow from a root point by adding unconnected carrier points as nodes in a tree. The carrier points are connected to the node of the tree such as *total cost* is minimum. The total cost is defined by:

$$total\ cost = wiring\ cost + bf \cdot path\ length\ cost \tag{1.1}$$

where *wiring cost* is the Euclidean distance between the new node and the nodes in the graph, *path length cost* is the length of the graph from the root to the new node and *bf* is a balancing factor.

For example, we want connect the red carrier point P in Figure 1.1 to the tree. Even if node 5 is closer to P, *bf* controls if the *path length cost* would make a lower *total cost* if P is connected to node 4.

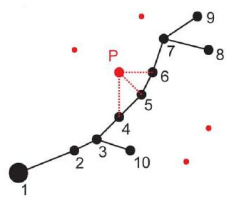

Figure 1.1: Growing an optimal graph: The carrier point P is connected to the node in the graph such that the cost (Equation 1.1) is minimum. (Modified from [17])

Thus, for the same set of homogeneous distributed carrier points (Figure 1.2), it is possible to generate different neural morphologies depending on *bf*. In general, for a low *bf*, wiring economy controls the morphology (Figure 1.2, left) creating short but slow neurons, and if *bf* is high the time conductance economy generates fast but long neurons. Therefore, the model reproduces the morphology of any neuron if the spanning field and the balancing factor (bf) are properly set. In order to do that, a set of graphs is generated for different combinations of spanning fields and *bf*. In order to choose the most realistic combination for each cell type, three parameters are compared between actual neurons and the set of graphs: total cable, mean path length and number of branching points.

Once the combination of spanning field and *bf* is chosen, the statistics of three variables between optimal graphs and actual neurons are compared [17]: branch order, path length distribution and Sholl intersections. The three of them show a good matching between optimal graphs and actual neurons. So, pure matter and time economy are able to reproduce statistical features of the morphology of individual neurons. Even more, if several

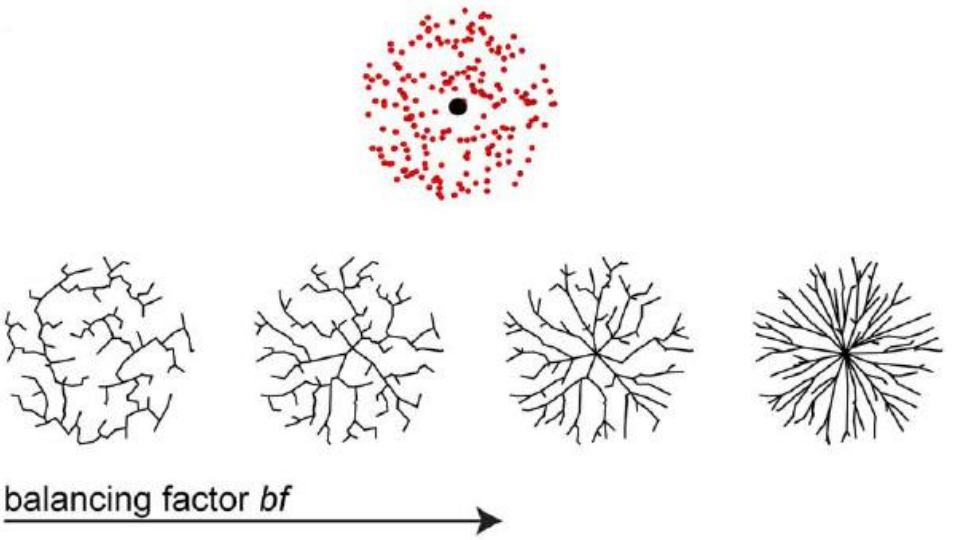

Figure 1.2: Morphology depends on balancing factor: For the same set of carrier points (top) different morphologies can been obtained when changing *bf* (bottom), from low values (left) to higher values (right). (Modified from [17])

graphs are created from several roots over the same spanning field at the same time, the algorithm reproduces the morphology of tiling neurons if adding a competition between the graphs [17].

The previous study shows that Cajal's economy law [1] explains the global morphology of individual neurons [17] without considering their connectivity, but nervous systems need to be connected to be functional. Optimization analyses of the areas in the macaque cortex, the ganglia in *C. elegans* and the individual neurons also in *C. elegans* have been done including anatomy. At a first approximation, the areas in the macaque cortex

are shown to be arranged to minimize the axon volume needed to connect them [4]. Each area of the cortex contains millions of neurons. The inter-area connectivity has been roughly described for some areas in the macaque prefrontal cortex [4] (Figure 1.3). The connectivity strength is ranked from 0 -non connection- to 3 -strong connection. As the cortex is a 2D sheet wrapping the rest of the brain, the position of the areas can be represented by the position of their centres in this sheet $\{x, y\}$. Assuming that the diameter of the axons is constant, the total axon volume is proportional to the total axon length or in other words, the distance between the areas:

$$V = \sum_{j}^{n} \sum_{i}^{n} \sqrt{(x_i - x_j)^2 + (y_i - y_j)^2} \cdot \omega_{ij} \tag{1.2}$$

where n is the total number of areas and ω_{ij} is the strength of the connection from area i to area j. As forward and reverse connections can be different, both directions are included in the calculation (Figure 1.3). When the relative positions of 11 areas in the macaque prefrontal cortex, whose interconnectivity is known (Figure 1.3), are permuted, the resulting axon volume is higher than actual axon volume. The same is true if the small and big areas are permuted independently [4]. In order to obtain configurations with less axon volume than the actual one through permutations, it was necessary to perturb the area positions a 15% for neighbouring areas and the connections strengths a 20%. This shows that the optimization of the actual configuration is fairly robust against perturbations [4].

A second way of approaching the problem is calculating the optimal configuration of the areas and comparing it to the actual one. The cost function that the system should minimize to be optimal in terms of wiring

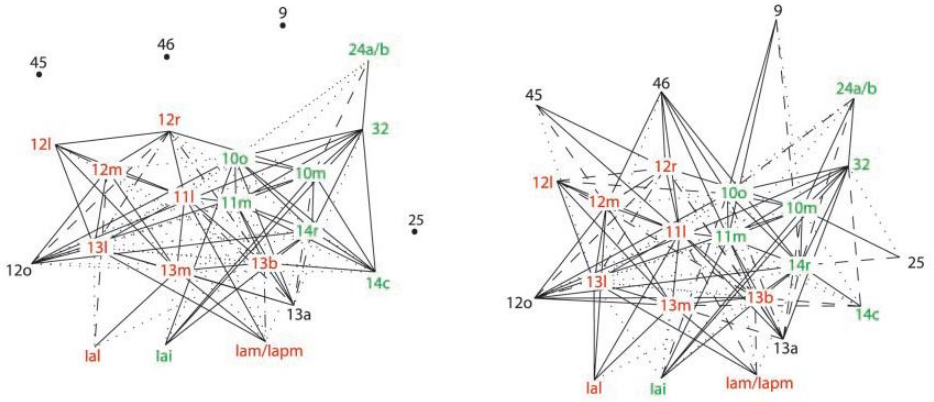

Figure 1.3: Macaque neocortex connectivity: Forward (left) and feedback (right) connections between the areas in the macaque neocortex. Connectivity strength takes 4 different values: 0 (non connected), 1 (dotted lines), 2 (dashed lines) and 3 (solid lines). (Modified from [4])

economy is unknown, one can only guess its dependence on the distance between the areas. If this dependence is quadratic it is possible to obtain an exact solvable function [8]. To avoid the trivial solution in which all the areas collapse in one point, the connections to surrounding areas are included. The surrounding areas are considered to be fixed.

The cost is given by:

$$\mathfrak{C} = \frac{1}{2}\sum_{i,j} A_{ij}(r_i - r_j)^2 + \sum_{i,j} B_{ij}(r_i - f_j)^2 \tag{1.3}$$

where A_{ij} is the number of connections between areas i and j, $\{r\}$ are the positions of the areas, B is the connectivity matrix between the areas and the surrounding fixed areas and $\{f\}$ are the positions of the fixed areas. Note that in this case the connectivity matrices are symmetrical, so A_{ij} is

the sum of the forward and reverse connections between area i and area j (Figure 1.3).

The optimal layout in matrix representation has been calculated in [8]:

$$\mathbf{r} = (\mathbf{L} + \mathbf{D_B})^{-1}\mathbf{Bf} \tag{1.4}$$

where $\mathbf{r}$ and $\mathbf{f}$ are column vectors, $D_{Bij} = \delta_{ij} \sum_k B_{ik}$ is a diagonal matrix and

$$\mathbf{L} = \mathbf{D_A} - \mathbf{A} \tag{1.5}$$

is called the Laplacian of matrix $\mathbf{A}$ where $D_{Aij} = \delta_{ij} \sum_k A_{ik}$ is a diagonal matrix. In the optimal layout, the areas in the macaque prefrontal cortex are more packed than in the actual configuration, but the optimal configurations predicts correctly their relative positions [8].

This mathematical framework can be straightforwardly applied to the *C. elegans* ganglia. *C. elegans* is a nematode whose neural connectivity is known [18]. As its long body axis is 10 times longer than its short body axis is reasonable to approximate it by a 1 dimensional animal. Its nervous system is composed of interconnected ganglia, with some dozens of neurons, that also connect to muscles and sensors. To calculate the optimal layout of their ganglia the cost (Equation 1.3) is minimized using the muscles and sensors as fixed components. The optimal layout (Equation 1.4) predicts correctly the relative positions of the ganglia in the body with the exceptions of one of them [8].

Furthermore, not only the connectivity of the ganglia in *C. elegans* nervous system is known, also the connections of individual neurons have been described [9, 18]. The 279 non pharyngeal neurons of *C. elegans* are

connected among them, to sensors and to muscles. The position of the neurons are optimized by fixing the sensors and the muscles [9]. The cost is assumed to be quadratic with the wiring length to obtain an exact solution. The model assumes one synapse per branch, but the average number of synapses per branch that connects two neurons or a muscle with a neuron is 29.3. As branches between neurons and sensors hold only 1 synapse, the total cost function for the individual neurons in *C. elegans* is:

$$\mathfrak{C} = \frac{1}{2}\frac{1}{29.3}\sum_{i,j}^{N} A_{ij}|x_i - x_j|^2 + \sum_{i,k}^{N,S} B_{ik}|x_i - s_k|^2 + \frac{1}{29.3}\sum_{i,k}^{N,M} C_{il}|x_i - m_l|^2 \quad (1.6)$$

where N, S and M are the total number of neurons, sensors and muscles respectively; A, B and C are the connectivity matrices between neurons, neurons and sensors and neurons and muscles respectively; $\{x\}$ are the position of the neurons and $\{s\}$ and $\{m\}$ are the fixed position of sensors and muscles.

By minimizing Equation 1.6 the optimal layout of the neurons is given by the following matrix equation [9]:

$$\mathbf{x} = \mathbf{Q}^{-1}[\mathbf{Bs} + \beta\mathbf{Cm}] \quad (1.7)$$

where,

$$Q_{ip} = \delta_{ij}\left(\alpha\sum_{j=1}^{N} A_{ij} + \sum_{k=1}^{S} B_{ik} + \beta\sum_{l=1}^{M} C_{il}\right) - \alpha A_{ip} \quad (1.8)$$

On average, the optimal positions of the neurons are a 9.71% of the worm body length away from the actual positions of the neurons and half of them are closer than a 5.1% of the body length (Figure 1.4) [9]. A deeper

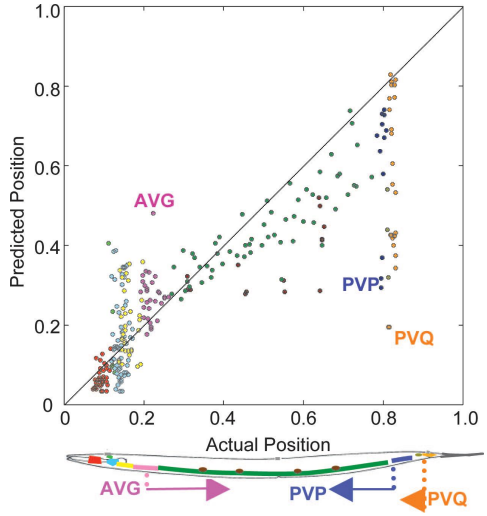

Figure 1.4: *C. elegans* actual vs. optimal configuration: each dot represents the position of each neuron in the optimal and actual 1-dimensional representation of a normalized nematode. Colours differentiate the neurons in each ganglia. AVG, PVP and PVQ are the worst predicted neurons. (Modified from [10])

analysis showed that the 84% of the *C. elegans* neuronal network is almost optimal [10]. This analysis showed that the optimal subnetwork is enough to explain the existence of ganglia and that some of the interneuron connections misplace the position of optimal neurons when they are included in the system [10].

When an optimal arrangement is compared to the actual configuration, it is found that they fit reasonably well, proving that those systems are in economical configurations, but the fit is never perfect [8–10]. Not enough evolutionary time, computational or developmental constrains or

inaccurate cost functions could be causes of this mismatching when considering a deterministic framework. However, an stochastic framework gives an explanation to this mismatching with no need of external ingredients [11]. The impact in the final cost of the neurons depends on the number of connections that those neurons have [11]. As it is shown in [11] the most connected neurons, with higher effective number of wires, have a lower deviation from the optimal configuration, $|\Delta x| = |x_{actual} - x_{optimal}|$ (Figure 1.5, left). Furthermore, if these deviations are permuted the resulting configurations have a significantly higher cost than the actual configuration (Figure 1.5, right). The data are held under the enveloping functions $1/|\Delta x|$ red line and $1/|\Delta x|^2$ dash blue line (Figure 1.5, left)[11]. This general result could be applied to other systems for which an optimization analysis can be applied [11].

Even though the wiring economy theory was proposed more than a century ago, it has only been applied to a few systems [2–11]. Despite its simplicity, an exhaustive wiring economy calculation needs an exhaustive description of the anatomy and connectivity of the nervous systems. Unfortunately, this kind of data is available only for a few nervous systems. Obtaining these data used to be a long manual process, but the recent interest on the connectivity of neural networks has promoted the automation of the process. This will give rise soon to new sets of connectivity data in different animals. We made a step forward in this direction by helping Prof. Chklovskii Lab (Janelia Farm Research Campus. HHMI. USA) to develop a semi-automatic protocol [16]. In this way, we had the opportunity to generate our own set of accurate anatomical and connectivity data of a subnetwork of the *Drosophila melanogaster* visual system. The *Drosophila*

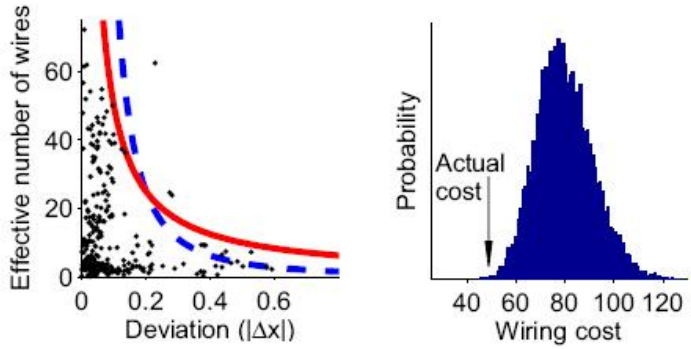

Figure 1.5: Stochastic optimization: Deviations from optimality in the *C. elegans* neurons. Left: effective number of wires vs. deviations from the optimal configuration. The higher the number of wires the lower the deviation. Red line: $1/|\Delta x|$. Dash blue line: $1/|\Delta x|^2$. Right: histogram of wiring cost of a set of synthetic nervous systems obtained by adding permuted versions of the deviation distribution to the optimal structure. (Modified from [11])

nervous system is a reasonable intermediate between the *C. elegans* nervous system and a vertebrate brain. The visual system is composed of 1500 parallel subunits that are expected to have enough evolutionary time to evolve to an optimal configuration due to their small size and high evolutionary pressure due to their high number of repetitions. The high quality of the data that we obtained allowed us to develop a new optimization framework. Our framework predicts the relative position of individual neurons, for the first time in 2 and 3 dimensions. We included, also for the first time, a repulsion component in the cost function that takes into account that the neurons occupy their own physical space. Under these assumptions, the framework does not need any external constrains to prevent the optimal

configuration of the system from collapsing into one point. The results show that the relative sizes of the neurons are as important for the final configuration as their connectivity.

1.2 Lamina: the first step in the visual processing

We are interested in the first step of visual processing in *Drosophila*, known as lamina. We first briefly introduce the *Drosophila* nervous system mainly focusing on the visual system. The *Drosophila melanogaster* brain is composed of around 200,000 neurons contained in a mm^3. It is subdivided into regions that process sensory information, like the antennal or the optic lobes, and also high processing regions, like the mushroom body or the central complex (Figure 1.6). The brain is also connected to the motor neurons in the ventral nerve cord.

The optic lobe processes in four regions (lamina, medulla, lobula and lobula plate) the visual incoming information that is captured by the photoreceptor cells in the retina. Retina is composed of around 750 subunits or ommatidia, and in each ommatidia there are 8 different photoreceptors (R1-R8). The photoreceptors can be divided in two groups: outer photoreceptors (R1-R6) and inner photoreceptors (R7-R8). The outer photoreceptors are identical and detect a broad light spectrum that makes them color blind. Lamina, the first processing centre (Figure 1.7), receives the outer photoreceptor terminals (R1-R6). In the same way that the retina is composed of 750 subunits or ommatidia, lamina is, also composed of 750 subunits or cartridges. Due to the curvature of the lens the photorecep-

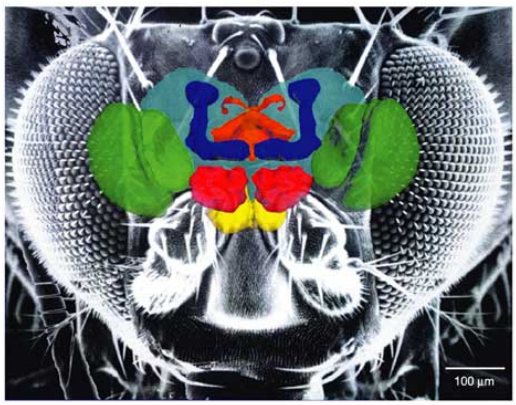

Figure 1.6: *Drosophila melanogaster* brain: *Drosophila* brain depicted on top of *Drosophila* head. The most salient neural structures are coloured and the rest are shown in light blue in the background. Green: optic lobes; yellow: suboesophageal ganglion; red: antennal lobes; blue: mushroom body and orange: central complex. (Modified from [19])

tor cells in each ommatidia do not receive light from the same point. In the region between retina and lamina the photoreceptors are rearranged in such a way that each cartridge holds a set of outer photoreceptor terminals (R1-R6) that receive light from the same point in space [12]. Thus, each cartridge processes the visual incoming information from each point in the visual panorama [12]. The inner photoreceptors (R7-R8) are sensitive to single and different colors. Medulla, the second processing centre in the optic lobe (Figure 1.7), receives the inner photoreceptor terminals [21]. The information processed in lamina and medulla is transferred to the two last processing centres in the optic lobe: lobula and lobula plate (Figure 1.7).

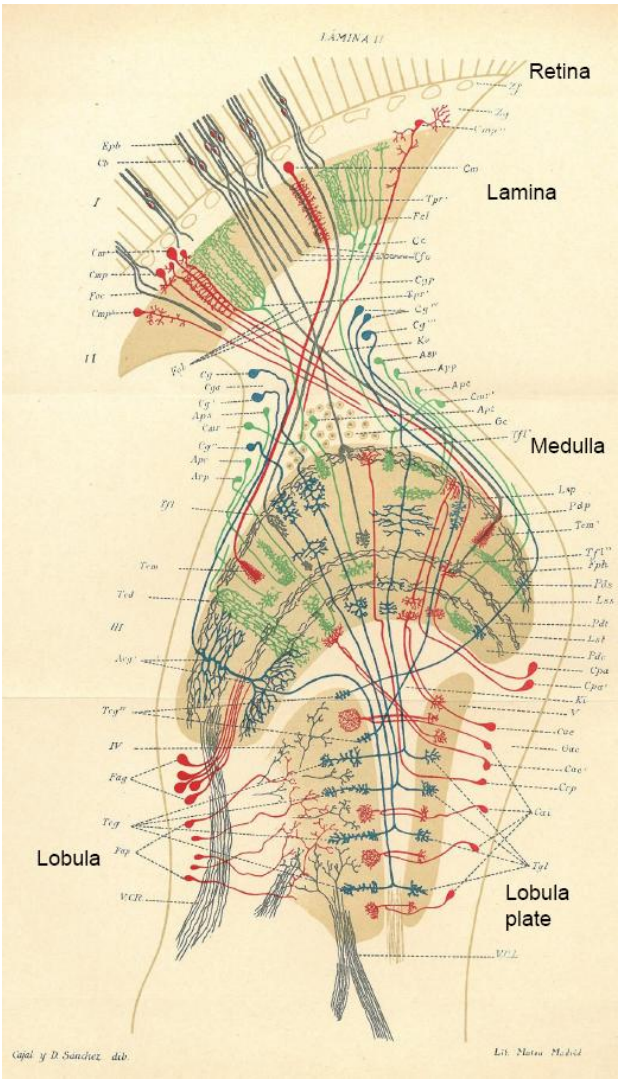

Figure 1.7: Visual system of the blue fly: Organization of the four neuropils in the insect visual systems (highlighted in yellow): Lamina, Medulla, Lobula and Lobula Plate. From the retina (top) the photoreceptor cells (black) send axons to lamina and medulla. (Modified from [20])

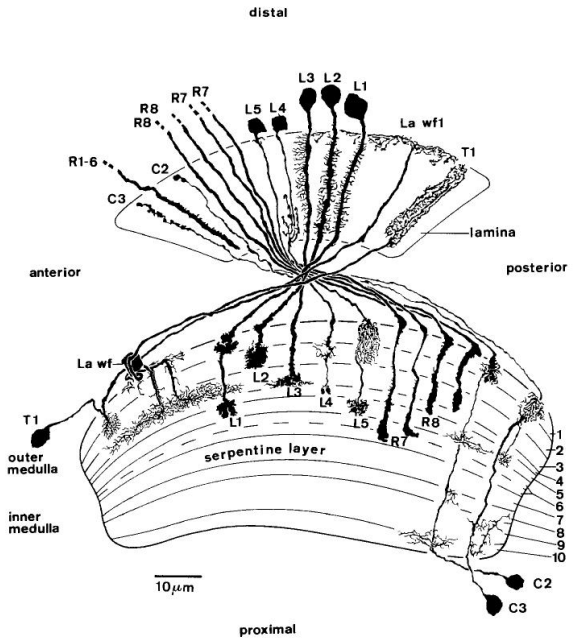

Figure 1.8: Description of the lamina and medulla neurons by Golgi staining: Arborization in lamina and medulla of most of the neurons that make synapses in *Drosophila melanogaster* lamina and that have been found with Golgi staining. (Modified from [22])

These last centres transfer the visual information to the rest of the brain.

Now that we know the general structure of the *Drosophila* visual system, we can focus on our main interest: lamina. The function of lamina is still not well described. It has been proposed to be the first step in the most basic movement detector, known as Reichardt detector [23]. However, recent studies found that the motion detection takes place in medulla [24]. Lamina has been shown to pre-process the visual information: the

synapses from the photoreceptor cells increase the signal to noise ratio [25]; the feedback connections to the photoreceptor cells serve as a system of gain control [26–28]; there is temporal derivation [29] and also, spatial processing by lateral inhibition [30]. Also, lamina is dynamically adapted to the incoming brightness [27, 28, 31]. In addition, it has been shown to split the visual incoming information in six parallel pathways carrying specific features of the visual stimuli [32, 33]: L1, L2, L3, L4, L5 and am/T1 pathways. Finally, the photoreceptors demonstrate energy-information trade-off in neural coding [34].

Lamina, as the rest of the regions, is composed of two types of cells: neurons and glia. The cartridges are surrounded and isolated from each other by a set of different glia cells [35]. Each cartridge holds branches from 12 different neuronal types. It is known that each cartridge holds 6 photoreceptor terminals (R1-R6), 5 axons from lamina monopolar cells (L1-L5), 2 L4 branches coming from neighbouring cartridges (L4+x, L4-y), 3 axons from medulla neurons (T1, C2 and C3), several branches from amacrine cells [13, 14] and several branches from the Lamina wide-field cells (Lawf1 and Lawf2) [22] (Aljoscha Nern, personal communication). These neuronal types, except Lawf2, were previously described using Golgi staining [22] (Figure 1.8).

Lamina development has been the target of many developmental studies. Development of the visual system in *Drosophila* occurs in an posterior-anterior direction, in such a way that the posterior ommatidia are older than the anterior ones [36] (Figure 1.9). Photoreceptor cells differentiate at 3^{rd} instar larval stage following a particular order (Figure 1.9):

- R8 is the first to differentiate. It sends a long axon to the developing

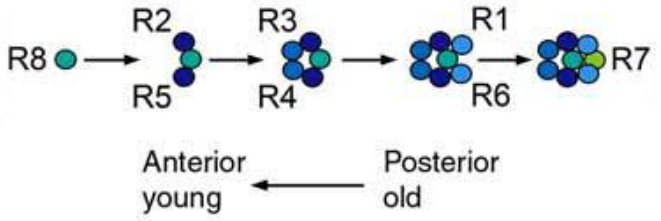

Figure 1.9: Photoreceptor development: Photoreceptor cells differentiate following the posterior-anterior direction and in an specific order: R8, R2 and R5, R3 and R4, R1 and R6 and finally, R7. (Modified from [36])

medulla that guides the growing axons of rest of photoreceptors.

- Then, the outer photoreceptors are differentiated; first R2 and R5, followed by R3 and R4, and finally, by R1 and R6 (Figure 1.9). All of the outer photoreceptors grow using R8 axon as a guide. They stop growing between two glia cells that are an intermediate target, but whose stop signal is still unknown [37, 38].

- R7 is the last photoreceptor to develop. It follows the path of R8 until the developing medulla [36].

The vast number of genetic tools in *Drosophila* makes possible an analysis of development at the single cell level. For example, if R7 is genetically transformed into an outer photoreceptor, it is, still, the last one to develop [39]. However, it stops growing where the outer photoreceptors do. Or in another example, the expression of the transcription factor Runt, normally expressed only in R7 and R8, in R2 and R5 is enough to drive all the R1-R6 to the developing medulla [39]. These two experiments show that the order of development does not indicate the layer of innervation [39].

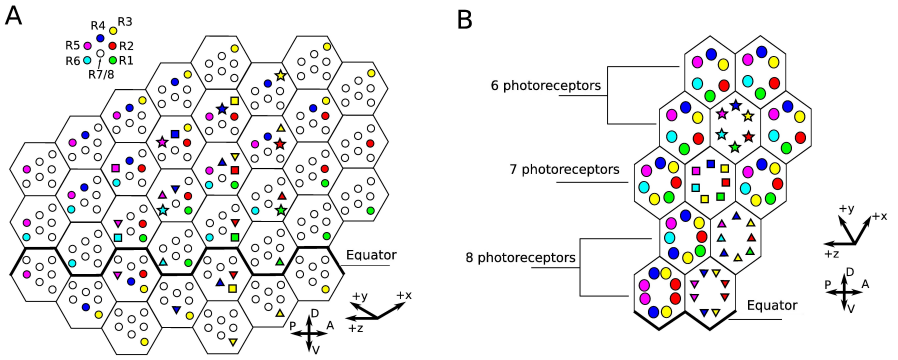

Figure 1.10: Photoreceptors sorting: A) Diagram of the retina, the photoreceptors that we have traced are coloured. The photoreceptors with special symbols: ★, ■, ▲ and ▼ receive light from the same point in the panorama and converge in the same cartridge, respectively. B) Diagram of the lamina, same colour code and symbols as in A).

R1-R6 induce the development of the lamina cells L1-L5 in 2 steps. First, they control the L1-L5 proliferation and also, their differentiation [40]. At this point in development, the cartridges already have the correct number of lamina cells L1-L5 but the photoreceptor R1-R6 are not in their final cartridges. It is during the pupal stage when R1-R6 are reorganized so the photoreceptors that receive light from the same point in the panorama collapse in the same cartridge [36]. The neural activity has been so far excluded as a possible component driving this rearrangement [41]. However, N-cadherin proteins are known to be required to regulate the R1-R6 targeting. They are thought to mediate the interaction between R1-R6 and their targets, among R1-R6 in the same bundle or between R1-R6 in different bundles [39, 42–44].

As we pointed out before, the six external photoreceptors, R1-R6, in each cartridge, receive light from the same point in the panorama, but those photoreceptors come from different ommatidia [12]. Therefore, to reach their corresponding cartridges the photoreceptors must be rearranged in their way from the retina to the lamina. Due to the curvature of the eye, around the equator more than 6 photoreptors see the same point in space. In addition, the arrangement of photoreceptors in each ommatida (Figure 1.10 A) is mirror symmetric between the ommatidia in the dorsal and the ventral sides of the eye. This organization in the eye gives rise to cartridges with 7 and 8 photoreceptors. These cartridges are close to the lamina equator (Figure 1.10 B). In Figure 1.10 we have marked in the retina with special symbols different sets of photoreceptors that converge in different cartridges respectively: 6 photoreceptor cartridge: ★; 7 photoreceptor cartridge: ■ and 8 photoreceptor cartridges: ▲ and ▼. We have traced for the first time, these photoreceptors through our dataset of electron microscopy images. We see that all the photorecptors arrive to their correct cartridges, as it was shown before in *Calliphora* [45].

A very important component of the nervous systems is also, the connectivity among the neurons. Here, we introduce the state of the art of the cartridge connectivity. Neurons are connected through *synapses* that transfer information from a *presynaptic* neuron to the *postsynaptic* ones. The cartridge connectivity has been partially described in previous studies based on serial sections Transmission Electron Microscopy(ssTEM) [13, 14]. The total number of presynaptic sites described in these studies is 480, with 1187 postsynaptic elements, 324 of which were described as *uncertain profiles* [14]. In that description, the photoreceptors (R1-R6) are the main

	Presynaptic					
Postsynaptic	**R1**	**R2**	**R3**	**R4**	**R5**	**R6**
L1	43	44	39	39	38	43
L2	48	49	43	39	42	48
L3	7	11	5	18	19	14
Am	47	47	43	34	34	46
ep. glia	0	12	4	3	1	2
Totals	145	165	134	133	134	154
Uncertain	55	35	46	43	34	54

Table 1.1: Main postsynaptic elements in the tetrads found in a previous reconstruction: Photoreceptor cells are presynaptic, mostly through tetrads (synapses with four postsynaptic elements). Here are listed the number of contacts from the six photoreceptor cells (R1-R6) (columns) to the main postsynaptic elements in the tetrads (L1, L2, L3, Am -amacrine cells- and ep. glia -epithelial glia-) (rows). As *uncertain* were included the lacking postsynaptic elements needed to complete 4 postsynaptic elements per tetrad. (Modified from [14])

presynaptic neurons in the lamina. Their presynaptic sites were described as tetrads: synapses with 4 postsynaptic elements [46]. It was described that, in the tetrads, L1 and L2 were always present and, two out of L3 or amacrine cells or epithelial glia completed the four postsynaptic terminals [13, 14] (Table 1.1). But, in the lamina the photoreceptors are also postsynaptic cells. Up to three different cell types were described to make feedback connections to the photoreceptors in the lamina [14] (Table 1.2): L2, L4 (including L4+x and L4-y) and the amacrine cells. These feedback connections have been shown to control photoreceptors output [26] and to improve the temporal representation of the stimuli [27, 28]. When a presy-

	Presynaptic		
Postsynaptic	**L2**	**L4 (all)**	**Amacrine**
R1	1	3	11
R2	1	6	9
R3	2	4	6
R4	0	1	10
R5	1	1	5
R6	1	4	7
Total	6	19	48

Table 1.2: Feedback connections found in a previous reconstruction: Up to three different cell types (columns) were described to make feedback connections to the photoreceptors (rows): L2, L4 (includes L4 and the incoming collaterals L4+x and L4-y) and amacrine cells. (Modified from [14])

naptic neuron sends information through a chemical synapse, it releases a neurotransmitter than opens the ion channels in the postsynaptic cells. Some of the neurotransmitters in the cartridge have been described in previous studies. As an example, the photoreceptors have been described to release histamine [47] and C2 and C3 release GABA, an inhibitory neurotransmitter, in the lamina [48]. Glutamate, a common neurotransmitter, has been found in some monopolar neurons, but data to support a neurotransmitter there is less conclusive [48, 49]. Only some of the ion channels that receive the neurotransmitter in the synapses have been described. Chloride channels opened by histamine have been found in the monopolar cells that are postsynaptic to the photoreceptors [50, 51]. Therefore, at this

moment, the dynamics of the cartridge is not fully described.

Each cartridge forms a cylinder-like structure with an approximate diameter of $6\mu m$ and $25\mu m$ of depth, that is a reasonable size for a complete reconstruction with the present tools. Using a semi-automatic protocol [16] we reconstructed one cartridge in the lamina of *Drosophila melanogaster*. We improved the previous reconstruction [13, 14] by describing completely the neuronal anatomy and the connectivity of a cartridge. As some examples, we included the Lawf connectivity, we found the L5 synapses in the lamina and, contradicting previous studies, we discovered that the feedback connections from the amacrine cells to the photoreceptors are almost absent. We reported the shapes and sizes of all the neurons and the position of all the synapses. Also, this new reconstruction has allowed us to test the wiring economy theory on this anatomical structure. Based on our new description, we have shown that the cartridge is in a low wire configuration.

1.3 Nervous system reconstructions

A reconstruction of a nervous system is a complete description of the anatomy and connectivity of a neural network. This kind of description of nervous systems is a key element in understanding their function and dynamics. Despite its importance, only the nervous systems of *C. elegans* has been completed reconstructed so far [18]. Some subnetworks have been also reconstructed: part of the optic lobe of *Daphnia Magna* [52], and lamina [13, 14] and medulla [53] in *Drosophila melanogaster*.

To reconstruct a nervous system it is necessary to identify the neurons, trace them and detect their synaptic contacts. So, to reconstruct neural

circuits, such a column in the mammalian cortex, thousands of neurons need to be traced and their synapses identified. In order to reconstruct nervous systems it is necessary to deal with two very different scales at the same time: the neural scale and the synaptic scale. On one hand, a typical neuron in a cortical column can be millimetres long, and the total cable of all its processes -branches- can sum up to meters of length. In flies, typical neurons are smaller, they are 20-100 microns long, and the whole brain volume is around one mm^3. On the other hand, the synaptic proteins, the synaptic vesicles and even the presynaptic and postsynaptic profiles are not bigger than some dozens of nanometres. Thus, a satisfactory reconstruction technique must be able to resolve nanometric details in volumes of μm^3 or mm^3, that is in volumes 1,000 to 100,000 times larger.

The reconstruction techniques can be classified in two main groups; the techniques based on light microscopy and the ones based on electron microscopy:

- Reconstruction techniques based on light microscopy allow us to trace neurons through millimetres if necessary, but they have a resolution not better than 0.2 μm [15], too big to resolve synapses. Classical methods of neural staining, like the Golgi method [54], are monochrome and require sparse labelled neurons, since close labelled neurons are not distinguishable. Multi-color approaches like the *Brainbow methods* randomly express several fluorescent proteins to obtain neurons labelled with up to 100 distinguishable colors [55–58] (Figure 1.11). With these methods, multiple neurons can be labelled and identified in the same tissue. In order to describe the synapses in

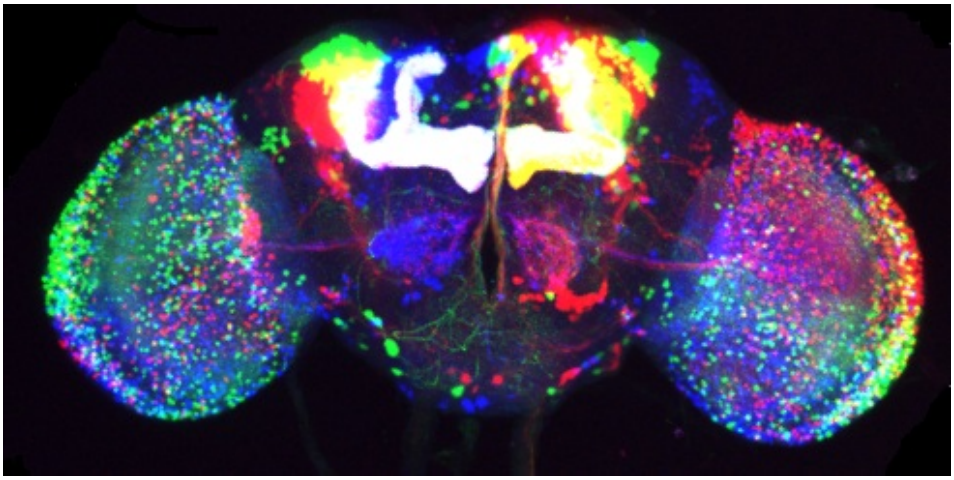

Figure 1.11: Brainbow in the *Drosophila* brain: Expression pattern of fluorescent proteins in a *Drosophila* brain obtained by crossing a OK107-GAL4 line to a UAS-dBrainbow and hsCre line [57]. (Courtesy of Stephanie Hampel)

nervous systems, some studies in vertebrates have tried to infer the connectivity network from the shapes of the neurons [59–61]. They assumed a synaptic contact when a physical contact exits. However, some other studies revealed that this technique is inefficient [62], as not all membrane contacts hold synapses. To solve this, new promising techniques that stain with fluorescence proteins the synaptic contacts between two cells have been recently developed [63, 64].

- The techniques based on electron microscopy (EM) have, in principle, enough resolution to describe the synapses, ($2nm$) but tracing long neurons is challenging [15]. Typically, the membranes are stained

with a heavy metal, that makes them look dark in the EM images, in contrast to the intracellular and extracellular spaces that look much lighter. After staining, the tissue is sectioned and then imaged. In the classical Transmission Electron Microscopy (TEM), electrons go through the tissue. Therefore, tissue must be manually cut in thin sections, 40-100 nm, that are separated from the block before taking the images. As a consequence, sections may present folds or tears that reduce their quality. Some new techniques have successfully automated this sectioning process [65]. Other new methods are based in Scanning Electron Microscopy (SEM) [66, 67], in those cases, the sections are not extracted from the tissue, instead, the block of tissue is imaged by collecting the reflected electrons. Then, a thin layer of tissue is erased from the top of the block and the next image is taken. Consequently, the tissue is lost after imaging.

Once the images have been taken, they are computationally analysed. The neurons are segmented in the images, that is, the parts of the images belonging to each cell must be properly identified and labelled (Figure 1.12). The real bottleneck of the reconstruction process from EM images is the segmentation of the images. This process has been traditionally manual and consequently very time consuming; for example, the complete nervous system of *C. elegans* took 15 years to be completed [18]. With the digitalization of the EM images many new attempts of automating the segmentation process are appearing [16, 68, 69]. Although the automatic protocols still need a manual proofreading of the automatic reconstruction, the time invested in the segmentation has been significantly reduced [16].

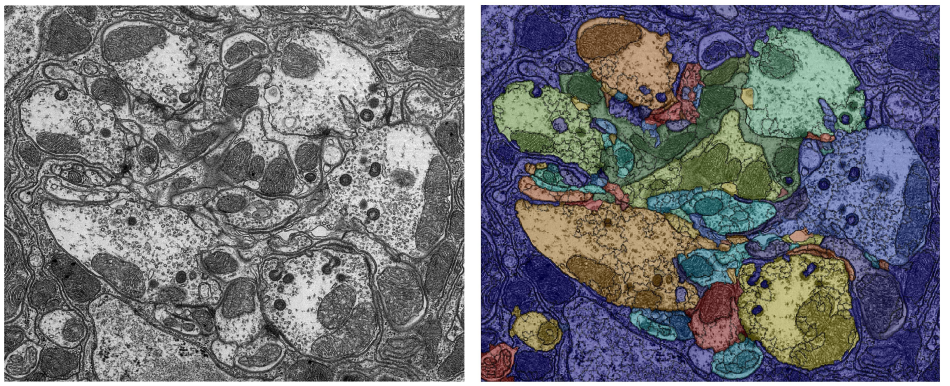

Figure 1.12: Original and segmented TEM image: Left: original TEM image of a cartridge in *Drosophila*. Right: the same image where the cells have been segmented and artificially colour labelled.

Despite the new automatic protocols, the reconstruction of large neural networks like a mammalian brain is still unfeasible. Although some pieces have been already reconstructed, the largest has only $162\mu m^3$ [62]. Not even the reconstruction of small brains, like *Drosophila melanogaster* brain, can be achieved in a reasonable time. However, smaller subnetworks in those small brains, like a *Drosophila* cartridge in lamina, are, as we have proved, a reasonable and productive goal.

Chapter 2

Cartridge reconstruction

2.1 Introduction

Describing the anatomy of nervous systems is crucial for understanding their function. Despite its importance, the complete anatomical description of the nervous systems is still a major challenge in modern neuroscience. The first attempts to describe the anatomy of the nervous systems are as old as neuroscience itself. In fact, the birth of the modern neuroscience is related to Santiago Ramón y Cajal's neuron doctrine [1], the description of the neurons as individual entities, in detriment of the reticular theory defended by Camillo Golgi [54]. Thus, modern neuroscience was born as a pure anatomical discipline [70].

Neurons are interconnected through *synapses*. Synapses can be chemical or electrical, and both transfer information from one *presynaptic* neuron to one or more *postsynaptic* neurons. Therefore, anatomical description of

nervous systems is not complete until it includes, apart from the shapes of the neurons, their connectivity. However, obtaining an accurate reconstruction of a complete nervous system in a reasonable amount of time is a problem not yet resolved.

A common approach to describe nervous systems is to use transmission electron microscopy (TEM) or more precisely, the classical serial sections TEM (ssTEM) [61, 71, 72], even though new approaches have been recently developed [15, 73–75]. Some neural networks have been described using this technique, for example: the complete neuronal system of *C. elegans* [18], parts of the optic lobe of *Daphnia magna* [52] and lamina [13, 14] and medulla [53] of *Drosophila melanogaster*. The process is in principle simple but technically complicated. First, the tissue is fixated and manually cut in sections thinner than one μm. Then, the sections are stained with a heavy metal, that creates a contrast in the TEM images.

Once the images have been taken, they are computationally analysed. In this analysis, the images are segmented by associating each group of pixels to the corresponding neuron. The image segmentation has been a manual paintstacking process for decades and is still the bottleneck of all reconstructions protocol. As an example, *C. elegans* reconstruction took around 15 years and it was done manually [18]. The efforts on automating the segmentation reduce the manual intervention and speed up the process [68, 76, 77]. The time inverted in the image segmentation is one of the main reasons for the low number of systems reconstructed so far.

In this work, we used a semiautomatic protocol that includes automatic image segmentation and automatic alignment. Although the protocol needs a manual proofreading of the automatic output [16], the reconstruction

process is speeded up with the automation.

Choosing the tissue to reconstruct is also important. With the available tools it is not possible to reconstruct complete nervous systems, besides very small ones like *C. elegans* nervous system [18], but it is possible to reconstruct small subnetworks, smaller than 200 μm^3. In vertebrates, even if there is some degree of organization like the cortical columns [78], the networks are thought to be very different from animal to animal. Therefore, in order to understand the fundamental features of the networks, these networks should be reconstructed in multiple individuals. Unfortunately, a single column in a single individual is already too large to be reconstructed (5 million μm^3), this makes unfeasible to reconstruct several columns in different animals to obtain a meaningful description of the neural networks. On the contrary, invertebrates are believed to have highly repetitive nervous systems. Thus, a single individual is representative of the whole population. Nowadays, it is not possible to reconstruct, for example, a whole *Drosophila* brain in a reasonable amount of time, but it is possible at least to reconstruct brain subnetworks.

We have chosen to reconstruct a *cartridge* of the lamina in *Drosophila melanogaster*. The visual processing in *Drosophila* is done in the *optic lobes*, which are composed of four neuronal centers or *neuropiles*. The first neuropil is lamina, which presents a retinotopic structure with approximately 750 units called cartridges [22]. Each cartridge receives the incoming visual information from one point in the panorama [12]. The cartridges process in parallel that information. Lamina offers many advantages to the reconstruction:

- It contains only around 30 neurons with a preferred direction, which is very convenient for TEM imaging.

- The cartridge is anatomically isolated which allows us to keep completeness even if we are not reconstructing a complete network. Since we want to analyse the structure of the cartridge in terms of the wiring economy theory this is specially convenient. The isolation of the cartridge allowed us to explain its anatomical structure without adding external constraints, that were necessary to be added for other tissues in previous studies [2–11].

- A previous reconstruction exits [13, 14], giving us the opportunity to study the improvement in the method done by the automation.

In this chapter we summarize the complete dataset of images used in the reconstructions (§2.2). We present the results of the reconstruction of a cartridge in the *Drosophila melanogaster* lamina using a semi-automatic protocol (§2.3.1). In §2.3.2 we explain the reconstruction protocol that we used and we introduce all the cells held in a cartridge, showing their 3-dimensional reconstructions. In §2.3.3 we show the synaptic contacts in the cartridge, studying their spatial distribution. We also studied the connectivity matrix and we show its main features (§2.3.4). As a partial and manual reconstruction already existed [13, 14], we compare our results with it (§2.3.5). Finally, we discuss our results presented and summarize our conclusions in this chapter (§2.4).

Region	**thickness** (nm)	**# sections**	**# images**	**resolution** ($nm/pixel$)	**area** (mm^2)
CBL	70	255	9180	8.68	0.0094
Lamina	40	749	26964	6.2	0.0048

Table 2.1: Summary of the image data set: Two regions have been cut and imaged: the cell body layer (CBL) (the region between retina and lamina) and the lamina itself. *Thickness* is the section thickess; *# sections* is the number of sections cut in each layer; *# images* is the total number of images taken (for each section 36 tiled images are taken in 6x6 montages); *resolution* is the image resolution; *area* is the approximated area imaged in each section assuming a 10% overlap of the tiled images.

2.2 The set of images

All the studies presented in this thesis correspond to the same image series of the left eye of a female Oregon-R fly. Tissue preparation, cutting and imaging were done in Janelia Farm Research Campus (HHMI) by their TEM facility members and collaborators. The fly's brain was fixated with Osmium-Thiocarbohydnizide-Osmium (OTO): 1% osmiun 20min at 4°C, 1% thiocarbohydnizide 15min at room temperature and 2% osmium 30min at 4°C. After fixation the tissue was cut in thin sections using a microtome. The sample was cut from the *basal membrane* – the end of the retina – until the *external chiasma* – the end of the lamina. From the basal membrane until the *lamina cortex* -the beginning of the lamina- the sections are cut at 70 nm thickness, resulting on 250 serial sections. From now on we will refer to this region as cell body layer (CBL), because most of the cell bodies of the lamina neurons are placed in this layer. The lamina itself is cut at 40

nm resulting on 749 serial sections. Thus, we have two different thicknesses for the two different regions that we studied, CBL and lamina. In CBL we manually traced 83 photoreceptors terminals in their way from retina to lamina and in the lamina we reconstructed one of the cartridges §2.3. After cutting, the sections are poststained with uranyl acetate (10min) and lead citrate (5min) in order to stain the membranes and to obtain contrast in TEM images.

Taking as a reference an specific cartridge, to cover approximately the same area in each section, it was possible to image all the sections with a transmission electron microscope at 80kV in a FEI T20 microscope, assisted by the microscope automation software *Leginon* [79]. Leginon allows to image larger areas of the sections by taking slightly overlapping tiles to make montages. In our case, and for all the sections, we took 6x6 montages of images, that is, 36 images per section with an approximate 10% overlap. The two regions were imaged at different resolutions: CBL was imaged at 8.68 $nm/pixel$ covering a total area of around 0.0094 mm^2 per section and lamina was imaged at 6.2 $nm/pixel$ with a total covered area of 0.0048 mm^2 per section. Thus, the total image data set is composed of 36144 images. All these details about our images are summarized in Table 2.1. Tissue preparation and section cutting were performed by Zhiyuan Lu and imaging was done by Shin-ya Takemura at Janelia Farm Research Campus (HHMI), Ashburn (VA, USA). We contributed to the cutting and imaging process by selecting the regions of interest, the section thickness and the image resolution.

CBL contains the cell bodies of the lamina monopolar cells, the branches of the Lamina tangential neurons (*Lat*) [22], the photoreceptor terminals

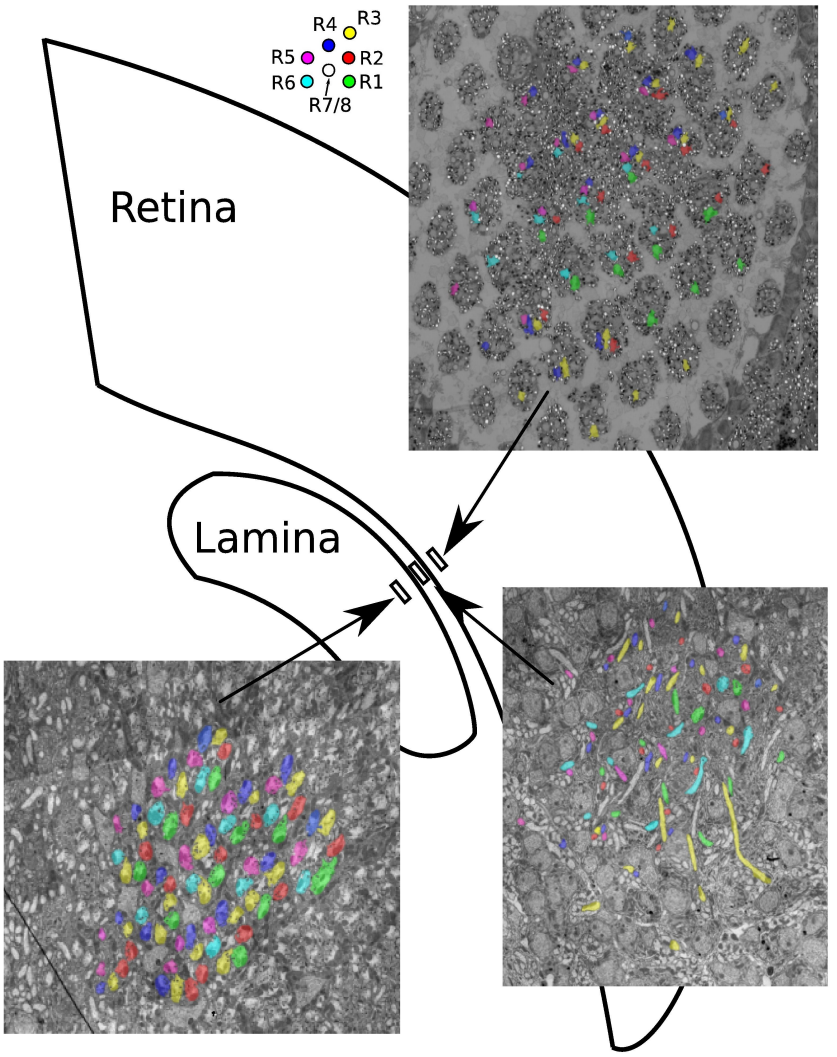

Figure 2.1: Images in the cell body layer: Photoreceptor segmentation on top of three original images corresponding to different layers: end of the retina (top), CBL (bottom right) and lamina (bottom left).

Figure 2.2: The data set includes 21 cartridges: Detail of one of the sections in the data set. Numbers show the number of photoreceptors in each cartridge. In magenta are marked the cartridges that are included completely in our data set.

[12], and up to four different glial cells [35]. As we introduced before, the cartridges around the equator of the lamina have extra number of photoreceptors. Instead of the regular number of 6 photoreceptors in each cartridge, they contain 7 or 8 photoreceptors. We have traced, for the first time in *Drosophila melanogaster*, 83 photoreceptors through the images of the CBL region (Figure 2.1).

The lamina region contains 21 complete cartridges (Fig 2.2). In order to select the cartridge of interest out of the lamina dataset, we roughly aligned the data set using the software TrakEM2 [69]. Then, we created a subset of images that contains the volume to reconstruct, including 2573 images in 628 sections. This is the stack of images that was analysed with the semiautomatic reconstruction protocol (§2.3) [16] in order to reconstruct one cartridge.

2.3 Semi-automatic reconstruction of the lamina

2.3.1 Reconstruction protocol

In order to obtain the 3-dimensional anatomy of all the neurons contained in a cartridge, we performed a reconstruction from ssTEM using a semiautomatic protocol [16] (Figure 2.3). The protocol was applied to a subset of images containing a complete 6-photoreceptors cartridge of the dorsal side of the lamina (see §2.2 for more details). Automatic alignment and segmentation are applied to the images to create an automatic 3D reconstruction. In order to generate fiducial 3D reconstructions, it is necessary to align the images with the aim of recovering, as much as possible, the original arrangement of the tissue. The protocol performs two different

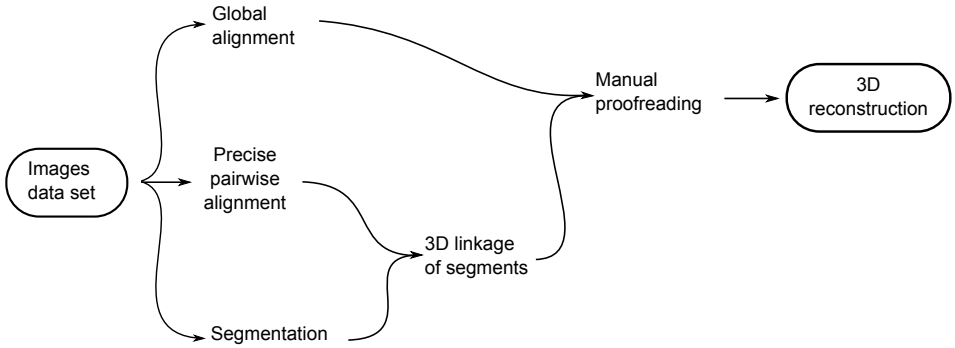

Figure 2.3: Diagram of the reconstruction protocol: Summary of the semi-automatic reconstruction protocol [16] from the images data set to the 3D reconstruction.

alignments: a very precise pairwise to be used in the segmentation process and a rough global alignment to be used in the manual proofreading. The segmentation process consists on labelling each pixel in the images as part of each cell. This protocol performs a 2-step segmentation. In the first step the images are segmented in superpixels – groups of pixels that belong to the same cell with a high confidence. The algorithm that generated theses superpixels was based on the watershed algorithm, known to over-segment the images. The second step links the superpixels in 2D – intra-section – by an iterative agglomerative algorithm that merges superpixels until a given threshold is reached [16]. Then, segments are linked in 3D – inter-section – by an algorithm based only in the overlapping areas using the precise pairwise alignment, to create 3D bodies.

After the automatic processing, we performed a manual proofreading of the automatic output by using a specific software called Raveler [80].

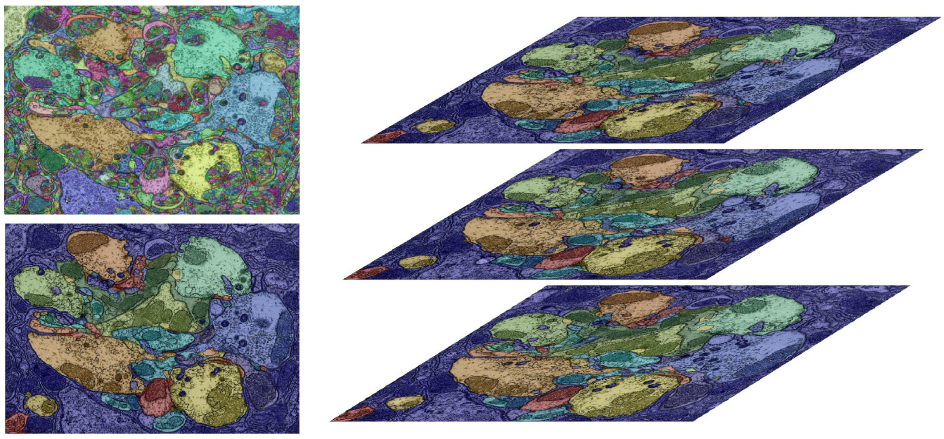

Figure 2.4: Manual proofreading: Left: segmentation before (top) and after proofreading (bottom). Right: Example of segmentation of neurons in 3 consecutive sections of a cartridge. The labels are kept from section to section to generate the 3-dimensional volumes of the reconstruction.

As the images were typically over-segmented, Raveler allowed us to link the segments belonging to the same cells just by clicking on the images. In order to facilitate this process Raveler artificially coloured the segments already linked with the same color. In Figure 2.4 it is shown an example of the same image, as it it shown by Raveler, before and after proofreading and an example of 3 consecutive sections after this manual proofreading. The output of the proofread dataset is visualized with 3D-viewer [81] to be able to identify the cells that have been reconstructed (Figure 2.5). We identified each cell type by comparing them with the Golgi staining studies [22] and with a previous manual reconstruction from ssTEM [14].

Based on previous studies [14, 22] (Figure 2.6) the cartridge has been

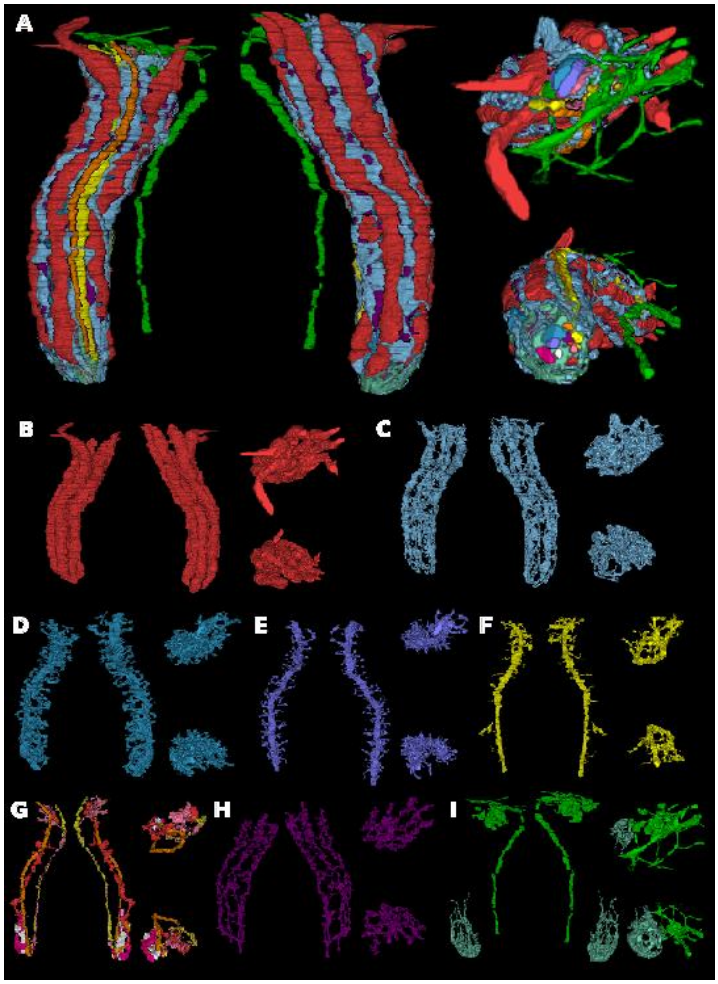

Figure 2.5: 3D reconstruction: For all the panels (left) front view; (center) back view; (top right) top and (bottom right) bottom views of all the cells reconstructed. A) All the neurons reconstructed. B) Photoreceptor cells. C) Amacrine cells. D) L2. E) L1. F) L3. G) L4 (orange), L5(yellow), C3 (dark orange), C2 (light pink), L4+x (dark pink) and L4-y (white). H) T1. I) Lawf cells (yellow green) and marginal glia (light green).

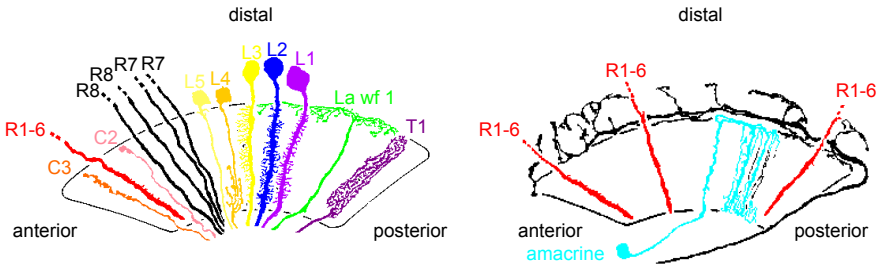

Figure 2.6: Lamina cells: Golgi staining of the lamina cells. The color code is the same as in Figure 2.5 and Figure 2.7. (Modified from [22])

described to have a straight shape. Although we could recognize all the cells held in the cartridge, the S-shape obtained in our reconstruction (Figure 2.5) was not consistent with these previous descriptions. Cutting and imaging are not perfect and any issue in those steps generates eventual errors in the image alignment. For example: during cutting, the knife is not always perfectly parallel and during imaging, dusts, folds or tears in the sections generates artefacts in the images. Therefore, the true shape of the tissue remains unknown since the alignment process is not perfect. As other techniques keeps better the actual shapes of the neurons we re-aligned our reconstruction to recover a straight shape of the cartridge. We divided the part of the cartridge that contains synapses (sections 14-613, see §2.3.3) in groups of 50 sections. We defined the center of the cartridge for each group by using the presynaptic sites of the photoreceptors. We vertical aligned those centres resulting on a straight reconstruction (Figure 2.7).

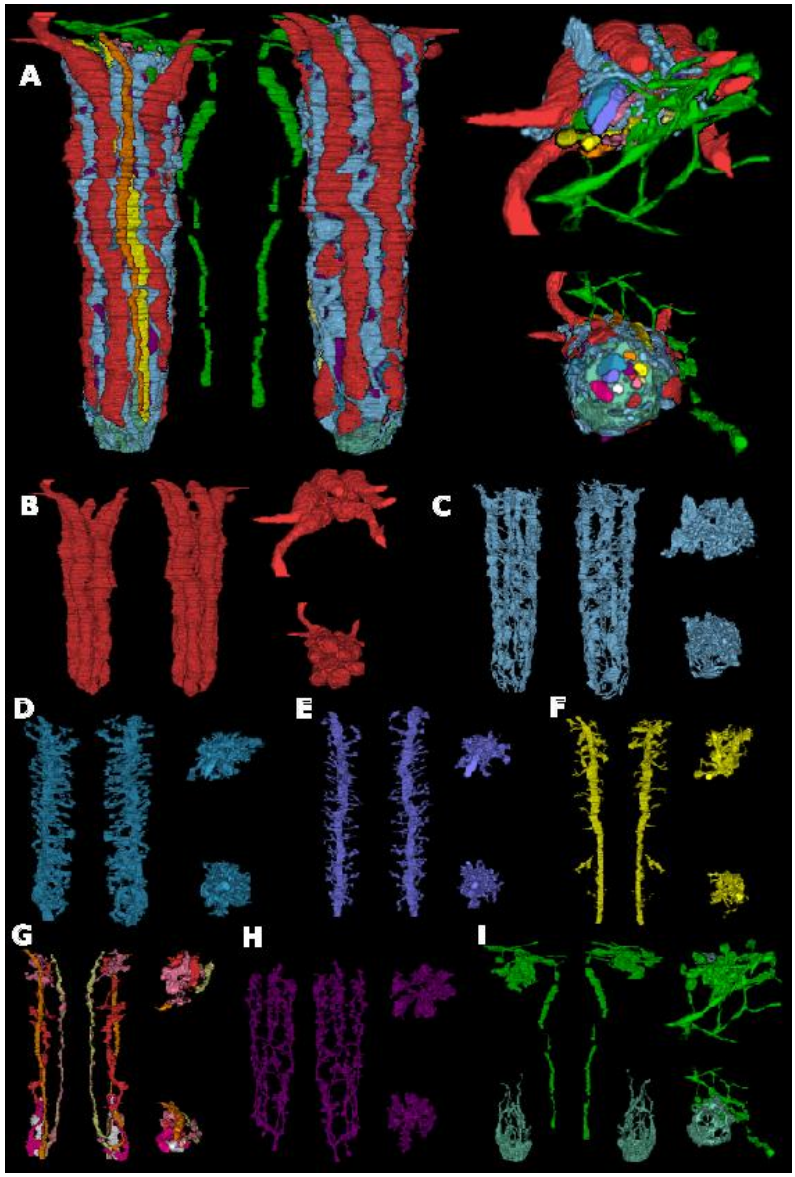

Figure 2.7: 3D reconstruction smoothly aligned: Same color code and labelling as in Figure 2.5.

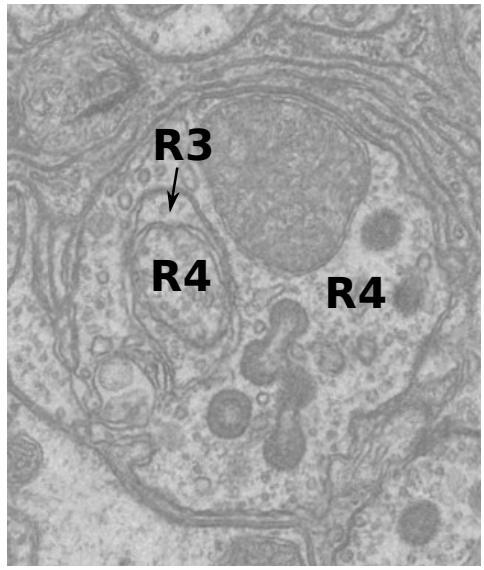

Figure 2.8: Example of the photoreceptor invaginations: R3 has invaginated R4 and then R4 has invaginated the R3 invagination.

2.3.2 Neuronal shapes

Cartridges are almost independent networks that process the visual incoming information in parallel, in such a way that each cartridge processes the information from a different point in the panorama. In *Drosophila melanogaster*, a regular cartridge is composed of 6 photoreceptors terminals (R1-R6), 5 lamina monopolar cells (L1-L5), 3 medulla cells (T1, C2 and C3), several branches of amacrine cells (am), several branches of Lamina wide field cells (Lawf) and 2 incoming collateral branches for neighbouring L4 cells (Figure 2.6). Cartridges are surrounded by different glial cells [35]: *satellite glia* (distal), *epithelial glia* (center) and *marginal glia* (proximal).

Tables 2.2, 2.3, 2.4, 2.5, 2.6 and 2.7 summarize the mean area, mean perimeter and position of the segments belonging to the neurons that we have reconstructed. That means that if one neuron has two separated branches in one section, both branches contribute independently to the mean area and perimeter. With this, the mean area and perimeter listed represent the mean branch size that is the meaningful data for dynamical studies or for comparison with fluoresce images. The neurons identified in our reconstruction can be classified as follows: outer photoreceptors, lamina monopolar cells, amacrine cells, medulla cells in lamina, lamina wide-filed cells and marginal glia. In the following we describe their main features:

Outer photoreceptors

The outer photoreceptors terminals (R1-R6) carry the achromatic visual information to the lamina. The photoreceptors in a cartridge receive light from the same point in the panorama, as we have already described. Photoreceptors have the thickest profiles within the lamina and are organized in an external ring in each cartridge. Their profiles have an homogeneous size all the way through the lamina and they end in the proximal part of the lamina (Figure 2.7 B). In Table 2.2, where we show the most important features of the photoreceptors that we have extracted from the reconstruction of the photoreceptors, we can see that they have similar sizes and lengths. From previous studies it is known that the cross section of the protoreceptors can vary up to a 40% depending on the time of the day and this variability is believed to control de coding efficiency [82, 83]. The photoreceptors invaginate each other in such a way that the host photoreceptor invaginates the invagination and so on up to 5 or 6 times. As a

Cell	area (μm^2)	perimeter (μm)	sections
R1	1.4 ± 0.7	6.1 ± 2.2	$1 - 580$
R2	1.2 ± 0.5	5.6 ± 1.7	$1 - 615$
R3	1.2 ± 0.5	5.7 ± 1.5	$1 - 628$
R4	1.2 ± 0.5	5.6 ± 1.9	$1 - 606$
R5	1.4 ± 0.8	5.9 ± 2.3	$1 - 586$
R6	1.6 ± 0.7	6.4 ± 2.2	$1 - 587$

Table 2.2: Photoreceptor data: mean and standard deviation of the area and perimeter of all the 2D segments belonging to each cell and interval of sections where the cells are present. Section 1 is the most distal and section 628 is the most proximal.

result, the TEM images present concentric profiles inside photoreceptors, that actually belong to both the host and the invaginating photoreceptor (Figure 2.8). The function of these invaginations remains unknown.

Lamina monopolar cells

The Lamina monopolar cells (L1-L5) can be divided in two groups: Large monopolar cells (L1 and L2) and small monopolar cells (L3-L5) [20]. All of them have their cells bodies in the distal border of lamina [22] (Figure 2.6) and end in different layers of medulla [53].

- As we can see in figure Figure 2.7 D and E, L1 and L2 have thick axons that are centred in the cartridge and that send lateral branches, homogeneously distributed, to make or receive synapses. L2 axon and branches are thicker than the L1 ones and both cells are homogeneous

Cell	area (μm^2)	perimeter (μm)	sections
L1	0.30 ± 0.16	2.7 ± 1.0	$1 - 628$
L2	0.35 ± 0.22	3.3 ± 1.5	$1 - 628$
L3	0.27 ± 0.15	2.4 ± 0.9	$1 - 628$
L4	0.16 ± 0.11	1.9 ± 0.7	$1 - 628$
L4+x	0.29 ± 0.18	2.9 ± 1.1	$442 - 628$
L4-y	0.38 ± 0.25	3.3 ± 1.6	$438 - 628$
L5	0.07 ± 0.04	1.3 ± 0.5	$1 - 628$

Table 2.3: Lamina monopolar cell data: mean and standard deviation of the area and perimeter of all the 2D segments belonging to each cell and interval of sections where the cells are present. Section 1 is the most distal and section 628 is the most proximal.

through the cartridge length. It has been shown that their size follows a circadian rhythm [84].

- Except in the distal region, L3 tends to be outside the cartridge between R5 and R6 (Figure 2.7 F). Most of L3 branches and synapses are located in the distal part of the cartridge and its branches are almost as thick as L1 branches.

- L4 sends two collateral branches to two neighbouring cartridges, in the proximal region of the lamina. Held in our cartridge we reconstructed the local L4 axon and the two incoming L4 branches from cartridges at positions +x and -y (see Figure 2.1 B for orientation in lamina) (Figure 2.7 G). The incoming branches are as thick as L2, while the branches of the local L4 have half the size. The L4 complex has been

largely studied as a possible movement detector [23, 32, 85]. This was suggested because the L4 collaterals connect the cartridges through a network with an anterior-posterior direction. This is the same direction as the direction of the apparent movement of the panorama when flies are flying. Therefore, this is a very important movement that flies should, in principle, be able to detect. However, such a movement detector network has been recently hypothesized to be in regions involved in higher processing [24].

- Finally, L5 has very few branches mostly in the proximal part as we can see in (Figure 2.7 G). It has the smallest axon of all the lamina monopolar cells and very few horizontal branches.

In Table 2.3 the most important features of the reconstructions of the lamina monopolar cell are shown.

Amacrine cells

Amacrine cells have their cell bodies in the proximal border of the lamina. They send an axon that bypasses the lamina and that branches in the distal lamina border [22] (Figure 2.6). The amacrine branches are placed in the inter-photoreceptors regions, spatially correlated to the T1 branches. Their thin processes and their intricate structure make their Golgi staining very difficult (Figure 2.6). Each amacrine cell can be found in more than one cartridge and each cartridge has several amacrine cells. All that makes them too extensive for a complete EM reconstruction.

We reconstructed all the pieces of amacrine profiles in our volume, but with our technique, it is not possible to know how many individual cells

Cell	area (μm^2)	perimeter (μm)	sections
Ama	0.23 ± 0.17	2.4 ± 1.3	$1 - 628$
Amb	0.28 ± 0.15	2.1 ± 1.1	$1 - 628$
Amc	0.03 ± 0.03	0.7 ± 0.3	$1 - 628$
Amd	0.03 ± 0.03	0.7 ± 0.3	$1 - 628$
Ame	0.02 ± 0.01	0.6 ± 0.2	$423 - 628$
Amf	0.08 ± 0.06	1.3 ± 0.6	$373 - 628$
Amg	0.16 ± 0.14	1.9 ± 1.1	$13 - 628$
Amh	0.07 ± 0.05	1.3 ± 0.7	$18 - 63$
Ami	0.03 ± 0.02	0.7 ± 0.3	$1 - 628$
Amj	0.05 ± 0.02	1.0 ± 0.3	$580 - 628$
Amk	0.05 ± 0.06	1.1 ± 1.1	$601 - 628$
Aml	0.18 ± 0.10	2.1 ± 0.8	$1 - 628$

Table 2.4: Amacrine cell data: mean and standard deviation of the area and perimeter of all the 2D segments belonging to each cell and interval of sections where the cells are present. Section 1 is the most distal and section 628 is the most proximal.

they belong to and whether they are linked outside our volume. All the disconnected amacrine pieces found are shown in Figure 2.9 A-F and their main features are summarized in Table 2.4. Most of the pieces reconstructed have very small size and only four of them (Aml, Amg, Ama and Amb) have vertical and thick branches placed between contiguous photoreceptors.

Medulla cells in lamina

There are three medulla neurons in the lamina cartridge: T1, C2 and C3 (Figure 2.7 G and H). They have different morphologies and possibly dif-

Figure 2.9: 3D reconstructions of amacrine cells and Lamina wide-field cells: From A) to F) (left) front view; (center) back view; (top right) top and (bottom right) bottom views of all the amacrine cells reconstructed. A) All the amacrine cells. B) Aml. C) Amc (dark blue), amd (yellow), ame (cyan), amf (magenta), amh (light blue), ami (dark pink), amj (spring green) and amk (purple). D) Amg. E) Ama. F) Amb. From G) to R) (left) front and (right) back views of the Lawf cells reconstructed. G) All the Lawf cells reconstructed. H) Lawff. I) Lawfa. J) Lawfb. K) Lawfc. L) Lawfd. M) Lawfe. N) Lawfg. O) Lawfh. P) Lawfi. Q) Lawfj. R) Lawfk.

Cell	area (μm^2)	perimeter (μm)	sections
T1	0.11 ± 0.04	1.8 ± 0.4	$42 - 628$
C2	0.09 ± 0.15	1.4 ± 1.2	$1 - 628$
C3	0.19 ± 0.20	2.1 ± 1.4	$21 - 628$

Table 2.5: Medulla cell data: mean and standard deviation of the area and perimeter of all the 2D segments belonging to each cell and interval of sections where the cells are present. Section 1 is the most distal and section 628 is the most proximal.

ferent functions [22] (Figure 2.6). In lamina, T1 presents a basket shape, with longitudinal and external branches in clear correlation to the amacrine branches. The T1 branches are narrow and homogeneous all the way along the cartridge. The set T1/amacrine is believed to be an independent pathway of information to the brain [32]. C2 and C3 are centrifugal neurons that send an ascending axon to the lamina. The reconstruction features of this medulla neurons are summarized in Table 2.5. C2 axon is quite small all the way trough the cartridge, but in the proximal it has thicker branches. C3 axon thickness is variable all the way through the lamina.

Lamina wide-field cells

Lamina wide field cells (Lawf) had been Golgi stained [22] (Figure 2.6), but had never been reconstructed before (Figure 2.7 I). Their cell bodies are located in the distal medulla plexus and each of them send an ascending axon that bypasses lamina and branches in the distal region. The branches of these neurons are horizontal and reach different cartridges. The branches

Cell	area (μm^2)	perimeter (μm)	sections
Lawfa	0.19 ± 0.13	2.2 ± 1.0	$1 - 44$
Lawfb	0.24 ± 0.15	2.7 ± 1.3	$1 - 59$
Lawfc	0.41 ± 0.35	3.3 ± 1.4	$1 - 69$
Lawfd	0.12 ± 0.11	1.5 ± 0.9	$1 - 85$
Lawfe	0.30 ± 0.21	2.9 ± 1.4	$1 - 72$
Lawff	0.21 ± 0.18	2.0 ± 1.1	$1 - 550$
Lawfg	0.51 ± 0.31	3.6 ± 1.2	$1 - 58$
Lawfh	0.19 ± 0.16	2.0 ± 1.0	$1 - 48$
Lawfi	0.16 ± 0.16	1.7 ± 1.0	$1 - 77$
Lawfj	0.25 ± 0.26	2.5 ± 1.7	$12 - 104$
Lawfk	0.17 ± 0.09	2.4 ± 0.9	$1 - 25$

Table 2.6: Lamina wide-field cell data: mean and standard deviation of the area and perimeter of all the 2D segments belonging to each cell and interval of sections where the cells are present. Section 1 is the most distal and section 628 is the most proximal.

of Lawf are quite thick. Only one Lawf cell type (Lawf1) had been described so far with Golgi staining [22]. Although from light microscopy studies we could expect to find around 5 Lawf cell branches in the cartridge (Aljoscha Nern, personal communication), we have actually found 11 of them. For this reason, we propose the existence of a second Lawf cell type (Lawf 2) that also matches the last light microscopy studies in *Drosophila* (Aljoscha Nern, personal communication.). Unfortunately, we could not find any differential anatomical features to associate the branches to their corresponding cell type (Table 2.6, Figure 2.9 G-R).

Cell	area (μm^2)	perimeter (μm)	sections
Marg. glia a	0.14 ± 0.26	2.3 ± 3.5	$395 - 628$
Marg. glia b	0.19 ± 0.33	3.35 ± 4.9	$366 - 628$

Table 2.7: Marginal glia data: mean and standard deviation of the area and perimeter of all the 2D segments belonging to each cell and interval of sections where the cells are present. Section 1 is the most distal and section 628 is the most proximal.

Marginal glia

Following the nomenclature proposed in [35], the glia cell that we have reconstructed is a marginal glia. The marginal glia, reconstructed for the first time in this work, wraps the proximal part of the cartridge (Figure 2.7 I). In the proximal sections they are really thick, while they become narrower in more proximal sections. Since each marginal glia cell covers more than one consecutive cartridge (Aljoscha Nern, personal communication), the two pieces that we were able to distinguish are expected to be connected further down in the external chiasma. Both pieces have very similar sizes and shapes (Table 2.7).

2.3.3 Cartridge synapses

In this work we have manually annotated the chemical synapses included in our cartridge using the software Raveler [80]. To identify the chemical synapses in this tissue, we have used three known synaptic landmarks [86]: the presynaptic T-bar ribbon, the presence of vesicles and the apposition

of the postsynaptic cells (Figure 2.10, left). If any of these three landmarks are missing, we annotated the synapse as *uncertain*. We identified 477 synapses (57 of which are uncertain) with 1884 postsynaptic elements. For each synapse we have annotated its presynaptic and postsynaptic cells, its position and its certainty (see Appendix A for the complete dataset). The electrical synapses are not consistently annotated because they cannot be clearly identified. However, we observed two special features that could be related to electrical synapses (Figure 2.10):

- Photoreceptor terminals projected branches that contact other photoreceptors membranes suggesting a possible electrical coupling between the two cells (Figure 2.10, top-right). They have been described before in other flies [87] and in *Drosophila* [13].

- The membrane between amacrine cells and T1 is thicker and darker than the rest of the cells membranes suggesting a possible electrical coupling between the two cells (Figure 2.10, bottom-right).

Further experiments need to be done in order to be sure if these special features are actual electrical synapses or a staining artefacts. It was also described that a gap junction marker appeared to localize with L1 and L2, suggesting a possible gap junction between these two cells [88]. However, we do not distinguish any specialization in their common membrane.

Returning to chemical synapses, we found that they are organized in a ring around the center of the cartridge (Figure 2.11 A). It is thus, convenient to describe their position in polar coordinates: radius (r) and angle (ϕ). The mean radius is almost constant along the reconstruction, $1.5 \pm 0.5 \mu m$,

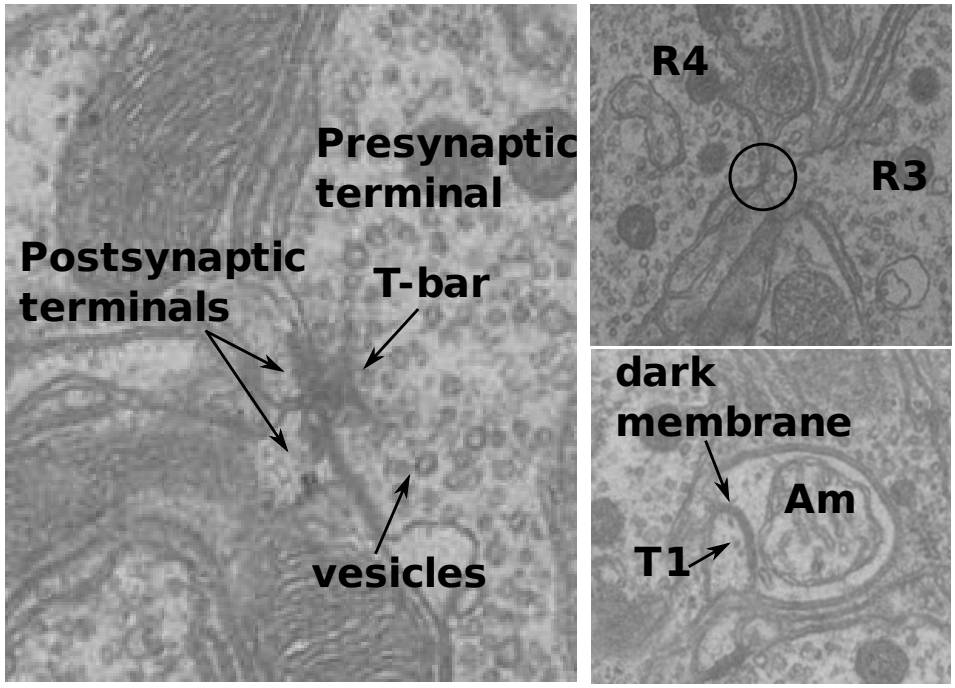

Figure 2.10: Synapses types in lamina: Left: the chemical synapses are associated to the presence of a T-bar protein and vesicles in the presynaptic terminal (covering all the right area of the image) and to the presence of postsynaptic terminals showing sometimes a postsynaptic density than can be observed in this figure. Top right: possible gap junction (circle) between R3 and R4. Bottom right: example of the dark and thick membrane between T1 and amacrine cells (Am).

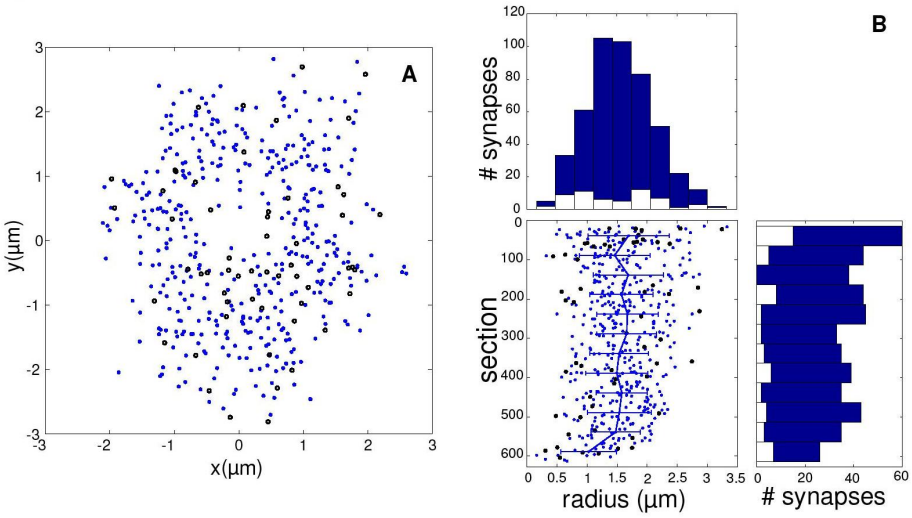

Figure 2.11: Synapses distribution: A) 2D projection of all the synaptic sites (blue dotes) and the uncertain synaptic sites (black circles). B) (Top) Histogram of radius (distance to the center of the cartridge) of all the synaptic sites (blue bars) and of the uncertain synapses (empty bars); (Bottom left) section vs. radius of all the synaptic sites (blue dotes) and of the uncertain synaptic sites (black circles); (Bottom right) histogram of the number of synapses along the cartridge (blue bars) and of the uncertain synapses (empty bars).

but there is a clear reduction in the proximal part, where the cartridge is narrower. We found no special features in the distribution of angles.

In figure Figure 2.12, we show, for each cell type, the distribution along the cartridge and the radius of the synapses. We observed that the number and distribution of synapses is different for each cell type (Figure 2.12).

- Photoreceptors are mostly presynaptic. The distribution of their synaptic sites is homogeneous along the cartridge and their synapses show a constant radius.

- L1 is only postsynaptic, its connectivity is also homogeneous along the cartridge and it synapses also show a constant radius.

- The distribution of postsynaptic sites of L2 is very similar to the distribution of L1, because both are postsynaptic to the photoreceptors in the same synapses, while the distribution of presynaptic sites of L2 is concentrated in the proximal part, to contact the L4 complex.

- L3 is only postsynaptic in lamina, it receives synapses all along the cartridge but mostly in the distal part, where we found most of its branches (Figure 2.7 D).

- L4 and the L4 collateral branches are both presynaptic and postsynaptic in the cartridge. Their synapses are located almost exclusively in the proximal part, where we found the L4 collateral branches (Figure 2.7 G).

- L5 is only postsynaptic, we found its synapses in the proximal and distal parts, but not in the central part.

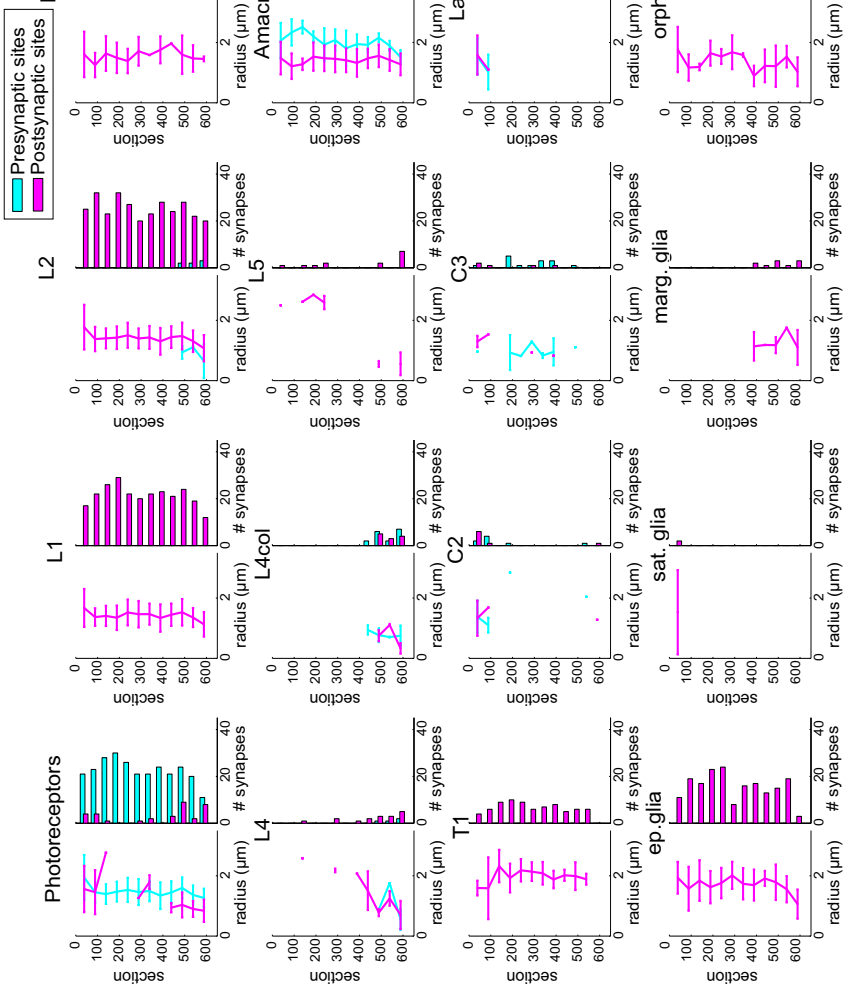

Figure 2.12: Synapses distribution for each cell type: For all the panels: presynaptic sites (cyan) and postsynaptic sites (magenta). For each cell: left: section vs. radius of all the synaptic sites and right: histogram of the number of synapses along the cartridge.

- The amacrine cells are both postsynaptic and presynaptic in the cartridge. The distribution of their synaptic contacts is not homogeneous, but their synapses are present all along the cartridge. The radii of their postsynaptic sites is lower than the radii of the presynaptic ones in the distal part of the cartridge. The synapses of the amacrine cells are the only ones showing a different radius between presynaptic and postsynaptic sites.

- T1 is only postsynaptic, its connectivity is homogeneous all along the cartridge and its synapses shows a constant radius.

- C2 presynaptic and postsynaptic sites are concentrated in the distal part. This is interesting because C2 crosses all the way through lamina, from proximal to distal, to contact preferably in the distal part.

- C3 postsynaptic sites are located in the distal part and its presynaptic sites are in the central part.

- The synaptic contacts of Lawf cells are only located in the distal part where we also found their branches.

- The glia cells are only postsynaptic in the cartridge. Each cell type receives synapses where it is present: epithelial glia all along the cartridge, satellite glia only in the distal part and marginal glia only in the proximal part.

- The small branches that we could not be assigned to any cell are called orphans. In our reconstruction the orphans are only postsynaptic and

are mostly concentrated in the distal part.

2.3.4 Cartridge connectivity

One of the most important features of a nervous system is its connectivity. Based on our annotation of synapses, we built the connectivity matrix of the cartridge. In this matrix, columns represent the presynaptic neurons and rows the postsynaptic cell (Table 2.8). We have included all the neurons in our cartridge and also the 3 glial cell types that receive synapses from the neurons in our cartridge. For visualization purposes, we have merged all the amacrine cells and all the Lamina wide-field cells as two single neurons. We also included the postsynaptic profiles that cannot be assigned to any cell and that we called orphans. We found 70 orphans out of 1884 postsynaptic elements, what represents less than 4% of the total postsynaptic profiles.

We have extracted the main features from the connectivity of the cartridge (Figure 2.13). Some of these features have already been described in the literature [13, 14] and some others are described for the first time in this work:

- L4-complex (Figure 2.13a). It is composed of L2, L4, L5 and two incoming collaterals of neighbouring L4. It is restricted to the proximal part of the cartridge, where the collaterals are present. We have included for the first time L5 in this complex, since its postsynaptic sites were not described before.

- Lawf connectivity (Figure 2.13b). Lawf synapses are placed in the distal part of the cartridge. Lawf cells are presynaptic to a variety of cells like amacrine cells, L3, the epithelial glia, C2, L2 or the photore-

	Presynaptic cell														
	R1	**R2**	**R3**	**R4**	**R5**	**R6**	**L2**	**L4**	**L4col a**	**L4col b**	**Am**	**C2**	**C3**	**La wf**	**Total**
R1	-	-	-	-	-	1 + 0	-	1 + 0	1 + 0	0 + 1	-	-	1 + 0	4 + 1	
R2	-	-	-	-	-	1 + 1	-	-	1 + 0	1 + 0	-	-	3 + 0	6 + 1	
R3	-	-	-	-	-	-	-	2 + 0	1 + 1	-	-	1 + 0	1 + 0	5 + 1	
R4	-	-	-	-	-	-	-	1 + 0	0 + 1	2 + 0	-	-	0 + 1	3 + 2	
R5	-	-	-	-	-	-	1 + 0	-	2 + 1	2 + 0	-	-	-	5 + 1	
R6	-	-	-	-	-	-	-	2 + 0	1 + 1	-	-	-	1 + 0	4 + 1	
L1	40 + 0	43 + 0	37 + 1	38 + 0	38 + 0	45 + 1	3 + 0	-	0 + 2	-	-	3 + 3	1 + 1	249 + 8	
L2	46 + 0	45 + 0	39 + 1	41 + 1	39 + 0	47 + 2	-	2 + 2	3 + 3	2 + 3	1 + 3	3 + 3	5 + 4	7 + 2	280 + 24
L3	11 + 0	10 + 0	4 + 0	8 + 0	6 + 0	12 + 1	-	-	0 + 1	1 + 0	10 + 4	-	0 + 1	17 + 4	79 + 11
L4	-	-	-	-	-	2 + 0	4 + 1	-	1 + 1	0 + 3	4 + 1	-	-	-	11 + 6
L4col a	-	-	-	-	-	-	4 + 1	-	-	0 + 1	-	-	-	-	4 + 2
L4col b	-	-	-	-	-	-	2 + 1	-	2 + 1	-	-	-	-	-	4 + 2
L5	-	-	-	-	-	-	1 + 0	1 + 1	1 + 2	1 + 1	4 + 0	0 + 1	-	1 + 0	9 + 5
Am	36 + 0	39 + 0	39 + 1	37 + 0	35 + 0	40 + 0	-	1 + 0	1 + 0	0 + 1	1 + 1	5 + 3	9 + 13	24 + 12	267 + 31
T1	-	2 + 0	2 + 0	2 + 0	-	-	0 + 1	-	-	-	54 + 9	-	1 + 1	1 + 3	62 + 14
C2	-	-	-	-	1 + 0	-	-	-	-	-	1 + 0	-	-	3 + 3	5 + 3
C3	-	-	2 + 0	-	-	-	-	-	-	-	1 + 0	-	-	2 + 0	5 + 0
La wf	1 + 0	-	-	-	-	-	-	-	-	-	-	0 + 1	-	5 + 2	6 + 3
Ep.glia	15 + 0	13 + 0	7 + 1	9 + 0	10 + 0	11 + 1	0 + 1	0 + 1	2 + 1	1 + 1	87 + 12	-	1 + 2	6 + 3	162 + 23
S.glia	1 + 0	1 + 0	-	-	-	-	-	-	-	-	-	-	-	-	2 + 0
M.glia	1 + 0	-	-	1 + 0	2 + 0	-	0 + 1	-	1 + 2	0 + 1	-	-	0 + 1	-	5 + 5
Orph.	11 + 0	6 + 0	6 + 0	8 + 1	8 + 0	8 + 1	-	2 + 2	1 + 0	1 + 1	4 + 0	2 + 2	1 + 3	12 + 6	70 + 16
Total	162 + 0	159 + 0	136 + 4	143 + 2	138 + 0	167 + 6	16 + 6	7 + 7	17 + 11	13 + 17	173 + 32	10 + 10	21 + 28	85 + 37	1247+160

Table 2.8: Connectivity matrix: The presynaptic cells (columns) make synapses in the postsynaptic ones (rows). The entries indicate certain synapses + uncertain synapses. The columns belonging to non presynaptic neurons have been omitted for visualization purposes. Amacrine and Lawf cells have been merged into single columns respectively. (see Appendix A for the complete dataset of the synapses)

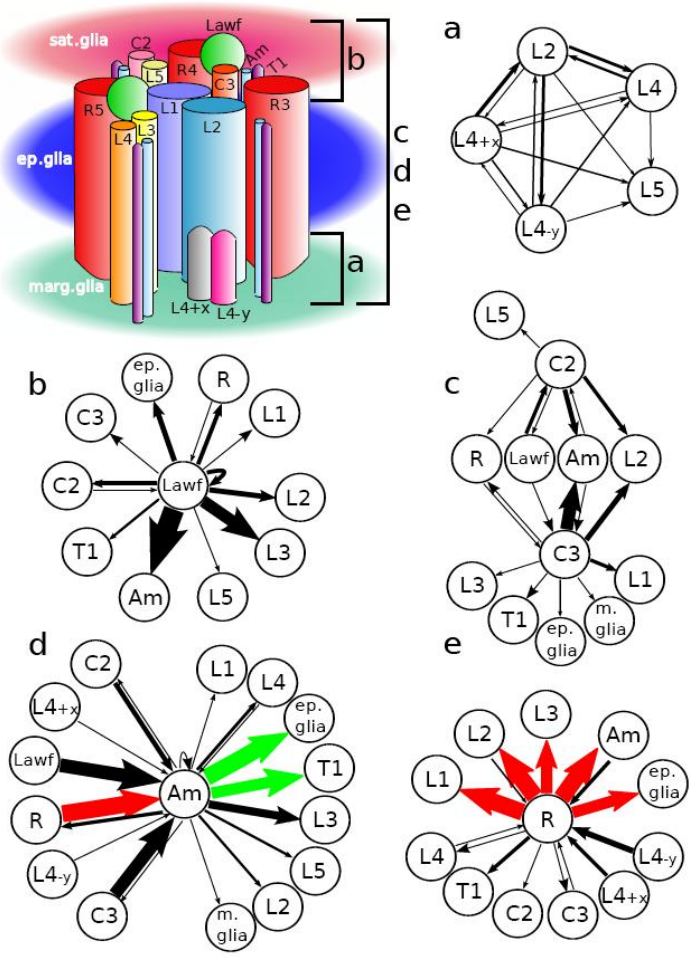

Figure 2.13: Main features of the connectivity network: Top left: Diagram of the cartridge cells, for simplicity only three photoreceptor, four amacrine branches, four T1 branches and two Lawf branches are shown. a) Connectivity of the L4-complex. b) Lawf cells connectivity. c) C2 and C3 connectivity. d) Amacrine cells connectivity. e) Photoreceptor cells connectivity. The postsynaptic cells in the tetrads are shown in the top of the scheme. The width of the arrows indicates the number of synapses, green and red arrows should be 6 and 9 times bigger than they show, respectively.

ceptors. As their connectivity had never been described before and there are not eletrophysiological or behavioural experiments in these cells, their function is unknown. But an important clue is that they are mostly presynaptic, meaning that they constitute an information input to the cartridge

- Medulla feedback (Figure 2.13c). Since, the medulla cells C2 and C3 are mostly presynaptic to the lamina, they bring feedback information from latter steps in the processing.

- The amacrine interneurons (Figure 2.13d). They should be basic for the cartridge function. This is so because although there are also other direct connections, they mediate most of the information flux, from the inputs (R, Lawf, C2, C3, and the L4 collaterals) to the outputs (L1-L5, T1, epithelial glia and marginal glia).

- Photoreceptor input and feedbacks (Figure 2.13e). Photoreceptors carry the main information input to the cartridge. Their presynaptic sites are tetrad synapses where the most common postsynaptic terminals are L1, L2, L3, amacrine cells and the epithelial glia in different combinations. In our reconstruction we showed that there were feedback connections to the photoreceptors from L2, L4, L4+x, L4-y, amacrine cells, C3 and Lawf cells. The photoreceptor with the highest number of feedback connections is R2 with 6+1 synapses, in any case a low number when compared with the mean number of tetrads 45 ± 3.7. Although the feedback connections from the amacrine cells to the photoreceptors had been described as an important feature, they are almost absent in our cartridge (Table 2.8).

In conclusion, the cartridge has a complex network. The general structure of the cartridge network presents a set of inputs: Photoreceptors, Lawf cells, C2, C3 and the L4 collaterals; a set of interneurons: the amacrine cells; and a set of outputs: L1-L5, T1, epithelial glia, marginal glia and satellite glia. Although T1 is a medulla cell, it is consider an output since it is not presynaptic in the lamina. On top of that there are feedback connections to the photoreceptors and C2 and C3 bring feedback information from deeper processing regions.

2.3.5 Comparison with previous reconstructions

A previous manual and partial reconstruction of a cartridge, also from ssTEM, has been done before in 2001 [13, 14] for a *Drosophila melanogaster* captured from the wild. In order to compare the connectivity matrix derived from this previous partial reconstruction, from now on Matrix2001, to the matrix that we have obtained, from now on Matrix2011, we overlapped both of them (Figure 2.14). Instead of showing the number of connections between the cells, we used different color codes to show the comparison. There are three possibilities for each element in the connectivity matrices:

- $Matrix2011_{ij} = Matrix2001_{ij}$: for these entries we show the number of contacts with a black to white scale. The most important features that are common to both reconstructions are: L1, L3, L5, T1 and the glia cells are not presynaptic and the photoreceptors do not make synaptic contacts with themselves.

- $Matrix2011_{ij} < Matrix2001_{ij}$: for these entries we show the difference between both matrices with a blue to green scale. The most

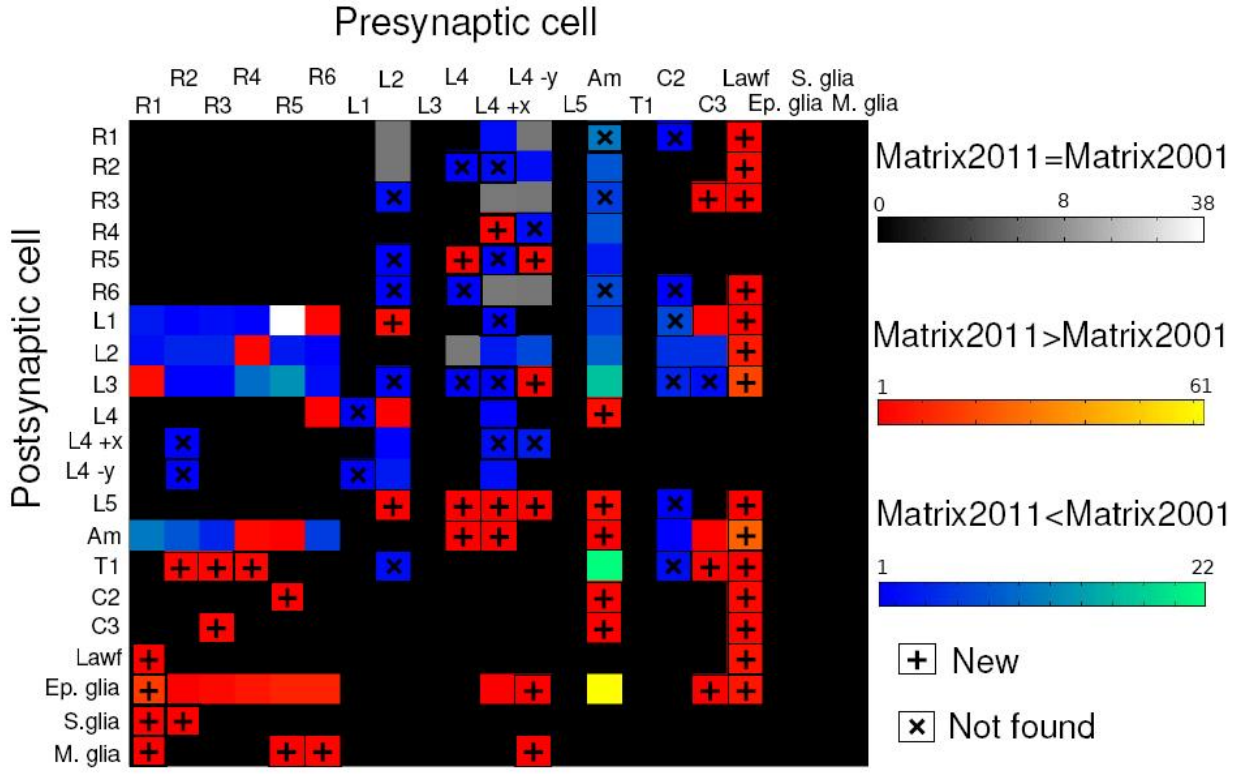

Figure 2.14: Comparison to a previous reconstruction: the two connectivity matrices are overlapping. Instead of the number of synapses three different color codes indicate the comparison: number of synapses for the entries with the same value in both matrices (black to white scale); difference in the number of synapses when $Matrix2011_{ij} > Matrix2001_{ij}$ (red to yellow scale) and when $Matrix2011_{ij} < Matrix2001_{ij}$ (blue to green scale).

important result here is that feedback connections from the amacrine cells to the photoreceptors are almost absent in our reconstruction. In the previous reconstruction these feedback connections were assumed to be very important for the function and dynamics of the cartridge [14]. In most of the cases, epithelial glia was found between the amacrine presynaptic sites and the photoreceptor terminals. Therefore, the low number of contacts from amacrine cells in our reconstruction is related to the high number of contacts between amacrine cells and epithelial glia.

- $Matrix2011_{ij} > Matrix2001_{ij}$: for these entries we represented the difference between the two matrices using a red to yellow scale. The most salient feature is the high number of synapses from amacrine cells to epithelial glia. We observed a very thin sheet of epithelial glia receiving synapses from the amacrine cells that prevents the neurotransmitter from reaching the photoreceptors. This sheet was described before [13] assuming a specialization in the glia called *gnarld*, but as we did not distinguish such a specialization (Figure 2.15), we described the glia as postsynaptic to the amacrine cells. The new type of synaptic contacts described are also important: the L5 postsynaptic sites, the connectivity of the Lwaf cells and the postsynaptic sites of satellite and marginal glia.

In broad terms, the previous reconstruction and our reconstruction are similar. As an example, the photoreceptor inputs remain the main input to the cartridge. Some features have been updated like the number of amacrine cell feedbacks to photoreceptors. The main additions are the

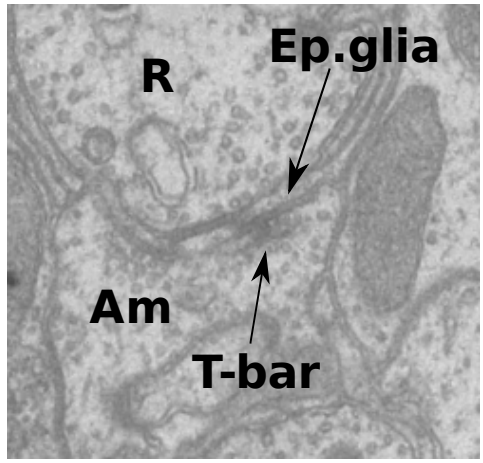

Figure 2.15: Synapse from amacrine to ep. glia: The amacrine cell (Am) makes a synapse, indicated by the T-bar. The epithelial glia (Ep. glia) prevents the neurotransmitter to reach de photoreceptor (R).

inclusion of Lawf cells connectivity and the discovery of the L5 synapses in lamina, none of them described before.

2.4 Discussion and conclusions

Accurate and detailed descriptions of nervous systems are crucial for understanding their function and dynamics. However, with the available tools it is only possible to reconstruct small subnetworks. Lamina cartridges are small subnetworks whose neurons are organized with a preferred direction, that is specially convenient for ssTEM reconstructions. This makes a cartridge a very good candidate for reconstruction.

Although a previous reconstruction of a cartridge existed [13, 14], it

lacked some features that turned out to be fundamental for our analyses: the completeness of the connectivity network, the positions of the synapses and the sizes of the neurons (§3). In this work, we were able to improve and update the previous knowledge of the cartridge connectivity. We included, for the first time, the connectivity of the Lamina wide-field cells, marginal glia and satellite glia. We also discovered the postsynaptic terminals of L5 and that the feedback synapses from the amacrine cells to the photoreceptors are almost absent. All that changes in the description of the connectivity matrix might make necessary a reinterpretation of some of the behavioural of electrophysiology data [26–28, 32] and it will give new ideas for new experiments in order to understand the system.

In invertebrates, the general structure of the connectivity of neural networks is believed to be similar among different individuals of the same species, and even of related species. But the specific number of synapses is believed not to be the same in different individuals, nor even for repetitive structures. Therefore, in order to completely understand a neural network and its general features, it is necessary to reconstruct it in different individuals and, in the case of repetitive networks, we need to reconstruct several samples of that network within the same individual. The more stereotyped the network the less number of specimens is necessary to reconstruct.

How stereotypical is the connectivity of the cartridge is still an open question, but from the comparison between an older reconstruction [14] and our reconstruction we can partially address this question. The number of synapses from photoreceptors to L1, L2 L3 and the amacrine cells is very similar in both reconstructions. The two reconstructions were done in flies of different strains, so based on this similarity we would expect these

connections to be broadly conserved from animal to animal. An example of discrepancy between both reconstructions is the connectivity of C2 and C3. Therefore, we do not expect to find stereotyped connectivity for these two cells in future reconstructions.

In order to fully address the question of how stereotypical the cartridges are, it is necessary to reconstruct more of them. The improvement in the automation of the protocol derived from our work, will speed up future reconstructions of more cartridges. That will enable us to answer questions about the synapses variability among cartridges, even for those equatorial cartridges with extra number of photoreceptors.

3-dimensional reconstruction from serial sections Transmission Electron Microscopy (ssTEM) is the most accurate and complete tool to describe the anatomy of the nervous systems. However, some issues need to be considered when using ssTEM data. The TEM imaging needs to be done in a previously fixated tissue, and the speed of the process is crucial to preserve as much as possible the original shape and connectivity of the neurons. Consequently, the reconstruction accounts for an specific moment in time of the neuron life, that means, that no dynamical information of the morphology can be address from ssTEM reconstructions. However they can serve as a basis for electrophysiological, behavioural and genetic experiments in order to fully describe the cartridge function and dynamics.

Chapter 3

Wiring economy with volume exclusion

3.1 Introduction

The nervous systems of small animals are expected to evolve under a great evolutionary pressure to be compact but functional. The pressure is even higher if we consider small flying animals like *Drsosophila melanogaster*, for which weight is an important factor. A possible way of reducing size and weight of the nervous systems keeping their functionality is by minimizing the total wire used to set up their connectivity networks. This argument is not new as it was proposed by Santiago Ramón y Cajal more than a century ago as the Economy Laws of volume, matter and conductance time [1] now renamed as the wiring economy theory. This theory proposes that among all the possible configurations that can perform the function of the system,

nervous systems tend to be arranged in configurations with minimal total wire. The wiring economy theory has been successfully applied to the areas in the mammalian cortex [2–8] and to the *C. elegans* neural network [8–11]. Despite the simplicity of this theory, for some systems, an accurate analysis at neuronal level needs a complete description of the connectivity, the size and the position of each neuron. Such kind of data is not available for any system due to the complicated and long experimental procedure to obtain them. Due to the lack of available data, we reconstructed one cartridge in the *Drosophila melanogaster* lamina (§2) to apply the wiring economy theory at the neuronal level.

As shown in §2 a cartridge in the *Drosophila melanogaster* lamina is composed of around 30 neuronal branches coming from 12 different neuronal types: photoreceptors, 5 Lamina monopolar cells (L1-L5), amacrine cells (am), 2 Lamina wide-field cells (Lawf1-2) and the medulla neurons T1, C2 and C3. Cartridges are surrounded by different glial cells [35]: *satellite glia* (distal), *epithelial glia* (center) and *marginal glia* (proximal). A cartridge is anatomically isolated and its boundaries are clear through the lamina depth. No tangential neurons are found in the lamina apart from the Lawf cells and two L4 collateral branches that send very clear branches to each cartridge and do not make synapses in their way from one cartridge to another. The anatomical isolation of the cartridge makes it a perfect candidate for a wiring economy analysis, since not external constraints are necessary to calculate low wiring configurations of the cartridge.

Wiring economy theory assumes that nervous systems have had enough time to evolve to low wiring configurations. The higher the number of elements in the system, a longer time is expected to be necessary to evolve,

and the higher the evolutionary pressure, the shorter the evolutionary time. For a cartridge, the evolutionary pressure to evolve to a low wiring configuration is thought to to be low, due to its low number of neurons. However, each lamina contains around 750 cartridges, that makes 1500 cartridges in each individual. The impact of using more wire than necessary in 1500 cartridges holding more than 20,000 neurons cannot be neglected. Thus, cartridges are expected to have had enough time to evolve to low wiring configurations due to their reduced number of neurons and a high evolutionary pressure due their large number of repetitions.

Taking advantage of the cylindrical organization of the cartridge, we projected all the neurons along the cartridge on a plane to create a 2 dimensional representation. Then, keeping the actual connectivity and sizes of the neurons we calculated the arrangement of the neurons in the 2 dimensional representation, that is in the lowest local minimum of the cost function. In order to define this optimization process it is necessary to define the cost function that is explored. As we pointed out, there are several previous studies based on wiring economy theory. Most of them needed to fix some of the components in order to prevent the optimal solution of the system from collapsing into one point. To avoid that, in our cost function we included, for the first time, an internal constraint of the system, the physical size of the neurons (§3.2).

We show that the actual cartridge configuration is close to a local minimum, which is the lowest local minimum that we have found (§3.3). We also show which are the most important features that control this arrangement (§3.4). From the analysis of a simplified model, we show some general results that could be applied to other systems (§3.5). We extended our model

from 2D to 3D. The 3 dimensional approximation is also close to a local minimum, with even less error than the 2 dimensional representation (§3.6). This is the first wiring economy 3D model. Finally, we discuss the results and summarize the conclusions (§3.7).

3.2 Cost function and optimization algorithm

Any optimization process requires a cost function to be minimized. In this work, we calculated the configuration of the neurons that minimizes the total wiring cost, for the experimental connectivity and sizes of the neurons.

In order to perform a meaningful analysis of the system with a reduced number of parameters, we took advantage of the cylindrical shape of the cartridge. We projected all the neurons on the xy plane creating a 2D representation of the cartridge. The sizes of the neuronal elements included in the calculation are defined by their radii $\{r_{i=1}^{N}\}$, assuming circular profiles $r_i = \sqrt{S_i/\pi}$ where S_i is the mean experimental area occupied by each neuronal element in all the sections. We considered the total area covered by each neuron in each section even if this area can be split in several segments.

The validity of any optimization study depends critically on the function that is optimized, called *Cost*. The cost function we have used is original for this study and includes the actual neuronal connectivity and, for the first time, the actual sizes of the neurons. With these two components and due to the anatomical isolation of the cartridge we did not need to add any external constraint to calculate a meaningful prediction of the cartridge

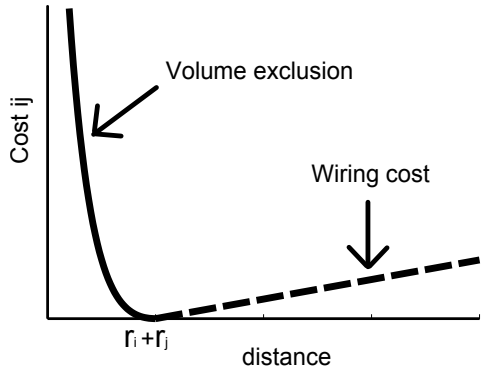

Figure 3.1: Pairwise cost function: Example of the representation of the pairwise cost function in Equation 3.2 for two neurons with radii r_i and r_j respectively.

organization. The total cost is the sum of the pairwise costs between all the elements (neurons and branches of neurons) in the system,

$$Cost = \sum_{i=1}^{N} \sum_{j=i+1}^{N} Cost_{ij}, \tag{3.1}$$

where N is the total number of elements.

The pairwise cost for any pair of elements is (Figure 3.1)

$$Cost_{ij} = \begin{cases} \left(\frac{r_i+r_j}{d_{ij}}\right)^{12} - 2\left(\frac{r_i+r_j}{d_{ij}}\right)^{6} + 1 & \text{if} \quad d_{ij} \leq r_i + r_j \\ \omega_{ij}(dij - (r_i + r_j)) & \text{if} \quad d_{ij} > r_i + r_j \end{cases} \tag{3.2}$$

where,

$$d_{ij} = \sqrt{(x_i - x_j)^2 + (y_i - y_j)^2} \tag{3.3}$$

and

$$\omega_{ij} = \alpha A_{ij} \tag{3.4}$$

where r_i is the radius of neuron i (Appendix §B), x_i and y_i define the position of element i in the xy plane, A is the symmetric connectivity matrix such that A_{ij} is the total number of synapses between neurons i and j (Appendix §C) and α is a factor that balances the relative strength between the two terms of the cost. As we perform alternative calculation with different connectivity matrices, we found convenient to set $\alpha = 1/max(A)$ that automatically sets $max(\omega) = 1$ for all the calculations.

The cost depends on the distances between the elements. For short distances, (lower than $r_i + r_j$, at which the two neurons are touching) the cost is a volume exclusion function modelled like a Lennard-Jones potential [89] (Equation 3.2 and Figure 3.1). This term accounts for the neurons as physical entities that can intermingle but not overlap. With this term, we prevent the wiring minimization from giving a single point as the optimal solution. In addition, this term modelled the relative sizes of the neurons that turned out to be a very important feature of the system. For long distances, the cost is proportional to the distance and the number of synapses between the two neurons, implemented by the connectivity matrix A (Equation 3.2 and Figure 3.1). By making the cost linearly dependent on the connectivity between the two neurons, we are implicitly assuming than all the neuronal branches hold the same number of synapses. As we assume that the branches grow from the border of the neurons, the pairwise cost function is minimal for the distances equal to the sum of their radii. Therefore, if two neurons are separated a distance equal to the sum of their radii, these two neurons would not overlap and their branches length would be zero, since the border of the neurons would be touching.

The optimal configuration is defined by the set $\{x_i, y_i\}$, $i = 1, ..., N$, that

minimizes the total *Cost* in Equation 3.1, for a given connectivity matrix A and a given set of sizes $\{r_i\}$. The problem has no analytical solution and for the typical number of elements in the cartridge the configuration space is so big that an exhaustive exploration is unfeasible. To calculate optimal configurations we used an heuristic algorithm called simulated annealing (Figure 3.2) [90]. The algorithm starts in an specific configuration, State P, that is randomly perturbed to a State Q. In our case, we slightly move a random element in a random direction. If $Cost(x_Q, y_Q) < Cost(x_P, y_P)$ we move the system to State Q and restart the cycle. In order to avoid the system to be trapped in a local minimum, when $Cost(x_Q, y_Q) > Cost(x_P, y_P)$ there is still a probability of accepting State Q. We calculated $\exp -\Delta C/T$ where $\Delta C = Cost(x_Q, y_Q) - Cost(x_P, y_P)$ and T is a parameter called temperature. If $\exp -\Delta C/T$ is lower than a number r randomly chosen from a uniform distribution between 0 and 1, then, we move the system to State Q, else we restart the cycle in State P. While the cycle is repeated, T is exponentially reduced to control the degree of acceptance of high cost configurations. Thus, the algorithm has four parameters, that we set in the following values: initial T ($T_0 = 1.5-2$), T decay rate ($CR = 0.99-0.999$), total number of global iterations ($NT = 1700 - 2590$) and iterations per each T value (NI= 4000-5000). The parameter T is initiated in T_0 and takes the values $T = T_0 CR^{i-1}$, where $i = 1, ..., NT$ until $TF = 5x10^{-12} - 5x10^{-8}$. The parameters are set by trial and error and they cannot be established *a priori*. Apart from sweeping the parameters to make sure that the algorithm was converging, we tried different initial configurations to better explore the configuration space.

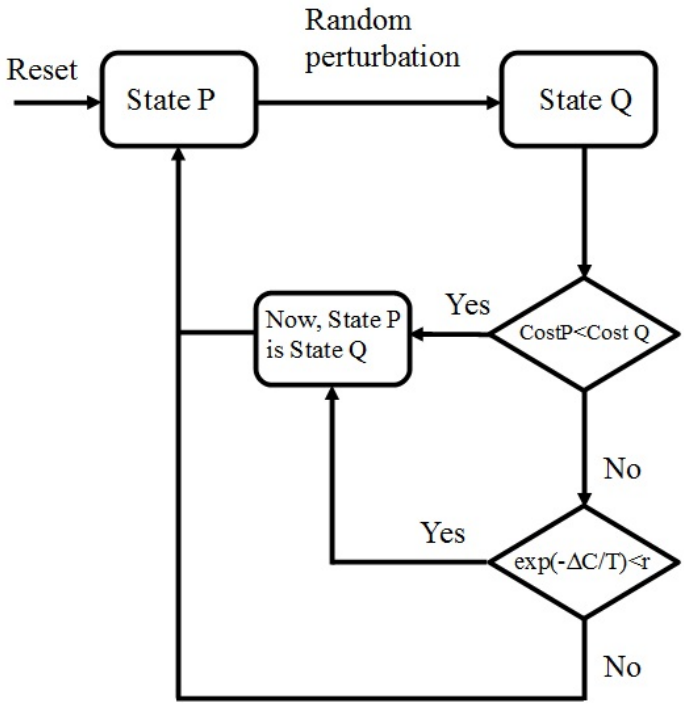

Figure 3.2: Simulated annealing algorithm: Cost is calculated using Equation 3.1, $\Delta C = Cost(x_Q, y_Q) - Cost(x_P, y_P)$, T is a parameter and r is a random number between 0 and 1.

3.3 Low cost configuration in 2D

3.3.1 Elements in the calculation

Most of the neurons in the cartridge have a vertical neurite with horizontal branches to make connections: (i.e., photoreceptors, L1-L5, L4+x, L4-y, Ama, Amb, Amg (Figure 2.9), C2 and C3) or a unique globular branch

like the Lawf cells (Figure 2.9). These neurons can be directly included in the calculation since they can be meaningfully represented by circles centred in their mean positions on the xy plane. Only Lawf f and Lawf k need some pre-processing to crop out their non synaptic axons that are outside the cartridge. However, this is not enough for T1 and Aml that present more than one vertical branch. Thus, they need to be split in their vertical branches, that will then be considered as independent elements in the calculation. In order to split these two neurons we need to go back to the 3D reconstructions (Figure 2.7). In order to identify the segments and the synapses that correspond to each branch, we took advantage of the fact that each branch is placed between two contiguous photoreceptors in the external ring of the cartridge (Figure 2.7). We first calculated the distance of each neuronal segment and each synapse to the six photoreceptors. Based on their two closest photoreceptors, we were able to split T1 in 6 vertical branches (T1 1-6) and Aml in 3 (Aml 1-3). A top view of the synaptic sites of each virtual branch is shown in Figure 3.3.

Neglecting part of the amacrine set, due to their very small size, the complete set of elements used in the calculation is: R1-R6, L1-L4, L4+x, L4-y, L5, Amb, Aml 1-3, Amg, Ama, C2, C3, T1 1-6 and Lawf a-k (Figure 2.9 and Figure 2.7). That makes 38 independent elements. To find minimum wiring configurations we had to use all the pairwise functions (Equation 3.2) at the same time. As we have 38 elements and considering each pair of elements only once, the total number of pairwise functions is 703.

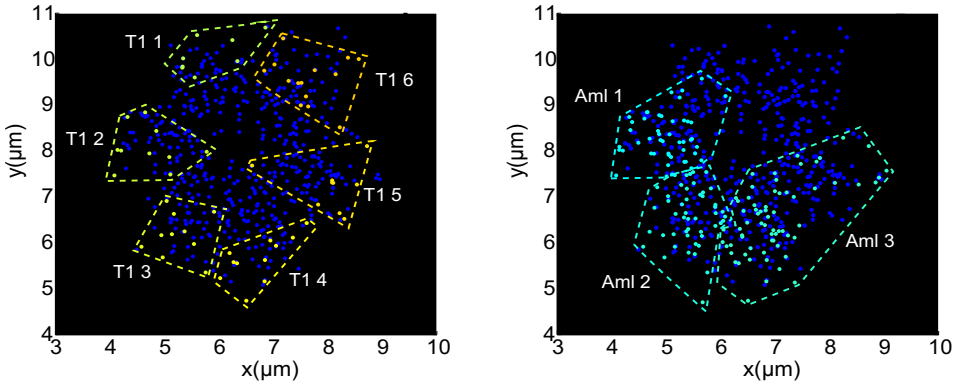

Figure 3.3: Synaptic sites of T1 and Aml branches: Top view of all the synaptic sites in the cartridge (blue dots) and of the synaptic sites of the branches of T1 and Aml (colours). Left: six virtual branches of T1. Right: three virtual branches of Aml. Dashed lines bound the synaptic contacts of each cell to help their differentiation.

3.3.2 Low cost configuration vs. actual configuration

In this section, we compare the configuration with the lowest cost found and the actual configuration. But this comparison is not very meaningful if the actual cartridge is in a very expensive configuration. Therefore, before any comparison we should first check if the actual cartridge is in a low wiring configuration. To do so we defined the wiring cost:

$$Wiring\,Cost_{ij} = \begin{cases} 0 & \text{if} \quad d_{ij} \leq r_i + r_j \\ \omega_{ij}(dij - (r_i + r_j)) & \text{if} \quad d_{ij} > r_i + r_j \end{cases} \tag{3.5}$$

where ω_{ij} is proportional to the connectivity between the neurons (Equation 3.4) and d_{ij} is the distance between the neurons (Equation 3.3). So, here,

the wiring cost assumes the wires to grow form the border of the elements and it is zero for two overlapping elements.

The actual position of the neurons are approximated by the mean positions of their projections on the xy plane and, even if two real neurons cannot be in the same place, their mean position can. Therefore, the volume exclusion term in the Cost would dominate over the connectivity term when two neurons are too close and this would give the false impression that the two neurons are in the same place, which is not physically possible. This is the reason why we used the $WiringCost$ in Equation 3.5 instead of the $Cost$ in Equation 3.2.

In order to check if the actual configuration of the cartridge is a low wiring configuration, we randomly permuted the positions of the neurons to generate up to 1 million of synthetic cartridges. We calculated the wiring cost of the synthetic cartridges and we compared it to the wiring cost of the actual configuration (Figure 3.4). As a control test we made two types of permutations: the first one involves all the neurons at the same time and in the second one the positions of the big and small neurons have been independently permuted. In both cases, the wiring cost of the actual configuration is significantly lower than the cost of the synthetic systems, $p = 10^{-8}$ and $p = 9.6\ 10^{-23}$, respectively. This suggests than the actual cartridge is in a low wiring configuration.

Once we have shown that the actual cartridge has a low wire configuration, we calculated the configuration with the lowest cost in order to compare it with the experimental cartridge. We initiated the simulated annealing algorithm in the experimental configuration $\{x_{actual}, y_{actual}\}$, and for the experimental connectivity and sizes of the neurons, we obtained the

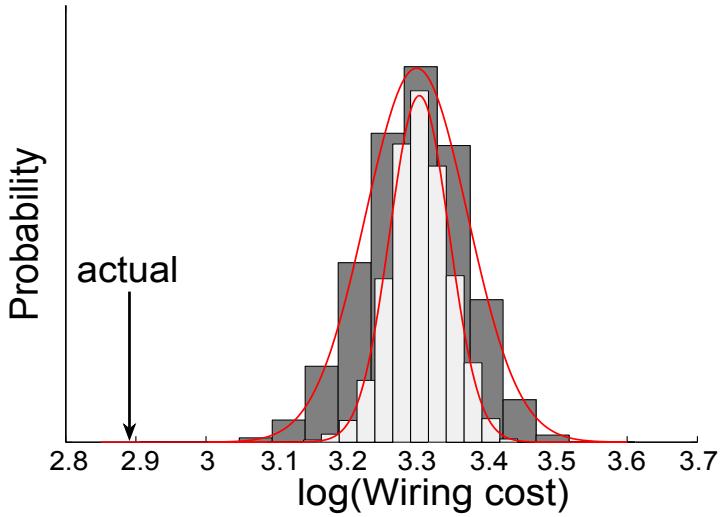

Figure 3.4: Permutations of the actual configuration: Wiring cost (Equation 3.5) of 1 million of permutations of the positions of all the elements in the cartridge (dark gray bars) and of the big and small elements independently (light gray bars). Histograms are fit by gaussian functions (red lines) to calculate the significance of the actual wiring cost (arrow).

configuration in the lowest local minimum $\{x_{llm}, y_{llm}\}$ among all the local minima explored by simulated annealing in this calculation. From now on we refer this configuration as llm configuration.

The llm configuration $\{x_{llm}, y_{llm}\}$ is shown in Figure 3.5. As no external constraints have been added we are free to translate and rotate the system as a whole to mimic as much as possible the actual orientation and position of the cartridge. Each element is represented by a circle placed in $\{x_{llm}, y_{llm}\}$ with their actual radii $\{r_{actual}\}$ (§B). The lines in Figure 3.5 connect $\{x_{llm}, y_{llm}\}$ with $\{x_{actual}, y_{actual}\}$. The general structure is similar

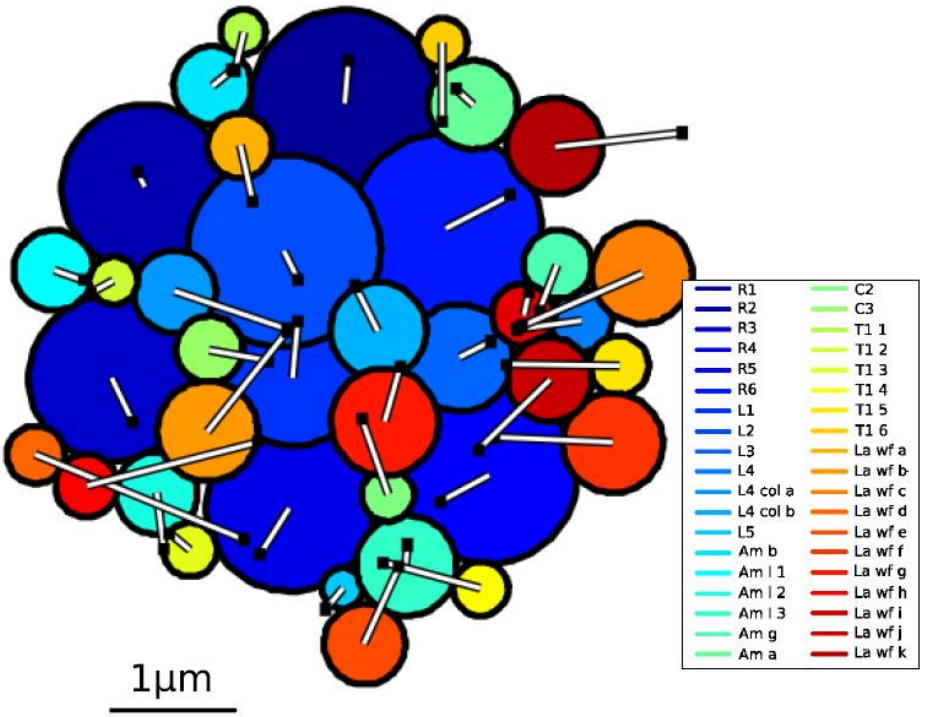

Figure 3.5: 2D configuration in the lowest local minimum of cost: The elements are placed in the configuration with the lowest cost. The radii of the circles represent the actual sizes of the elements. The tips of the lines show the actual configuration.

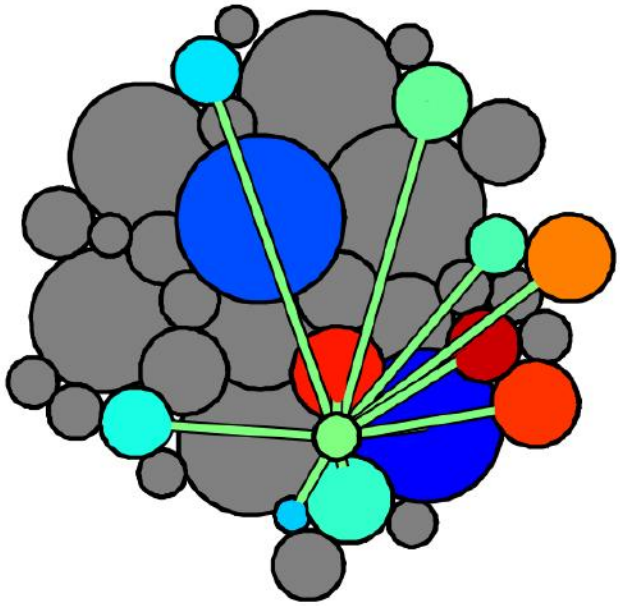

Figure 3.6: Diagram of the C2 connectivity: The elements of the systems connected to C2 receive a virtual branch from C2 and are highlighted with the same colors as in Figure 3.5

in both configurations: the photoreceptors are in a ring in the outside alternated by T1 and amacrine branches and L1 and L2 are in the center of the structure. The mean error of the prediction is only $0.56\,\mu m$ while the mean error for one thousand the permuted configurations is $1.9 \pm 0.1\ \mu m$. The mean error is defined as the mean distance between the llm configuration and the actual configuration:

$$mean\ error = \frac{1}{N}\sum_{i}^{N}\sqrt{(x_{i\,actual} - x_{i\,llm})^2 + (y_{i\,actual} - y_{i\,llm})^2} \qquad (3.6)$$

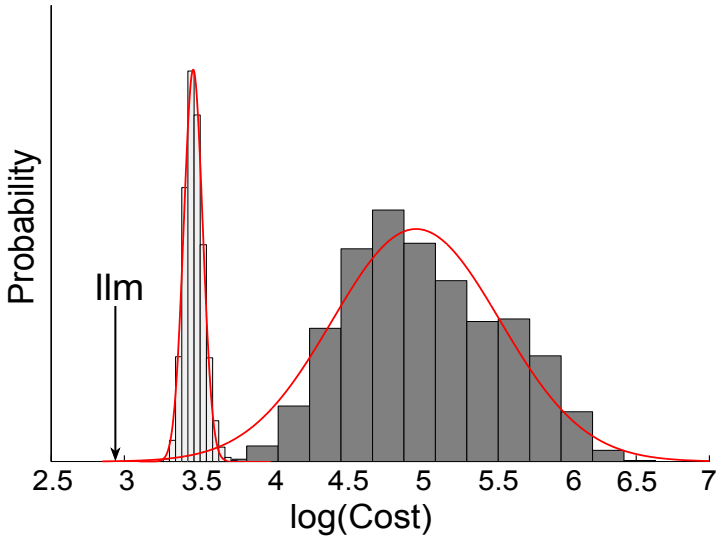

Figure 3.7: Permutations of the lowest cost configuration: Cost of 1 million permutations of the positions of all the elements in the the lowest cost configuration (dark gray bars) and of the big and small elements independently (light gray bars). Histograms are fit by gaussian functions (red lines) to calculate the significance of the lowest local minimum (arrow).

where N is the total number of elements.

The high interconnectivity of the cartridge neural network makes the system indivisible in independent subnetworks and the organization non trivial. As an example we show highlighted the cells connected to C2 (Figure 3.6), that it is not only connected to neighbouring elements but also to farther ones. We used C2 as an example but the case is the same for most of the elements of the cartridge. So, the llm solution is not as simple as putting connected elements closer, but a complicated trade off between the relative sizes of the elements and their connectivity.

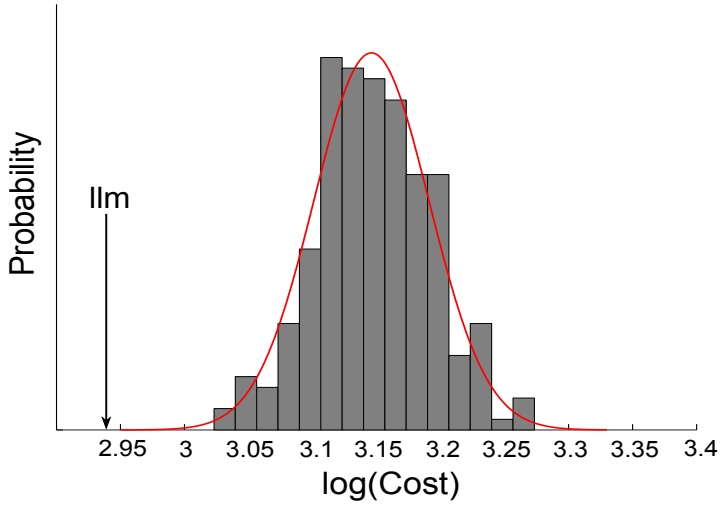

Figure 3.8: Cost of 240 local minima: Cost of the 240 local minima found fit by a gaussian function (red) and cost of the lowest local minimum, llm, (arrow).

The llm configuration is in a local minimum of the cost function but to better understand how important this local minimum is, we explored roughly the whole configuration space. We permuted the positions (x_{llm}, y_{llm}) among all the elements and we calculated the *Cost* of each of the permuted configurations. We did two different types of permutations: one that includes all the elements and another that permutes large and small elements independently (Figure 3.7). In both cases the llm configuration has a lower cost than any of the permuted configurations $p = 10^{-4}$ and $p = 6.3\ 10^{-7}$ respectively.

To study the position of llm with respect to the rest of local minima of the cost function, we performed 240 calculations initiated in 240 different

configurations. In each case, the algorithm converges to a final configuration that is, at least, in a local minimum. The final configuration with the lowest cost among the 240 local minima is the one obtained when we initiated the algorithm in the actual configuration (llm configuration) (Figure 3.8). This cost is significantly lower than cost of the rest of the local minima ($p = 1.4\,10^{-6}$). It is also, the closest one to the actual configuration.

3.3.3 Controls

If the simulated annealing parameters are not well chosen the algorithm cannot converge. To show that our calculation has actually arrived at least to a local minimum, we explored the configuration space close to the llm configuration found by simulated annealing. To do so we moved one element at a time from $(x_{llm\,i}, y_{llm\,i})$ to $(x_{llm\,i} + \Delta x, y_{llm\,i})$ or to $(x_{llm\,i}, y_{llm\,i} + \Delta y)$ where Δx and Δy varied from -0.25 to 0.25 μm. We calculated the $Cost$ of these perturbed configurations (Figure 3.9) that increases when we moved any neuron, suggesting that we are at least at a local minimum.

As we pointed out before, the pairwise wiring cost has two terms (Equation 3.2): a volume exclusion term for short distances and a wiring term for long distances. The wiring term is proportional to the number of synapses between each pair of neurons (A_{ij} Appendix §C) and to their relative distance (d_{ij}). However, the actual form of the volume exclusion term is not known. We have used a standard function in physics, the Lennard-Jones potential, but any other function with a soft decay could be used. To verify that the results do not change quantitatively with the volume exclusion function, we repeated the calculation with two alternative volume exclusion terms: a truncated Lennard-Jones function and a 1/distance function.

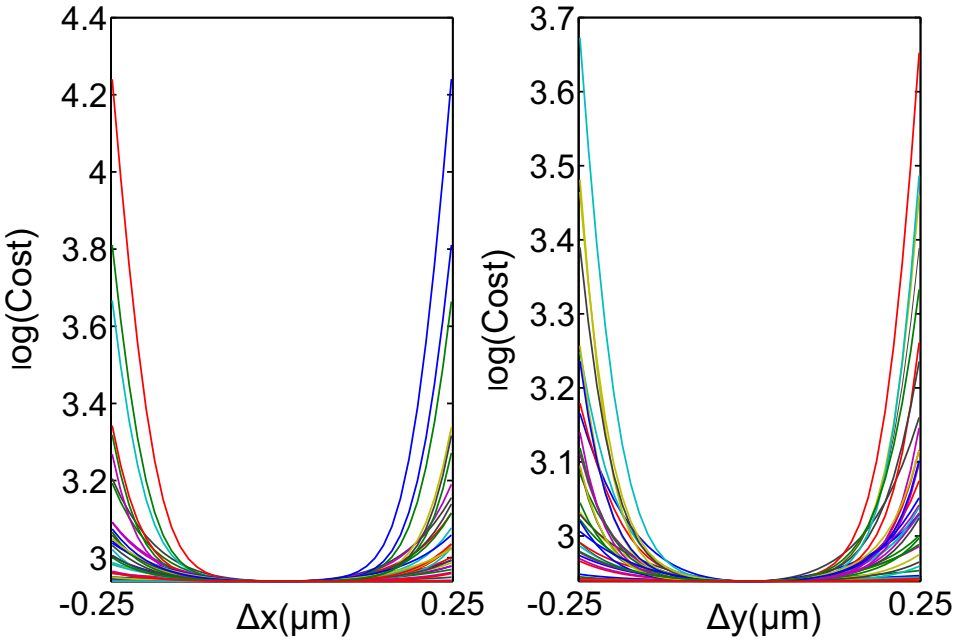

Figure 3.9: Exploring the configuration space close to the llm: From the llm configuration, each element is independently moved in the x (left) or y (right) directions. The cost increases when moving any neuron in any of the two directions.

The truncated Lennard-Jones pairwise cost is defined as:

$$Cost\,truncated_{ij} = \begin{cases} \left(\frac{r_i+r_j}{d_{ij}}\right)^{12} - 1 & \text{if} \quad d_{ij} \leq r_i + r_j \\ \omega_{ij}(dij - (r_i + r_j)) & \text{if} \quad d_{ij} > r_i + r_j \end{cases} \tag{3.7}$$

where r_i are the radii of the neurons, d_{ij} their distance (Equation 3.3) and ω_{ij} is proportional to their connectivity (Equation 3.4).

And the 1/distance pairwise cost function is defined as:

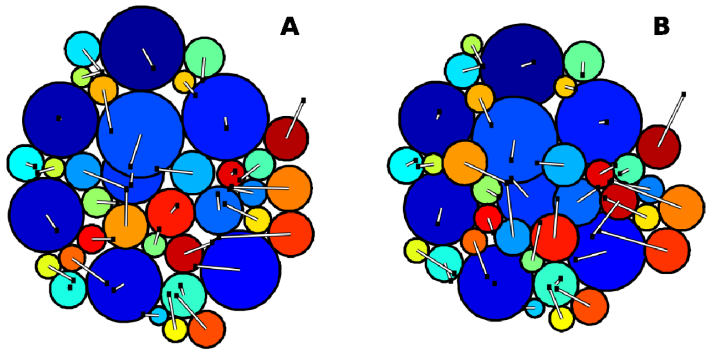

Figure 3.10: Alternative volume exclusion potentials: Low cost configuration calculated assuming two different alternative volume exclusion potentials: A) 1/distance pairwise cost function (Equation 3.8) and B) truncated Lennard-Jones pairwise cost function (Equation 3.7).

$$Cost\ 1/distance_{ij} = \begin{cases} \beta\left(\frac{1}{d_{ij}} - \frac{1}{r_i+r_j}\right) & \text{if} \quad d_{ij} \leq r_i + r_j \\ \omega_{ij}(dij - (r_i + r_j)) & \text{if} \quad d_{ij} > r_i + r_j \end{cases} \tag{3.8}$$

where $\beta = 1000$ is a normalization term, r_i are the radii of the neurons, d_{ij} their distance (Equation 3.3) and ω_{ij} is proportional to their connectivity (Equation 3.4).

All the normalization terms make the pairwise costs to be zero when the two neurons are touching but not overlapping so, that is, $Cost_{ij}(r_i+r_j) = 0$. The normalization parameter $\beta = 1000$ is used to have a reasonable weight with respect to the wiring part of the pairwise costs, lower values of β led to too soft neurons and higher values generated too hard neurons.

The configurations with the lowest total cost found for the two alternative volume exclusion potentials were initiated in the actual configuration

(Figure 3.10). They are very similar to the actual cartridge and to the previous llm configuration in Figure 3.3.

3.3.4 Impact of individual errors

One cartridge has a low number of neurons and a high number of repetitions. These two facts should tend to reduce the evolutionary time needed to arrange a close to optimal configuration. Although the actual configuration is close to the lowest local minimum, it is slightly deviated from it.

The stochastic optimization framework shows that the distribution of deviations from optimality of the different elements of the system has some structure [11]. The elements with a higher impact on cost tend to be closer to their optimal positions that those elements with less impact. In the cartridge, the elements with higher impact in the total Cost are those with a larger number of synapses, that is L1, L2 and the photoreceptors terminals. As we see in Figure 3.11 these are elements with low errors, while two of the less connected elements as Lawf d and Lawf h have the highest errors. The elements are placed under a $1/\#\ synapses$ curve (Figure 3.11) showing how the less connected neurons could have extra wire due to their low relative impact in the final cost. Similar results have been obtain before in the *C. elegans* nervous system [11].

To verify that the actual distribution of deviations with respect to $\{x_{llm}, y_{llm}\}$ is significant and it allows the actual cartridge to be in a low wiring configuration, we randomly reassigned the errors among the elements. By calculating the wiring cost of these configurations we proved that the actual configuration has a significantly low wiring cost $p = 0.0052$

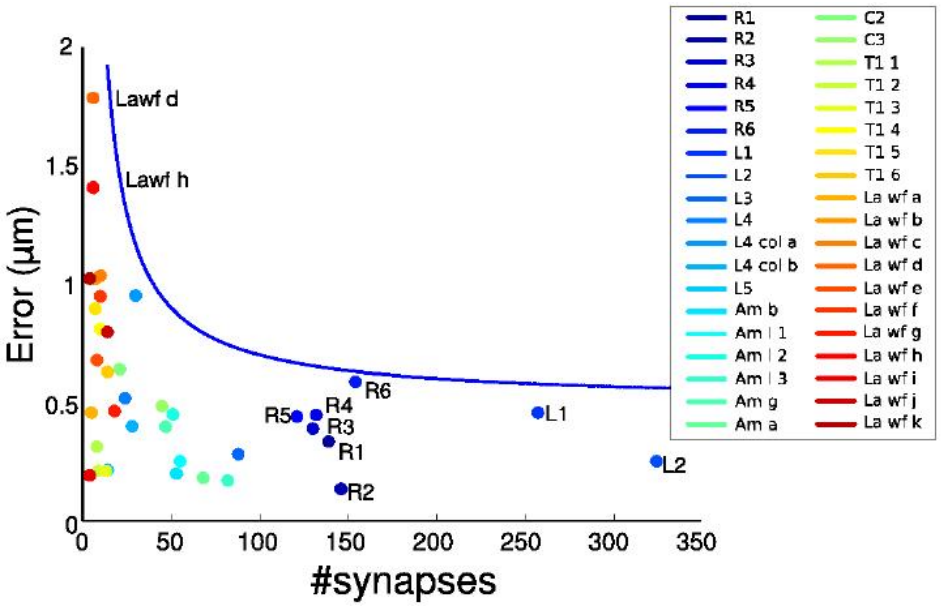

Figure 3.11: Errors correlates with the number of synapses: Error (difference between actual and the lowest cost configuration) vs. number of synapses for each element. The enveloping curve is a 1/#synapses function.

(Figure 3.12). This suggests that even the distribution of the deviations from the llm configuration has the organization predicted by wiring economy.

3.4 The role of connectivity and sizes

To find the roles of connectivity and sizes in the structure of the cartridge and to verify than the optimization is not a trivial consequence of them, we

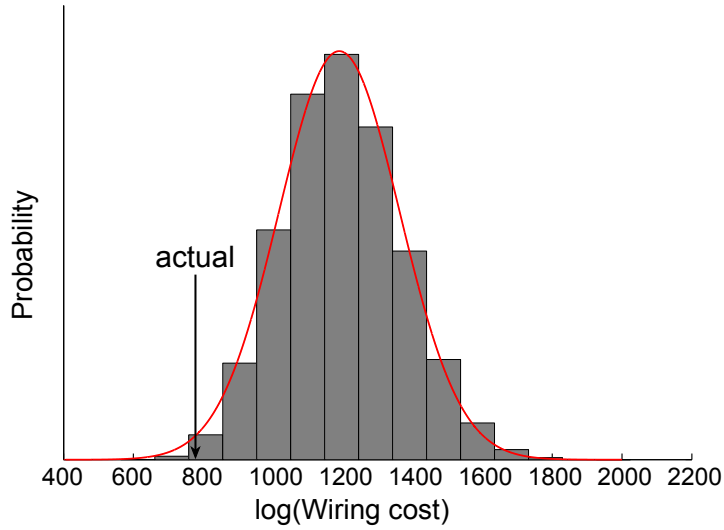

Figure 3.12: Permutations of the error distribution: The errors are randomly distributed and added to the lowest cost configuration, to generate alternative synthetic systems. Histogram is fit by a gaussian function (red lines) to calculate the significance of the lowest local minimum (arrow).

created three different synthetic systems. For each system, we calculated a low wiring configuration and we compared it to the original cartridge (Figure 3.13). First, we randomized the connectivity keeping the actual sizes (Figure 3.13 A), then we randomized the sizes keeping the actual connectivity (Figure 3.13 B) and finally, we randomized both the connectivity and the sizes of the neurons (Figure 3.13 C). The resulting low wiring configurations are not capturing the actual configuration of the cartridge, in fact the errors are: $1.24\mu m$, $0.85\mu m$ and $1.23\mu m$. These errors are higher than the error of the llm configuration. This result suggests that both the relative sizes of the neurons and their connectivity are necessary for the

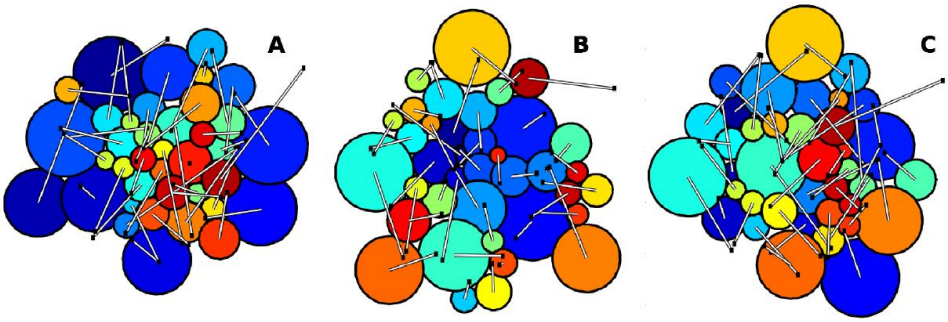

Figure 3.13: Randomized systems: Low cost configurations calculated for three randomized synthetic systems. A) Random connectivity and actual radii. B) Random radii and actual connectivity. C) Random connectivity and radii.

final arrangement. These calculations also show than the algorithm can escape from the initial configuration, since all of them have been initiated in the actual configuration.

The low wiring configurations of the randomized systems (Figure 3.13) suggest that both the relative sizes of the neurons and their connectivity are essential for the actual arrangement. But a more systematic study is necessary in order to understand which are the fundamental features controlling this optimization process. We distorted the original connectivity matrix and the original distribution of sizes generating alternative distorted systems. For each distorted system we calculated the corresponding llm configuration and we compared it with the original configuration. When the llm configuration of a distorted system is similar to the configuration of the actual system, that means that the feature distorted is not important for the optimization process, since the structure is robust against changes in

that specific feature. We distorted independently the connectivity matrix (Figure 3.14, blue line) and the sizes distribution (Figure 3.14, green line) to generate 4 different systems. Their corresponding low cost configurations and errors are shown in Figure 3.14:

- Homogeneous radii: all radii are set to 0.42 μm. The configuration in the lowest local minimum is an hexagonal lattice not related to the actual one.

- Inverted radii: small and large radii had been interchanged. The cartridge structure is lost in the configuration in the lowest local minimum.

- Homogeneous matrix: For all $\{i, j\}$ such that $\omega_{ij} \neq 0$ in the original system, $\omega_{ij\,homog} = \bar{\omega} = 0.1396$ in the homogeneous system. Even when the relative number of synapses have been omitted, the configuration in the lowest local minimum keeps the general structure of the actual cartridge. That is, the photoreceptors are in the outside with L1 and L2 in the inside and the rest of small cells are intermingle in the structure preferentially in the inside.

- Inverted matrix: small and large elements in the connectivity matrix have been interchanged. The configuration in the lowest local minimum is not similar to the actual configuration.

Thus, these results suggest that the relative sizes of the neurons are fundamental for the optimization process. Although the connectivity is also important for the actual structure, the global structure is fairly robust

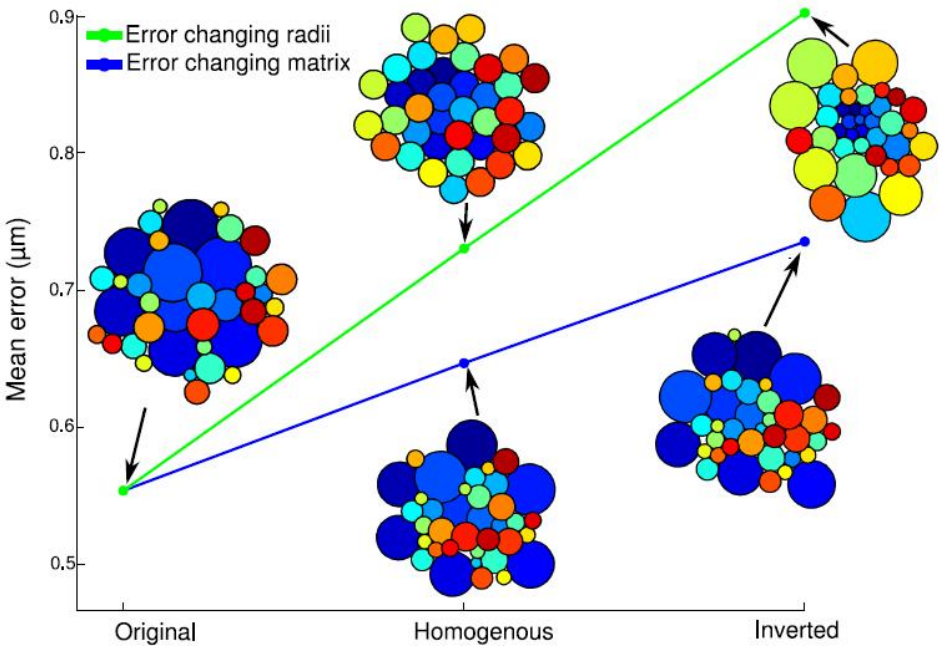

Figure 3.14: Error in the degraded systems: Error vs. degradation: degradation in the radii distribution (green line) and degradation in the connectivity matrix (blue line). For each system the lowest cost configuration is shown.

against changes in the relative number of synapses, as suggested by the configuration of the lowest local minimum with the homogeneous matrix. Thus, the important feature of the connectivity is its general structure, until some extent, not the individual values of synapses.

A global observation that can be made is the fact that the large neurons tend to be in the outside and the small one in the inside. The exception are L1 and L2 in the actual system (Figure 3.3). The connectivity between

L1/L2 and the photoreceptors is the highest in the cartridge and, more importantly it is almost the same for all the photoreceptors. That keeps L1 and L2 in the center of the cartridge, even if they are the largest neurons besides photoreceptors. To fully understand the relationship between the relative sizes of the neurons and their connectivity, in §3.5 we developed a set of synthetic systems to capture the importance of each feature independently.

3.5 Toy model

In order tu fully understand the anatomical structure of the cartridge, in its 2 dimensional representation, we have simplified the system. We have included only four types of cells: 6 photoreceptor-like cells, 1 L1-like cell, 1 L2-like cell and 30 small cells that would mimic the rest of the neurons. The sizes and color code of the cells in the simple model are summarized in Table 3.1. The sizes of the photoreceptor-like and L2-like cells are the mean of their actual sizes respectively, L1-like cell has its actual size and the small cells has the actual mean size of the rest of the neurons in the cartridge.

The connectivity matrix has been also simplified (Figure 3.15). Only two different values in the connectivity have been used: a high one representing the photoreceptors to L1/L2 connectivity (42.5 synapses) and small one representing the connectivity of the small cells (4 synapses). The high number of synapses has the value of the mean connectivity between photoreceptors and L1/L2 and the small number of synapses has the mean value of the connectivity among the rest of the neurons. The connectiv-

Cell	Colour	Size (pixels)
Photoreceptor-like		57.22
L1-like		57.22
L2-like		44
Small cells		23.9344

Table 3.1: Cells included in the toy model

ity of the small cells has been set up randomly keeping the ratio of connected/unconnected cells at its actual value 0.2. That means that among all the entries in the connectivity matrix that correspond to a small cell, 20% of them have been randomly chosen to contain synapses. As in the actual system the connectivity among the photoreceptors is set to zero.

Using the 4 different subsets of the cells and the corresponding parts of the simplified connectivity matrix, 4 different simplified cartridges have been generated. They include these subsets of neurons:

(a) Photoreceptors + L2

(b) Photoreceptors + L1 + L2

(c) Photoreceptors + small cells

(d) Photoreceptors + L1 + L2 + small cells.

We calculated the configuration in the lowest local minimum of the 4 simplified cartridges using the same cost and simulated annealing algorithm as for the full cartridge representations (Figure 3.16). The low wire configuration of system (a) shows that a group of elements with the same size and

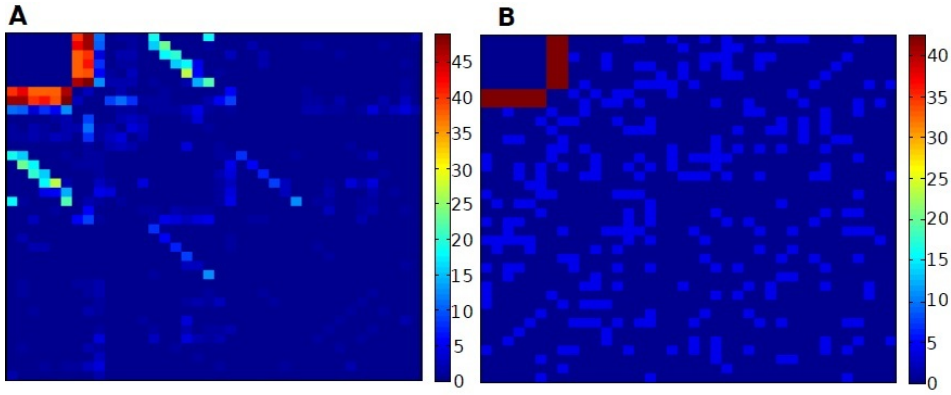

Figure 3.15: Actual and simplified connectivity matrices: A) actual connectivity matrix used in the calculation. B) Simplified connectivity matrix used in the toy model.

connectivity all to one has low wiring when the most connected element is placed in the center of the structure. That would explain why L1 and L2 are centred in the cartridge, considering that their size is similar to the photoreceptor size and their connectivity has also an all to one structure.

To verify that the simultaneous presence of L1 and L2 in the actual cartridge does not change this result, in system (b) we included both L1-like and L2-like cells. Therefore, when cells have similar sizes in an all to one connectivity framework, the low wire configuration places the most connected components in the center of the structure (Figure 3.16 (a) and (b)).

The low wire configuration of system (c) predicts that when big and small cells are connected randomly, their low wire configuration has the small elements in the inside of the structure pushing the big elements to

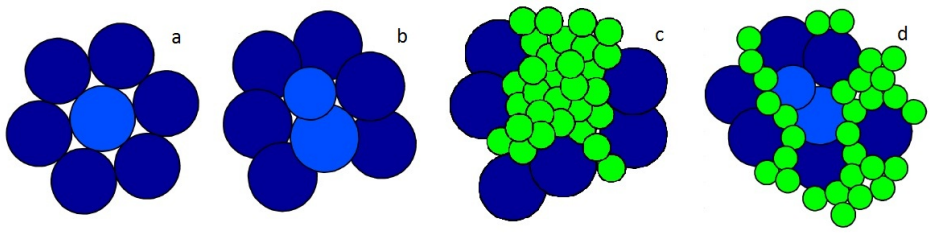

Figure 3.16: Low wire configurations of the simplified systems: from left to right, models (a), (b), (c) and (d). The color code is the same as in Table 3.1.

the outside (Figure 3.16 (c)). This result was already suggested by the distorted systems in the previous section. To understand this result we should think about the extra cable that a big cell would generate when placing it in the center of the structure. All the rest of the cells would be pushed out, and this would increase the relative distance among them, and consequently the total cable. Therefore, the low wire configuration placed the small cells in the center and the big cells surrounding them, reducing the relative distances between the cells.

The results so far explained independently why L1 and L2 are centred in the cartridge and why the small cells tend to be inside the photoreceptor ring, but the remaining question is what happens when combining all the elements. In system (d) we included the 38 simplified cells (Table 3.1) connected by the full simplified connectivity matrix (Figure 3.15, right). The low wire configuration in system (d) (Figure 3.16 (d)) shows the same general structure as the actual cartridge: the photoreceptor-like cells in the outside, L1-like and L2-like cells in the center and the small cells intermingled in the structure. Therefore, we can reproduce the main

features of the cartridge anatomy with only 4 types of neurons with three different sizes and with a connectivity matrix with only two different values of connections that is random for most of the cells. Also, the connectivity must be stronger between photoreceptors and L1/L2 than for the rest of the neurons. However, this system does not split the group of small cells in several groups, like the actual cartridge. This suggests that the actual connectivity of the small cells has a certain degree of structure that is not captured by the simplified random matrix we used.

3.6 Low wire configuration in 3D

Once we have fully understood the anatomy of the cartridge in the a 2D representation we can move our model forward to a more realistic 3D representation. Three anatomically distinct horizontal layers can be identified in the cartridge (Table 3.2), that may have different functions [22]. The distal layer, the closest to the retina, is the only one holding the branches from Lawf cells. The central layer, that is the biggest one, does not hold any tangential branches. The proximal layer, which is the closest to the brain, is the region where the L4 complex makes its synapses (Figure 2.13). In this 3D model we approximated each layer to an horizontal plane and we vertically connected the three layers through the common neurons between consecutive layers. Extra layers could be considered, with a subsequent increase in the calculation complexity. We observed that the connectivity was homogeneous within each layer and, at the same time, different from layer to layer. Therefore, they constitute a very reasonable representation of the 3D structure of the cartridge and we decided not to include more

Layer	Sections	number of neurons
Distal	1-150	36
Central	151-450	26
Proximal	451-628	21

Table 3.2: Horizontal layers

layers in the calculation.

As our reconstruction of a cartridge includes the position of each synapse, we could assign the corresponding synapses to each layer. As we did for the whole cartridge, we projected each layer in a plane. In each layer we included only those neurons that make synaptic contacts in that layer (Table 3.2). The position of the neurons in each layer is defined by $\{x_{ki}, y_{ki}\}$, where k = 1, 2, 3 indicates the distal, central and proximal layers respectively. We associated different connectivity matrices A_k to each layer. As, neurons that appear in more than one layer can present different sizes in each layer, the radius of neuron i in layer k is defined by r_{ki}, and corresponds the actual mean size of that neuron in that layer.

Now that we have defined the 3D model, we need to define a total cost function to be minimized. The total cost is the sum of the pairwise costs between neurons in each layer plus a cost associated with connecting each neuron to itself in consecutive layers that we called $link3D$. Thus,

$$Cost3D = \sum_{k=1}^{3} \sum_{i=1}^{N_k} \sum_{j=i+1}^{N_k} Cost_{kij} + link3D_{12} + link3D_{23} \qquad (3.9)$$

where k = 1, 2, 3 corresponds to distal, central and proximal layers, respectively and N_k is the number of neurons in each layer.

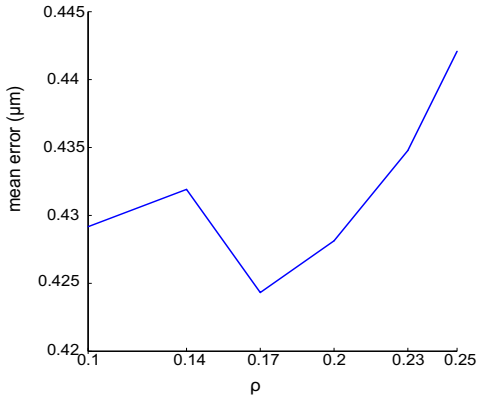

Figure 3.17: Prediction error vs. ρ: Alternative ρ values are used to calculate the lowest local minimum. The lowest mean error is obtain when $\rho_{min} = 0.17$

The pairwise cost within a layer, $Cost_k$, is the same one for the 2D representation, but defined in each layer independently:

$$Cost_{kij} = \begin{cases} \left(\frac{r_{ki}+r_{kj}}{d_{kij}}\right)^{12} - 2\left(\frac{r_{ki}+r_{kj}}{d_{kij}}\right)^{6} + 1 & \text{if} \quad d_{kij} \leq r_{ki} + r_{kj} \\ \omega_{kij}(d_{kij} - (r_{ki} + r_{kj})) & \text{if} \quad d_{kij} > r_{ki} + r_{kj} \end{cases} \tag{3.10}$$

where r_{ki} is the radius of neuron i in layer k,

$$d_{kij} = \sqrt{(x_{ki} - x_{kj})^2 + (y_{ki} - y_{kj})^2} \tag{3.11}$$

and

$$\omega_{kij} = A_{kij}/max(A_k) \tag{3.12}$$

where A_k is the symmetric connectivity matrix in layer k.

Thus, the novelty of the 3D study is the component $link3D$ that connects the neurons to themselves from layer to layer:

$$link3D_{mn} = \sum_i \rho\sqrt{(x_{mi} - x_{ni})^2 + (y_{mi} - y_{ni})^2} \tag{3.13}$$

where m and n are two consecutive layers, i are only those neurons that are both in layer m and layer n and ρ is the vertical rigidity of the neurons. For $\rho = 0$ the three layers are not connected at all and for $\rho = \infty$ the neurons became vertical sticks.

To choose the best value for ρ we have calculated the low wire configuration of the neurons for a set of different ρ values. To compare those low wiring configurations to the actual one, we calculated their difference, or error, by considering the neurons in the three layers at the same time (Figure 3.17). The low wiring configuration closest to the experimental one is obtained for $\rho_{min} = 0.17$. We therefore, adopted this value as the most representative one. We show the llm configuration with $\rho_{min} = 0.17$ in Figure 3.18 compared to the actual one. The centres of the circles are placed in the llm positions and the lines connect llm and actual positions.

The 3D optimization process is a trade-off between the 2D connectivity in each layer and the vertical consistency of the neurons. The mean values of the non-zero elements of the normalized connectivity ω in the three layers are: $\bar{\omega}_1 = 0.2$, $\bar{\omega}_2 = 0.2979$ and $\bar{\omega}_3 = 0.3359$. Note that the functional form of the wiring cost and $link3D$ are similar. Therefore, the ration between ρ and ω gives as an idea about the relative strength between the two costs. As the most representative vertical consistency $\rho = 0.17$ has a comparable value to $\bar{\omega}$ the synaptic connectivity strength is comparable to the vertical consistency of the neurons.

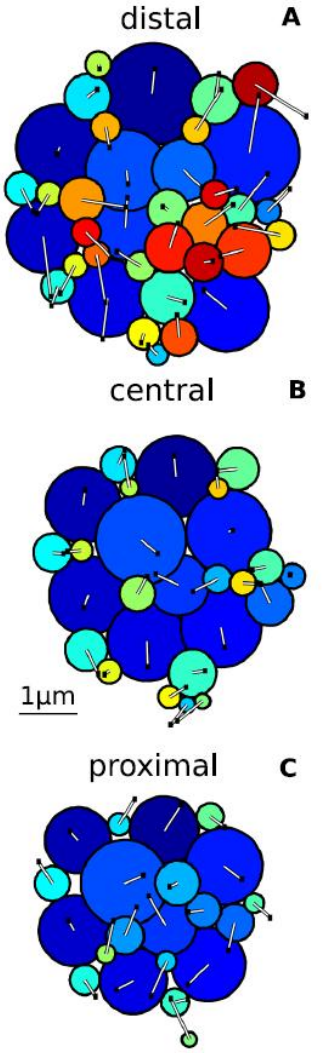

Figure 3.18: 3D low cost configuration: Lowest cost configuration found for the approximation in 3 layers: A) distal, B) central and C) proximal. The radii of the circles represent the actual sizes of the elements. The tips of the lines show the actual configuration. The color code is the same as in Figure 3.3.

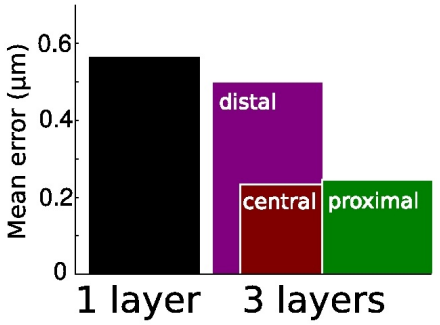

Figure 3.19: Prediction errors in 2D and in 3D: Error of the configuration in the lowest local minimum, for the 2D model (1 layer) and the 3D model (3 layers).

The 3D approximation represents better the actual cartridge than the 2D representation. Since some of the neurons like the Lawf cells and the L4 collateral are not present in the whole cartridge length, the 2D projection does not capture their 3D anatomy. The similarity in 3D is higher to the actual system as the mean total error is 0.42 μm while the mean error in 2D is 0.56 μm(Figure 3.19).

3.7 Discussion and conclusions

We have shown that the cartridge configuration is a low wiring configuration, and also very similar to the configuration in the lowest local minimum of the cost function (llm configuration) that we have found. We also showed that the structure of the cartridge is non trivial and indivisible due to the high interconnectivity of the network.

Due to the high number of variables we used an heuristic iterative algo-

rithm to avoid exploring exhaustively the whole configuration space. This algorithm converges to a local minimum, but cannot guarantee to converge in the global minimum. In order to obtain a meaningful local minimum for the actual structure we initiated the algorithm in the actual configuration. We obtained a configuration in a local minimum that is similar to the actual cartridge and that turned out to be the lowest local minimum found when comparing it with other 240 local minimum obtained initiating the algorithm in 240 different configurations.

The cost function that we have designed for this work includes an attractive part proportional to the number of synapses between the neurons and a repulsive term that, for the first time, takes into account the relative sizes of the neurons. This repulsive term keeps the neurons from occupying the same physical space. This was enough to prevent the optimal configuration of the system from collapsing in one point, so no external constrains are needed. This cost function implicitly assumes that all the branches of all the neurons in the cartridge contain the same number of synapses. Although this is not exactly true for all the neurons, its impact on the cartridge configuration is neglected since we have shown that the arrangement of the cartridge is fairly robust against changes in connectivity values.

In order to understand the role of the two driven forces of the system, i.e., the connectivity and the relative sizes of the neurons, we generate alternative systems and we calculated their low cost configurations. We have shown that both the relative sizes of the neurons and their connectivity are crucial for the final arrangement. However, the important feature of the connectivity is its general structure and not the specific number of synapses between the neurons.

By simplifying the original system, we have obtained some general conclusions that can be extrapolated to other systems with connected components. We have shown that big elements tend to be in the outside of the structures to improve the packing. However big elements can be in the inside of the structures if they are evenly and strongly connected to the rest of the big elements.

The errors between the actual configuration of the neurons and the llm configuration, correlate inversely with the number of synapses. Therefore, the neurons with more synapses, thus having a greater impact on the cost, are closer to their llm positions. This result has been shown before for the positions of the neurons in *C. elegans* and for reaction rate in the metabolism of *E. coli* [11]. It seems to have a general application to many systems that optimize a cost function.

We have shown that the 3-dimensional structure of the cartridge is a consequence of lowering the total wire in a trade off between the horizontal neural connectivity and the vertical consistency of the neurons. But to answer the question of why the cartridges are cylinders, in opposition to globular structures like for example, in the antennal lobe also in *Drosophila melanogaster* we need to zoom out a bit. The visual information must travel from the eyes to the brain and physical constraints control the position of the eyes. More precisely, to generate low wiring visual systems the neurons should have a preferred direction parallel to the virtual line that connects the eyes and the brain. In this sense the lamina neurons follow pretty well this description, as most of them are vertically organized with short horizontal branches, generating the characteristic cylindrical structure of the cartridge.

Conclusions

The conclusions drawn by this study are divided in two sections:

Cartridge reconstruction

- Lamina wide-field cells (Lawf) make synaptic contacts in the lamina. They are mainly presynaptic, that means that they input information to the cartridge.

- L5 is a postsynaptic neuron in the *Drosophila melanogaster* lamina. This solves the mystery of the presence of L5 in lamina.

- Contradicting previous studies, we showed that the amacrine cell feedbacks to photoreceptors are almost absent. Amacrine cells are the main interneuron in the cartridge, mediating the information flux from inputs to outputs.

- We discovered that *satellite glia* and *marginal glia*, as *epithelial glia*, are postsynaptic in the lamina.

Wiring economy with volume exclusion

- The cartridge organization is in a low wiring configuration. It is close to the configuration in the lowest local minimum of the wiring cost function, suggesting that the evolution of the cartridge tends to minimize the total wiring.

- The two main features controlling the cartridge organization are the relative sizes of the neurons and the general structure of the connectivity.

- The deviations that we found between the actual and the configuration with the lowest wiring cost are distributed in such a way that neurons with the higher number of synapses are less deviated than neurons with less synapses. This implies that theses deviations are not randomly organized.

- The 3D organization of the cartridge is a trade off between the horizontal features (connectivity and volume exclusion of the neurons) and the vertical consistency of the neurons. The neurons have a soft vertical consistency. Thus, they are nor completely lax nor vertical sticks.

- From our toy model we propose that, for many connected system that minimizes the total wire, the small elements would tend to be located in the center of the structure, surrounded by the big elements. Big elements strongly and evenly connected to the rest of the big elements are an exception as they would be placed in the center of the structure.

Conclusiones

Las conclusiones que se derivan de este estudio se dividen en dos sectiones:

Reconstrucción de un cartucho

- Las células Lawf son sinápticas en lámina. Son principalmente presinápticas y, por tanto, constituyen una entrada de información al cartucho.

- L5 es postsináptica en lámina. Esto, resuelve el enigma de su presencia en lámina.

- Contradiciendo estudios anteriores, hemos descubierto que las conexiones de retroalimentación de las células amacrinas a los fotoreceptores son casi inexistentes. Las células amacrinas son las principales interneuronas en el cartucho, median el flujo de información entre las entradas y las salidas.

- Hemos descubierto que la glia satélite y la glia marginal son, junto con la glia epitelial, postsynápticas en lámina.

Economía de cableado con exclusión por volumen

- El cartucho se encuentra en una organización de bajo cable. Su configuración es similar a la configuración en el mínimo local mas bajo de la función de coste que hemos encontrado. Esto sugiere que la evolución del cartucho tiende a minimizar el cable total.

- Los dos componentes principales en la organización del cartucho son el tamaño relativo de las neuronas y la red neuronal, pero no el número específico de sinapsis.

- Las desviaciones entre la configuración real y la configuración de menor coste de cableado encontrada se distribuyen de tal modo que las neuronas con más conexiones se encuentran más desviadas que las neuronas con pocas sinapsis. Esto implica que estas desviaciones no están organizadas al azar.

- La organización en 3D del cartucho es un juego compensatorio entre las componentes horizontales (conectividad y la exclusión por volumen) y la propia consistencia vertical de las neuronas. Las neuronas tienen una suave consistencia vertical, de tal forma que ni son completamente laxas ni completamente verticales y rígidas.

- A partir de nuestro modelo simplificado, proponemos que para muchos sistemas con elementos conectados, y que minimimice el cable total, los elementos más pequeños tienden a situarse en el centro de la estructura rodeados por los elementos más grandes. La excepción la constituirían los elementos grandes que están fuerte y ho-

mogéneamente conectados al resto de los elementos grandes que se colocarían en el centro de la estructura.

Appendix A

Synapse table

certain	x	y	section	pre	post1	post2	post3	post4	post5
Yes	1.8655	2.2815	14	Lawfk	L3				
Yes	1.5121	-0.2357	14	Lawfg	L3	Ama	Aml		
Yes	1.2544	2.1847	15	R1	L3	Lawfk	L1	sat.glia	
Yes	1.8337	2.7761	16	R1	L3	L2	orph.	orph.	
Yes	1.3892	1.0782	19	C2	Ama	L2	orph.	orph.	
No	1.7020	1.8990	20	Lawfk	orph.				
No	0.9704	-0.9716	20	Lawfg	Aml				
Yes	1.4443	2.2114	21	Lawfk	R1	L3			
No	1.7605	-0.4112	21	Lawfc	Ama	L3	Amh	C2	
Yes	-0.5370	-0.8924	22	R2	L1	L2	orph.	orph.	
No	1.9616	2.5796	22	R6	L2	orph.			
Yes	-0.5405	-0.0530	23	R2	L1	L2	L3	sat.glia	
Yes	-0.3235	1.1560	23	Lawfa	L2	ep.glia			
No	1.7218	-0.8232	25	Lawfc	Aml	C2	Amh		
Yes	-0.5579	0.9757	28	Lawfa	L1	L3			
Yes	-0.5393	-1.7151	28	R3	L1	L2			
Yes	0.8150	-1.7251	29	Lawfe	Aml	Lawfj	Lawfd		
Yes	1.1374	-0.0325	29	Lawff	Amb	Ama	Lawfg	orph.	
Yes	0.8894	2.0197	29	R1	L1	L2	orph.		
Yes	0.8522	0.2589	29	Lawfg	Aml	Amb			
Yes	-1.0016	0.9161	29	R2	L1	L2	L3		
Yes	-1.3612	-0.7083	29	Aml	ep.glia				
Yes	-0.7729	-1.0445	31	Lawfb	R2	orph.			
Yes	1.6451	2.1609	31	R6	L1	L2	L3	ep.glia	
Yes	0.8197	-0.8289	33	Lawff	C3	Aml	L3	orph.	
Yes	-0.4920	-0.6778	34	Lawfh	L3	R2	L2		
Yes	-0.0429	1.4884	35	R1	L1	L2	L3		
Yes	0.2919	-0.4026	35	Lawfg	Lawfb	Aml	orph.		
Yes	-0.6663	-0.0220	36	R2	L1	L2	L3		
Yes	0.7686	0.4330	37	Lawfg	Amb	Amg	L3	Amh	
No	1.7978	-0.4536	37	Lawff	Aml	C2	Lawfc	orph.	
Yes	-0.8283	1.2166	38	Lawfa	R2	L3	orph.		
Yes	1.7501	1.2524	40	R6	L1	L2	L3		
Yes	0.5741	-0.3711	43	Lawfg	C2	Aml	L3	orph.	
Yes	-0.3373	-1.3135	43	Lawfh	Lawfd	L2	Aml	ep.glia	
Yes	-0.5171	-1.7475	43	R3	L1	L2	L3		
Yes	0.7256	-0.1145	44	Lawfg	Amg	C2	L3	Amb	
Yes	1.0128	0.0043	47	Lawfc	C2	orph.	Amg	Amh	
No	1.3379	-1.3883	48	Lawff	ep.glia	orph.			
No	-1.3095	-0.9357	48	Lawfb	T1	L3			
Yes	0.5497	-2.4376	50	Lawfe	Aml	L5	Amd	Amc	Ami
Yes	-0.4609	-2.4996	50	R4	L1	L2	orph.		

certain	x	y	section	pre	post1	post2	post3	post4	post5
Yes	1.0298	-0.9968	51	Lawff	Amh	orph.	C3		
Yes	-0.9604	1.7126	51	Amb	ep.glia				
Yes	1.0236	2.3078	51	R6	L2	Ama	ep.glia	orph.	
Yes	0.7818	1.9234	51	Lawfb	Ama	orph.	ep.glia		
Yes	0.6171	1.2066	52	Lawfb	L2	L3			
No	0.4738	-1.7708	54	Lawfe	Lawfj	Aml	orph.		
No	0.8237	-2.0102	55	Lawfe	Aml	Ami			
No	1.6262	0.7140	56	Lawfi	L3	Amg	ep.glia		
Yes	-0.3888	1.4890	56	R1	L1	L2	L3	ep.glia	
Yes	0.8450	2.5616	56	Ama	ep.glia				
No	0.7609	0.6606	57	C2	L2	Amg	Amb		
Yes	-1.5331	-0.3624	57	R2	L1	L2	T1	Aml	
No	-0.1787	-0.9490	58	C3	Aml	orph.			
Yes	0.2677	2.0642	58	R1	L2	orph.			
No	-0.4612	-2.3293	59	R4	L2	orph.			
Yes	-1.6489	-0.9319	60	R3	L1	L2	T1	Aml	
No	1.0756	-0.7249	61	Lawfc	Amg	Amh	T1		
Yes	-1.2184	-0.8055	61	R3	L1	orph.	L3	orph.	
Yes	-0.1694	-0.7625	66	C2	Aml	L2			
No	0.3576	-1.0477	66	C2	L2	Lawfj	orph.		
Yes	-1.1366	1.3951	66	R2	L1	L2	L3	Amb	
No	0.0786	1.3765	66	C2	L2	orph.			
Yes	1.0361	0.2814	67	Lawfi	L3	orph.			
Yes	1.0664	0.6086	69	Lawfi	ep.glia	L3			
Yes	-1.2214	-2.1008	69	R3	L2				
Yes	-1.0292	-0.4950	69	C2	Aml	L2			
Yes	-0.9246	-1.9844	71	Lawfd	L2	R3			
Yes	0.8850	-0.2064	73	Lawfj	L3	L2			
Yes	1.2439	0.5361	75	R6	L1	L2	L3	ep.glia	
Yes	-0.0829	1.4475	75	R1	L1	L2	ep.glia	orph.	
Yes	0.4220	-1.6315	76	R5	L1	L2	C2	orph.	
Yes	0.6789	2.1901	77	Ama	ep.glia				
Yes	-0.1589	-1.7793	79	R4	L1	L2	L3	ep.glia	
Yes	-0.9567	-1.4869	82	Lawfd	L2	L3	orph.	orph.	
Yes	-1.2392	2.4028	83	Amb	ep.glia				
Yes	-0.8610	1.0140	83	R2	L1	L2			
Yes	0.3445	-1.0854	84	R5	L1	L2	L3	Aml	
No	0.4581	0.4470	87	Lawfj	L2	L3	ep.glia		
Yes	1.2889	0.5400	87	R6	L1	L2	L3	ep.glia	
Yes	-0.9067	-0.8192	89	R3	L1	L2			
Yes	0.3643	0.7308	89	Lawfj	R6	L3	ep.glia		
Yes	-0.7698	1.0415	90	R2	L1	L2	ep.glia		

certain	x	y	section	pre	post1	post2	post3	post4	post5
Yes	0.2346	-0.2233	90	Lawfj	L3	ep.glia	T1		
Yes	-0.3048	1.6677	90	R1	L1	L2	L3		
No	0.4334	0.0688	91	Lawfj	T1	orph.			
Yes	-0.2663	-1.1512	93	R4	L1	L2	L3		
Yes	1.3895	-0.0097	94	R5	L1	L2			
Yes	1.0113	0.4987	94	R6	L1	L2	L3		
Yes	2.5622	-0.4050	96	Aml	ep.glia				
Yes	0.4422	-1.9357	97	Aml	R5	T1	ep.glia		
Yes	0.5419	-0.5896	98	R5	L1	L2	ep.glia	orph.	
Yes	0.7589	1.4812	98	R1	L2	L3	ep.glia		
No	-0.2265	-0.8121	99	Lawfj	L1	L2	orph.	R4	
Yes	1.0941	1.1719	99	R6	L1	L2			
Yes	1.8137	2.0096	100	Ama	T1	ep.glia			
Yes	-1.5205	-0.1892	103	Aml	C3	L3	T1		
Yes	0.4590	-1.6062	107	R5	L1	L2			
Yes	-0.7057	0.8628	109	R2	L1	L2	L3	ep.glia	
Yes	-0.2837	1.1736	110	R1	L1	L2	ep.glia		
Yes	0.0086	-1.8196	112	R4	L1	L2			
Yes	-1.1074	-0.5982	112	R3	L1	L2	L3		
Yes	1.7761	1.8267	113	Ama	T1	ep.glia			
Yes	1.0821	1.4926	114	R1	L1	L2			
Yes	-0.5733	2.2118	114	Amb	T1	ep.glia			
Yes	0.8784	0.3346	116	R6	L1	L2			
Yes	-0.9002	-1.2449	118	R4	L1	L2			
Yes	0.7065	0.6537	120	R6	L1	L2			
Yes	1.8349	-0.4127	120	R5	L1	ep.glia			
Yes	-0.1176	-1.0072	121	R4	L1	T1	orph.	ep.glia	
Yes	1.4899	0.0745	125	R6	L1				
Yes	-0.4126	1.5391	127	R2	L1	L2			
Yes	-1.1243	0.4438	130	R2	L1	L2	L3	ep.glia	
Yes	0.6121	-0.6591	131	R5	L1	L2			
Yes	2.5970	-0.5088	133	Aml	ep.glia				
Yes	-0.2421	-2.6037	134	Aml	L5	T1			
Yes	0.5342	2.8172	137	Amb	T1	ep.glia			
Yes	0.6896	0.9269	138	R1	L1	L2	Ama		
Yes	1.4212	1.8755	138	Ama	T1	ep.glia			
Yes	0.0639	-1.1990	139	R4	L2	Aml	ep.glia	orph.	
Yes	2.5326	-0.4861	140	Aml	L4	L3			
Yes	-0.4671	1.9999	141	R2	L1	L2	L3		
Yes	-1.2359	-0.3685	141	R3	L1	L2	orph.		
Yes	1.0158	0.6544	142	R6	L1	L2			
Yes	-0.2428	1.4418	142	R1	L1	L2			

certain	x	y	section	pre	post1	post2	post3	post4	post5
Yes	-0.0754	-2.3774	142	Aml	T1	ep.glia			
Yes	-1.8650	-2.0429	144	Aml	T1	R4	ep.glia		
Yes	-1.1322	-1.3921	145	R4	L1	L2			
Yes	-1.2168	0.5048	147	R2	L1	orph.			
Yes	-0.2846	2.3955	149	Amb	T1	ep.glia			
Yes	0.7666	0.8264	152	R1	L1	L2	ep.glia		
Yes	1.5427	1.6012	153	Ama	T1	ep.glia			
Yes	-1.5325	-1.1144	153	R3	L1	L2			
Yes	1.3403	-0.9287	155	R5	L1	L2			
Yes	1.1233	-0.3273	155	R6	L1	L2	L3	Aml	
Yes	0.1759	-1.2016	156	R4	L1	L2	ep.glia		
Yes	0.1015	1.1978	156	R1	L2	L3	orph.	ep.glia	
Yes	0.1212	-1.8218	157	R5	L1	L2			
Yes	-1.1239	-0.0426	158	R3	L1	orph.	ep.glia	Aml	
Yes	-1.3438	0.4716	161	R2	L1	L2	Aml	ep.glia	
Yes	0.1268	1.5998	162	R1	L1	L2	Amb	L3	
Yes	-0.9746	-1.4137	164	R4	L1	L2	Aml	T1	
No	0.0681	2.0953	165	Amb	T1	L3	ep.glia		
Yes	-0.5835	1.2328	170	R2	L1	L2	L3	ep.glia	
No	0.4530	-2.8098	171	C2	L5	Ami			
Yes	0.7269	1.4246	172	R1	L2	Ama	orph.		
No	0.8098	-0.3799	174	R6	L1	L2	L3	ep.glia	
Yes	0.3222	-1.9860	176	R5	L2	orph.	Aml		
Yes	-2.0637	-0.2750	177	Aml	T1	ep.glia			
Yes	-1.1945	-2.0731	178	Aml	T1	ep.glia			
Yes	1.0397	0.7166	180	R6	L1	L2	Ama	ep.glia	
No	0.4456	0.3692	181	C3	Ama	Aml	L1	ep.glia	
Yes	-1.5373	-1.5653	182	R3	L1	L2	Aml	orph.	
Yes	-0.3283	1.8447	182	R2	L1	L2	Amb	ep.glia	
No	-1.1529	-1.5839	182	C3	Aml	T1	orph.		
Yes	-0.0544	1.4043	183	R1	L1	L2	Ama		
Yes	1.0566	-0.2513	184	R6	L1	L2	ep.glia		
Yes	-0.6298	-1.5905	184	R4	L1	L2	L3	Aml	
Yes	-1.2487	-0.1522	185	R3	L1	L2	Aml	Aml	
Yes	1.4246	-0.6732	186	R5	L1	L2	Aml	ep.glia	
Yes	0.1846	-1.4172	186	R4	L1	L2	Aml		
Yes	0.7561	-1.4421	187	R5	L1	L2			
Yes	-1.2589	0.4923	187	R2	L1	L2	Aml	Aml	
No	0.5949	-2.2853	187	Aml	ep.glia				
Yes	-0.3960	2.2467	188	Amb	ep.glia				
Yes	1.1294	0.7891	191	R6	L1	L2	orph.	ep.glia	
Yes	1.1418	1.5269	191	Ama	T1	ep.glia			

certain	x	y	section	pre	post1	post2	post3	post4	post5
Yes	0.6733	1.1050	192	R1	L1	L2	Ama	ep.glia	
Yes	-1.0760	0.6147	194	R2	L1	L2	Aml	ep.glia	
Yes	-1.2408	-1.4501	195	R3	L2	L3	Aml	T1	
Yes	-0.6686	-0.1923	198	C3	T1	L1	L2		
Yes	0.8424	1.4745	202	R1	L1	L2	Ama		
Yes	1.3224	1.4123	203	R6	L1	L2	Ama	ep.glia	
No	-0.4384	0.4761	203	C3	L1	L2	Ama	Aml	
Yes	0.0691	-1.1736	205	R4	L1	L2	Aml	L3	
Yes	2.0124	-1.1553	206	Aml	T1	ep.glia			
Yes	-0.8520	-1.4095	206	R3	L1	L2	Aml	ep.glia	
Yes	-1.1718	-0.6905	207	R3	L1	L2	Aml	ep.glia	
Yes	1.7077	-0.2010	208	R6	L1	L2	L3	Aml	
Yes	-0.9335	0.5492	208	R2	L2	L3	orph.		
No	-0.5863	-0.5172	208	C3	L1	Aml	L3	ep.glia	
Yes	1.2701	-0.6724	209	R5	L1	L2	Aml	ep.glia	
Yes	-0.2844	1.2736	212	R1	L2	Amb	orph.		
Yes	2.1301	-0.5370	213	Aml	T1	L3	ep.glia		
Yes	0.6669	0.3496	213	R6	L1	L2			
Yes	-0.7476	0.3305	215	C3	L2	Aml	ep.glia		
Yes	-1.3366	-0.3825	215	Aml	ep.glia				
Yes	0.3808	-2.4037	215	Aml	L5	T1			
Yes	1.9830	0.5658	216	Amg	ep.glia				
Yes	0.6624	-1.3872	216	R5	Aml	orph.	L2		
Yes	0.0451	-1.2572	217	R4	L1	L2	Aml	L3	
Yes	-0.4943	1.6444	217	R2	L2	Ama	Amb	L3	
Yes	-1.4279	0.7079	218	R2	L1	L2	Aml	T1	
Yes	-0.7397	-1.4497	218	Aml	L3	ep.glia			
Yes	-0.0338	1.7862	220	R1	L2	L3	orph.		
Yes	-0.5085	2.1270	221	Amb	ep.glia				
Yes	0.5853	1.3269	222	Ama	ep.glia	L3			
Yes	-1.0621	0.0180	225	R3	L1	L2	ep.glia	Aml	
Yes	0.6880	-1.3592	228	Aml	ep.glia				
Yes	-0.8753	-1.4527	230	R3	L1	L2	Aml	ep.glia	
No	0.9812	2.6948	231	Ama	ep.glia				
Yes	-0.2500	-1.6578	232	R4	L1	L2	ep.glia	Aml	
Yes	0.5276	1.3861	233	R1	L1	L2	Ama	ep.glia	
Yes	0.8899	1.2185	234	R6	L1	L2	Ama		
Yes	-0.7443	1.7948	235	R2	L1	L2	Amb	ep.glia	
Yes	0.4913	-2.7009	238	Aml	T1	L5			
Yes	0.4603	-0.2023	238	R6	L1	L2	Ama	L3	
Yes	-1.0127	2.1224	239	Amb	T1	ep.glia			
Yes	0.0661	-1.2876	239	R4	L2	orph.	L3		

certain	x	y	section	pre	post1	post2	post3	post4	post5
Yes	-1.4591	0.3430	239	Aml	ep.glia				
Yes	0.6853	-1.9773	240	Aml	T1	ep.glia			
Yes	-0.8965	0.3276	241	Aml	ep.glia				
Yes	-0.3385	1.8652	241	R1	L1	L2	Amb	ep.glia	
Yes	1.3950	-0.0118	244	R6	L1	L2	Amg		
No	-0.6696	-1.7788	244	Aml	T1	ep.glia			
Yes	-0.7510	-0.2179	245	R3	L1	L2	Aml		
Yes	1.3165	-0.3604	249	R5	L1	L2	Amg		
Yes	-1.1218	-0.1154	251	Aml	ep.glia				
Yes	-0.9792	0.4860	251	R2	L1	L2	Aml		
Yes	0.6915	1.2549	255	R6	L1	L2	Ama		
Yes	0.7031	2.2144	256	Ama	T1	ep.glia			
Yes	-0.9337	-2.2620	256	Aml	T1	ep.glia			
Yes	1.7447	0.2800	256	Amg	T1	ep.glia			
Yes	0.9627	-1.8791	257	R5	L1	L2	Aml	Aml	
Yes	0.5774	-2.0233	258	R4	L1	L2	Aml	Aml	
Yes	-1.1921	1.7418	261	R2	L1	L2			
Yes	0.4881	1.3884	261	R1	L1	L2	L3		
Yes	-0.2009	-1.4466	262	R4	L1	L2	Aml		
Yes	-0.8713	1.1993	263	R2	L1	L2	Aml	Amb	
Yes	-0.6667	1.9991	263	R1	L1	L2	Amb	ep.glia	
Yes	-0.5807	-1.4558	264	R3	L1	L2	Aml		
Yes	1.1987	0.2368	264	R6	L2	Amg	orph.		
Yes	-0.8110	-0.4653	265	R3	L1	L2	Aml	C3	
Yes	0.6320	2.2968	267	Ama	T1	ep.glia			
Yes	0.6551	-0.9240	269	R5	L1	L2	Aml		
Yes	-1.1739	0.4524	269	R2	L1	L2	Aml		
Yes	1.4711	-0.0482	272	R5	L2	orph.	L3		
Yes	-1.0594	1.8165	273	Amb	ep.glia				
Yes	0.1426	-1.4276	274	R4	L1	L2	Aml		
Yes	1.1098	-2.4568	274	R5	L1	orph.	Aml		
Yes	-0.3542	-1.2431	275	C3	L1	orph.	Aml		
Yes	-1.2520	0.1799	281	Aml	R2	orph.			
Yes	0.3592	1.5548	282	R1	L1	L2	Ama	orph.	
Yes	0.6985	2.0912	284	Ama	T1	orph.			
Yes	-1.0507	1.6556	285	R2	L1	L2	Amb	Amb	
Yes	0.5109	-2.2085	286	Aml	ep.glia	T1			
No	1.6075	0.3940	287	Amg	T1	L3			
Yes	1.0681	0.0406	287	R5	L1	L2	Aml	L3	
Yes	1.0662	0.4642	290	R6	L1	L2	Amg		
Yes	-0.6698	1.9398	290	R1	L1	L2	Amb	Amb	
Yes	-0.4534	-1.1203	293	R4	L1	L2	Aml		

certain	x	y	section	pre	post1	post2	post3	post4	post5
Yes	-0.8316	-2.1929	293	Aml	ep.glia				
Yes	0.2904	-1.2393	294	R4	L1	L2	Aml	ep.glia	
Yes	0.6190	-1.2951	294	R5	L1	L2	Aml	ep.glia	
Yes	-0.6212	-0.4345	295	R3	L1	L2	Aml		
Yes	2.0818	0.4819	296	Amg	L4	L3			
Yes	1.7406	-0.6972	297	Aml	T1	ep.glia			
No	2.1858	0.4055	303	Amg	L4	L3			
Yes	0.5116	1.7808	304	R1	L1	L2	Ama	Ama	
Yes	0.9691	1.2963	310	R6	L1	L2	Ama		
Yes	1.2789	-0.4471	311	R5	L1	L2			
Yes	-0.7609	2.3305	311	Amb	T1	ep.glia			
Yes	-1.2633	1.0708	312	R2	L1	L2	Aml	Aml	
Yes	-1.2143	-1.3817	315	Aml	T1	ep.glia			
Yes	0.4783	-0.7865	315	C3	Aml	Amg	L1		
Yes	-0.6197	1.2931	318	R1	L1	L2	ep.glia		
Yes	-0.9485	-1.1012	319	R3	L1	L2	Aml		
Yes	1.3579	-0.0162	319	R6	L1	L2	Amg		
Yes	1.1037	1.8562	319	Ama	T1	ep.glia			
Yes	-0.5957	-2.3076	322	Aml	T1	ep.glia			
No	0.5823	1.8650	322	Ama	R1	ep.glia	T1		
Yes	-0.9001	0.5409	325	R3	L1	L2	Aml		
Yes	0.6681	-0.3604	327	C3	Amg	Ama	Aml	L2	
Yes	0.4571	-1.3598	328	R4	L1	L2	Aml		
Yes	-0.8759	1.7588	328	R2	L1	L2	Amb	ep.glia	
Yes	1.0335	0.2448	329	R6	L2	Amg	L1	Ama	
Yes	-0.4177	1.8049	331	R1	L1	L2	ep.glia	Amb	
Yes	-1.5027	0.6517	331	Aml	T1	ep.glia			
Yes	0.7851	-1.5307	331	R5	L1	L2	Aml	Aml	
Yes	1.4727	-0.5918	334	R5	L1	L2	Amg	L3	
Yes	-0.4566	-1.1123	339	R4	L1	L2	Aml	ep.glia	
Yes	0.2998	-0.7651	339	Amg	ep.glia				
Yes	0.3494	1.3863	339	R1	L1	L2	Ama	ep.glia	
Yes	-0.7275	-0.8489	340	R3	L1	L2	Aml	Aml	
Yes	0.7287	1.1377	343	R6	L1	L2	Ama	Ama	
Yes	-1.4749	0.4554	345	R3	L1	L2	orph.	Aml	
Yes	0.6722	-0.4530	346	Amg	ep.glia				
Yes	-0.7130	1.5865	348	R2	L1	L2	Amb	Amb	
Yes	0.8592	-2.2330	350	R5	L1	L2	Aml	Aml	
Yes	0.5492	-1.5324	350	R4	L1	L2	Amg		
Yes	-1.2160	0.7150	351	R2	L1	L2	Aml	Aml	
Yes	0.0382	-0.9747	352	R4	L1	L2	Amg	Amg	
Yes	-1.9837	0.5098	355	Aml	ep.glia				

certain	x	y	section	pre	post1	post2	post3	post4	post5
Yes	-0.2211	1.6908	356	R1	L1	L2	Amb	Amb	
No	-0.1350	-2.7396	359	Aml	ep.glia	T1			
Yes	1.5488	-0.5017	361	Amg	orph.	ep.glia	R5		
Yes	-1.6672	0.8715	362	Aml	ep.glia	T1			
No	0.6162	-0.5453	363	C3	Amg	Ama	L2		
No	-0.6282	2.0678	364	Amb	T1	ep.glia			
Yes	1.2435	-0.4653	367	R6	L1	L2	Amg	Amg	
Yes	1.3339	1.1774	369	R6	L1	L2	Ama	Ama	
Yes	0.2631	-0.6983	370	C3	L2	Amg			
No	-0.7909	-0.4441	370	R3	L1	L2	Aml	ep.glia	
Yes	-0.8846	2.2990	373	Amb	ep.glia				
Yes	0.8532	-1.6846	374	R5	L1	L2	Aml	ep.glia	
Yes	0.5884	-1.7995	375	R4	L1	L2	Aml	Amg	
Yes	0.4520	1.2819	375	R1	L1	L2	Ama	Amb	
Yes	1.4272	-0.9595	376	R5	L1	L2	Amg	ep.glia	
Yes	-0.4663	-1.2140	378	R4	L1	L2	Aml	Aml	
Yes	1.0749	-0.3587	380	R6	L1	L2	Amg	orph.	
No	-1.1801	0.7727	381	Aml	L2	T1	ep.glia		
Yes	1.9793	-0.6226	383	Amg	L4	L3			
No	0.4330	-0.4865	385	C3	Aml	L2	orph.	Ama	
Yes	-1.0674	1.4355	385	R2	L1	L2	Aml		
Yes	0.5632	-1.0383	385	R4	L1	L2			
Yes	-1.4872	0.8928	386	R2	L1	L2	Aml	Aml	
Yes	-0.8282	0.0588	387	R3	L1	L2	C3	Aml	
Yes	0.0230	0.9112	388	R1	L1	L2	Amb		
Yes	1.7236	-0.5801	389	Amg	T1	ep.glia			
Yes	1.1470	1.1001	389	Ama	T1	ep.glia			
Yes	0.4565	0.5740	390	R6	L1	L2	Ama	Amb	
Yes	0.8858	-0.7945	392	R5	L1	L2	Aml	Amg	
Yes	-0.0466	-2.3126	393	Aml	T1	ep.glia			
Yes	0.9741	1.6377	394	Ama	T1	ep.glia			
Yes	-0.9278	-1.2374	396	Aml	ep.glia				
Yes	-0.6636	1.9441	397	R1	L1	L2	Amb	Amb	
No	-1.9284	0.5057	397	Aml	T1	ep.glia			
Yes	0.2602	-2.2533	397	Aml	ep.glia				
Yes	-0.2653	-0.5155	399	R4	L1	L2	Amg		
Yes	1.2963	-0.6307	402	R6	L2	L3	ep.glia	Amg	
No	-0.9900	1.0947	404	C3	Amb	L2	m.glia a	Aml	
Yes	0.7785	-0.2056	406	R6	L2	m.glia b	L1	ep.glia	
Yes	-1.1196	-0.8602	409	R3	L2	L1	Aml	Aml	
Yes	-0.6817	-0.2517	410	R3	L1	L2	Aml	ep.glia	
Yes	1.0147	1.5782	411	R1	L1	L2	Ama	Ama	

certain	x	y	section	pre	post1	post2	post3	post4	post5
Yes	-0.5787	1.7270	411	Amb	ep.glia	T1			
Yes	1.1984	1.1513	412	R6	L1	L2	Ama		
No	-0.9787	1.0733	415	Amb	L2	ep.glia			
Yes	-1.6406	0.3000	417	R3	L1	L2	Aml	Aml	
Yes	-0.3820	-2.1366	417	Aml	T1	ep.glia			
Yes	-1.2400	-1.3607	418	Aml	ep.glia				
Yes	-1.1812	1.2778	422	R2	L1	L2	Amb	ep.glia	
Yes	0.4804	-1.7602	422	R5	L1	L2			
Yes	-1.3943	0.7455	423	R2	L1	L2	Amb		
Yes	0.3308	-1.1996	425	R4	L1	L2	Aml		
Yes	1.0143	1.4124	427	R1	L1	L2	Ama		
Yes	-0.4055	1.8836	427	Amb	ep.glia				
Yes	-0.3382	-1.9764	430	R4	L1	L2	Aml	Aml	
Yes	1.6249	-0.3449	431	R6	L1	L2	Amg	Amg	
Yes	1.4070	-0.9623	434	R5	L1	L2	orph.	Amg	
Yes	0.1647	1.1714	435	R1	L1	L2	m.glia a	Amb	
Yes	0.9521	0.4708	435	R6	L1	L2	Ama		
Yes	-1.0529	1.9411	436	Amb	T1	ep.glia			
Yes	-1.0762	-1.0580	438	Aml	ep.glia				
Yes	-0.9088	-0.3911	440	R3	L1	L2	Aml		
Yes	-1.5380	0.0597	444	R3	L1	L2	Aml	Aml	
Yes	-1.6100	0.3909	445	R2	L1	L2	Aml	orph.	
Yes	-1.1264	1.9347	445	Amb	ep.glia				
Yes	1.3521	1.0968	447	Ama	T1	ep.glia	L2		
Yes	0.4469	-1.1910	447	R5	L1	L2	Aml	Aml	
Yes	1.6497	-1.2468	447	Amf	ep.glia				
No	0.8980	-0.5534	449	L4-y	L2	L4	R5		
Yes	-0.0731	-0.6003	450	R4	L1	L2	orph.		
Yes	1.3963	1.4209	450	Ama	ep.glia				
Yes	-0.7465	-0.5605	451	R4	L1	L2	orph.	Aml	
Yes	0.4309	1.0213	456	R1	L1	L2	Amb		
Yes	0.8153	-0.1753	456	L4-y	R1	R5			
Yes	-2.0057	0.1595	456	Aml	T1	ep.glia			
Yes	-0.1821	-1.4136	459	R4	L1	L2	Aml		
Yes	1.2587	-0.8034	460	R5	L1	L2	Amf		
Yes	1.9035	-0.4810	460	Amg	T1	L3	L4	ep.glia	
Yes	1.7098	1.0371	462	R6	L1	L2	Ama	Ama	
Yes	0.0529	1.7305	464	R1	L1	L2	L3	Amb	
Yes	-0.8686	1.0822	465	R2	L1	L2	Amb	Amb	
Yes	1.7936	1.4134	466	Ama	ep.glia				
Yes	1.6890	-1.3005	469	Amf	T1	ep.glia			
Yes	-2.0372	0.2309	469	Aml	ep.glia				

certain	x	y	section	pre	post1	post2	post3	post4	post5
Yes	-1.0328	-0.4077	469	C3	Aml	L2	R3		
Yes	1.2226	-0.0986	471	R6	L1	L2	Amg	m.glia b	
No	-1.0357	0.3344	473	L2	R2	ep.glia	T1		
Yes	0.5019	-0.8126	473	R5	L1	L2	Aml	Aml	
Yes	1.8372	-0.3883	474	R6	L1	L2	L3	L3	
Yes	-0.8202	-1.7807	475	Aml	ep.glia				
Yes	1.3374	1.6355	475	R1	L1	L2	Ama		
Yes	-0.9605	1.3405	476	R2	L1	L2	Amb		
Yes	1.3421	-1.2918	477	R5	L1	L2	Amf	Amf	
Yes	-1.7842	0.9268	479	R2	L1	L2	Aml		
Yes	-0.1513	-0.9429	480	R4	L1	L2	Aml		
Yes	1.8785	-1.3929	481	Amf	T1	ep.glia	L3		
Yes	1.5918	1.1544	483	R6	L1	L2	Ama	Ama	
Yes	-2.0848	0.8320	483	Aml	L1	orph.	ep.glia	T1	
Yes	-1.0199	-1.6552	485	Aml	T1	ep.glia	R4		
Yes	-1.3934	0.2473	487	R3	L1	L2			
Yes	0.1923	-2.0104	489	R5	L1	L2	Aml	ep.glia	
No	-1.9761	0.9574	491	Aml	ep.glia	T1			
Yes	-1.1755	-1.9638	492	Aml	ep.glia				
Yes	0.3257	-0.5326	493	L4-y	R5	ep.glia	L5	L3	
Yes	-0.8321	0.9783	495	R2	L1	L2	Amb	ep.glia	
Yes	-1.7055	0.8471	496	R2	L2	Aml			
Yes	-0.4647	-0.4683	497	L4+x	L4	R4	L2	ep.glia	
Yes	0.5211	1.1375	497	R1	L1	L2	Ama		
No	-0.1601	-0.4569	498	L4+x	L1	L4-y	L5	L2	
Yes	1.4837	-0.1851	499	R6	L1	L2	Amg		
Yes	1.1683	-0.8061	500	R5	L1	L2	m.glia b	L3	
No	0.8901	-0.0445	501	L4-y	L4+x	R6	orph.	m.glia b	L4
Yes	0.0973	1.6658	502	R1	L1	L2	Amb	Amb	
Yes	-0.8575	0.2026	502	L4	L2	orph.			
Yes	-0.9877	-0.5662	502	R3	L2	Aml			
Yes	1.0660	1.3104	504	R1	L1	L2	ep.glia	Ama	
Yes	-2.1084	0.2750	504	R3	L2	Aml			
Yes	0.0144	0.7866	507	L2	L4	L1	L4-y	L4+x	
Yes	-0.1778	-1.5136	507	R4	L1	L2	Aml	Aml	
Yes	0.1764	-1.6634	508	R5	L1	L2	Aml	Aml	
Yes	0.8476	0.0521	510	L4+x	L4-y	orph.	R6		
Yes	0.7864	0.8075	511	L4+x	R6	R1	Ama		
Yes	1.0818	1.1746	516	Ama	T1	ep.glia			
Yes	-0.8402	-0.9148	516	R4	L1	L2	Aml		
Yes	0.8470	-1.8954	517	Aml	T1	ep.glia			
Yes	1.3120	-1.1762	517	Amf	T1	L3			

certain	x	y	section	pre	post1	post2	post3	post4	post5
Yes	-1.2602	0.1868	518	R3	L1	L2	Aml	Aml	
Yes	-1.5888	0.7572	518	R2	L1	L2	orph.	Aml	
Yes	1.6918	-0.3288	519	R6	L1	Amg	orph.	L3	
Yes	-0.0108	1.0881	522	L2	R1	L4+x	L1	L4	
Yes	0.0528	2.0285	524	Amb	ep.glia				
Yes	0.4822	1.0593	526	R1	L1	L2	Amb		
Yes	1.1851	-1.5166	529	Amf	T1	ep.glia			
Yes	-0.0595	-1.6302	531	R4	L1	L2	L3	Aml	
Yes	1.2177	-0.6382	531	R5	L1	L2	Amf	ep.glia	
Yes	1.0689	0.1926	531	R6	L2	Ama	orph.		
Yes	0.3443	-1.5072	532	R5	L1	L2	L3	Aml	
No	-0.6763	0.9078	535	L2	L4+x	L4-y	L4		
Yes	-0.0369	2.0477	536	Amb	T1	ep.glia			
Yes	1.1610	0.8047	541	R6	L1	L2	Ama	orph.	
Yes	2.0553	-0.2275	544	R6	L1	L2	orph.	Amf	
No	-0.4903	-0.4972	545	L4+x	L3	L2	ep.glia		
Yes	-0.8572	-0.6397	547	R3	L1	L2	Aml	Aml	
Yes	0.7300	-1.5449	547	Amf	Aml	ep.glia			
Yes	0.9868	-0.2398	548	R5	L1	L2	orph.	ep.glia	
Yes	0.3074	-0.8195	549	R5	L1	L2	Aml		
No	1.7028	-0.4257	554	L4	ep.glia	orph.	m.glia b	L2	
Yes	-1.7568	0.8763	554	Aml	ep.glia				
Yes	-0.0952	-1.0767	554	R4	L1	L2	Aml	ep.glia	
Yes	-0.8144	0.4423	554	R3	L1	L2	Aml		
Yes	-0.6072	-0.3792	555	L4+x	R3	L2	ep.glia		
Yes	0.8188	1.1832	555	R1	L1	L2	orph.	ep.glia	
Yes	-0.7126	-1.4456	555	R4	L2	Aml	ep.glia		
Yes	1.5256	-0.1312	555	R6	L1	L2	ep.glia	L4	
Yes	0.7324	-1.9074	560	C2	Ami	Ame			
Yes	-0.6130	1.3972	560	R2	L1	L2	ep.glia	ep.glia	
Yes	-1.8877	0.3339	561	Aml	T1	ep.glia			
Yes	0.6573	-1.0982	567	Aml	C2	L5			
Yes	-1.4383	1.0656	567	R2	L1	L2	Aml		
Yes	-0.5651	1.1153	569	R2	L1	L2	Aml		
Yes	1.2639	0.7495	569	R6	L1	L2	Ama		
Yes	-0.8922	0.4178	572	R3	L1	L2			
Yes	0.1049	-1.3988	574	R4	L2	orph.	Aml	L3	
Yes	-0.4144	1.2022	577	L2	R2				
No	0.1958	-0.4687	578	L4+x	L1	L5	L4	L2	
No	1.5375	0.8364	579	Ama	Amj	m.glia b	L2		
Yes	1.3665	-0.2269	580	R6	L1	L2	L4		
No	0.8607	-1.2467	581	Aml	L3	ep.glia			

certain	x	y	section	pre	post1	post2	post3	post4	post5
Yes	1.1422	0.1080	582	L4-y	R6	L2	orph.		
Yes	0.4121	-0.6887	585	L4	L5	orph.	L2	R5	Amj
Yes	-0.3541	-1.4419	586	R4	L1	L2	Aml	orph.	
No	-0.1495	-0.2701	586	L4	L5	L2	orph.		
No	0.2105	-0.9056	591	L4-y	L4	Amj	m.glia b	L2	
No	-0.1936	-1.1783	593	L4-y	R4	L2			
Yes	-1.1097	0.1826	596	R3	L1	L2	Amk	ep.glia	
Yes	0.0177	0.5175	598	L2	L1	L4+x	L4		
Yes	-0.1187	-0.1149	598	L2	L5	L4-y	L4+x	L4	
Yes	-0.3332	0.9422	599	R2	L1	L2			
Yes	-0.6231	-1.2433	602	R3	L1	L2	Aml		
No	-0.0103	-0.5488	604	L4-y	R3	L5	ep.glia		
Yes	0.0743	-0.3007	608	L4+x	R3	L4-y	L5	L2	
Yes	-0.3112	0.5425	610	L4-y	R2	R3	L2	m.glia a	
Yes	-0.6631	0.0930	613	R3	L1	L2	Aml	Amk	

Table A.1: Synaptic contacts in the cartridge: *certain* indicates if the synapse is certain (Yes) or uncertain (No). x and y show the position of each synapse in μm from the center of the cartridge. *Section* indicates the section where the synapse has been annotated. *Pre* indicates the presynaptic cell. *Post* indicates the postsynaptic partners, their order is irrelevant.

Appendix B

2D radii

Element	Radius ($10^{-1}\mu m$)	Element	Radius ($10^{-1}\mu m$)
R1	7.45	C2	2.10
R2	6.64	C3	2.67
R3	6.58	T1 a	1.80
R4	6.66	T1 b	1.91
R5	7.02	T1 c	2.15
R6	7.62	T1 d	2.18
L1	5.47	T1 e	2.36
L2	7.68	T1 f	1.96
L3	4.26	La wf a	2.59
L4	2.48	La wf b	3.99
L4col a	3.29	La wf c	4.00
L4col b	3.81	La wf d	2.30
L5	1.63	La wf e	3.22
Am b	3.12	La wf f	3.98
Am l 1	3.20	La wf g	4.27
Am l 2	3.27	La wf h	2.50
Am l 3	4.00	La wf i	2.50
Am g	2.73	La wf j	3.36
Am a	3.55	La wf k	3.83

Table B.1: Sizes of the elements in the 2D model

Appendix C

2D connectivity matrix

	R1	R2	R3	R4	R5	R6	L1	L2	L3	L4	L4col a	L4col b	L5	Am b	Am l 1	Am l 2	Am l 3	Am g	Am a
R1	0	0	0	0	0	0	40	47	11	0	1	1	0	19	0	0	0	0	18
R2	0	0	0	0	0	0	43	47	10	0	0	1	0	16	23	0	0	0	1
R3	0	0	0	0	0	0	38	40	4	0	2	2	0	0	18	20	0	0	0
R4	0	0	0	0	0	0	38	42	8	0	1	1	0	0	0	16	18	5	0
R5	0	0	0	0	0	0	38	39	6	1	0	3	0	0	0	0	27	6	0
R6	0	0	0	0	0	0	46	49	13	2	2	2	0	1	0	0	2	14	22
L1	40	43	38	38	38	46	0	3	0	0	2	0	0	0	1	0	0	0	0
L2	47	47	40	42	39	49	3	0	0	9	11	8	1	1	1	0	0	0	2
L3	11	10	4	8	6	13	0	0	0	0	1	1	0	1	1	1	3	5	1
L4	0	0	0	0	1	2	0	9	0	0	2	3	2	0	0	0	1	4	0
L4col a	1	0	2	1	0	2	2	11	1	2	0	4	3	0	0	0	0	0	1
L4col b	1	1	2	1	3	2	0	8	1	3	4	0	2	0	0	0	0	0	0
L5	0	0	0	0	0	0	0	1	0	2	3	2	0	0	0	0	4	0	0
Am b	19	16	0	0	0	1	0	1	1	0	0	0	0	0	0	0	0	0	0
Am l 1	0	23	18	0	0	0	1	1	1	0	0	0	0	0	0	0	0	0	0
Am l 2	0	0	20	16	0	0	0	0	1	0	0	0	0	0	0	0	0	0	0
Am l 3	0	0	0	18	27	2	0	0	3	1	0	0	4	0	0	0	0	0	0
Am g	0	0	0	5	6	14	0	0	5	4	0	0	0	0	0	0	0	0	0
Am a	18	1	0	0	0	22	0	2	1	0	1	0	0	0	0	0	0	0	0
C2	0	0	0	0	1	0	0	6	0	0	0	0	1	1	0	2	1	1	1
C3	0	0	3	0	0	0	6	9	1	0	0	0	0	1	5	4	3	4	5
T1 a	0	0	0	0	0	0	0	0	0	0	0	0	0	8	0	0	0	0	0
T1 b	0	2	0	0	0	0	0	0	0	0	0	0	0	0	6	0	0	0	0
T1 c	0	0	2	2	0	0	0	0	0	0	0	0	0	0	0	7	0	0	0
T1 d	0	0	0	0	0	0	0	0	0	0	0	0	0	0	0	0	9	0	0
T1 e	0	0	0	0	0	0	0	0	0	0	0	0	0	0	0	0	3	3	0
T1 f	0	0	0	0	0	0	0	0	0	0	0	0	0	1	0	0	0	0	13
La wf a	0	1	0	0	0	0	1	1	2	0	0	0	0	0	0	0	0	0	0
La wf b	0	1	0	0	0	0	0	1	2	0	0	0	0	0	0	0	0	0	1
La wf c	0	0	0	0	0	0	0	0	1	0	0	0	0	0	0	0	1	2	1
La wf d	0	0	1	0	0	0	0	2	1	0	0	0	0	0	0	0	0	0	0
La wf e	0	0	0	0	0	0	0	0	0	0	0	0	1	0	0	0	4	0	0
La wf f	0	0	0	0	0	0	0	0	1	0	0	0	0	1	0	0	2	0	1
La wf g	0	0	0	0	0	0	0	0	4	0	0	0	0	3	0	0	4	2	1
La wf h	0	1	0	0	0	0	0	2	1	0	0	0	0	0	0	1	0	0	0
La wf i	0	0	0	0	0	0	0	0	3	0	0	0	0	0	0	0	0	1	0
La wf j	0	0	0	1	0	1	1	3	4	0	0	0	0	0	0	0	0	0	0
La wf k	2	0	0	0	0	0	0	0	2	0	0	0	0	0	0	0	0	0	0

Table C.1: Symmetric connectivity matrix for the 2D model (Part A)

	C2	C3	T1 1	T1 2	T1 3	T1 4	T1 5	T1 6	Lawf a	Lawf b	Lawf c	Lawf d	Lawf e	Lawf f	Lawf g	Lawf h	Lawf i	Lawf j	Lawf k
R1	0	0	0	0	0	0	0	0	0	0	0	0	0	0	0	0	0	0	2
R2	0	0	0	2	0	0	0	0	1	1	0	0	0	0	0	1	0	0	0
R3	0	3	0	0	2	0	0	0	0	0	0	1	0	0	0	0	0	0	0
R4	0	0	0	0	2	0	0	0	0	0	0	0	0	0	0	0	0	1	0
R5	1	0	0	0	0	0	0	0	0	0	0	0	0	0	0	0	0	0	0
R6	0	0	0	0	0	0	0	0	0	0	0	0	0	0	0	0	0	1	0
L1	0	6	0	0	0	0	0	0	1	0	0	0	0	0	0	0	0	1	0
L2	6	9	0	0	0	0	0	0	1	1	0	2	0	0	0	2	0	3	0
L3	0	1	0	0	0	0	0	0	2	2	1	1	0	1	4	1	3	4	2
L4	0	0	0	0	0	0	0	0	0	0	0	0	0	0	0	0	0	0	0
L4col a	0	0	0	0	0	0	0	0	0	0	0	0	0	0	0	0	0	0	0
L4col b	0	0	0	0	0	0	0	0	0	0	0	0	0	0	0	0	0	0	0
L5	1	0	0	0	0	0	0	0	0	0	0	0	1	0	0	0	0	0	0
Am b	1	1	8	0	0	0	0	1	0	0	0	0	0	1	3	0	0	0	0
Am l 1	0	5	0	6	0	0	0	0	0	0	0	0	0	0	0	0	0	0	0
Am l 2	2	4	0	0	7	0	0	0	0	0	0	0	0	0	0	1	0	0	0
Am l 3	1	3	0	0	0	9	3	0	0	0	1	0	4	2	4	0	0	0	0
Am g	1	4	0	0	0	0	3	0	0	0	2	0	0	0	2	0	1	0	0
Am a	1	5	0	0	0	0	0	13	0	1	1	0	0	1	1	0	0	0	0
C2	0	0	0	0	0	0	0	0	0	0	3	0	0	1	2	0	0	1	0
C3	0	0	0	1	1	0	0	0	0	0	0	0	0	2	0	0	0	0	0
T1 a	0	0	0	0	0	0	0	0	0	0	0	0	0	0	0	0	0	0	0
T1 b	0	1	0	0	0	0	0	0	0	0	0	0	0	0	0	0	0	0	0
T1 c	0	1	0	0	0	0	0	0	0	1	0	0	0	0	0	0	0	0	0
T1 d	0	0	0	0	0	0	0	0	0	0	1	0	0	0	0	0	0	0	0
T1 e	0	0	0	0	0	0	0	0	0	0	0	0	0	0	0	0	0	1	0
T1 f	0	0	0	0	0	0	0	0	0	0	0	0	0	0	0	0	0	0	0
La wf a	0	0	0	0	0	0	0	0	0	0	0	0	0	0	0	0	0	0	0
La wf b	0	0	0	0	1	0	0	0	0	0	0	0	0	0	1	0	0	0	0
La wf c	3	0	0	0	0	1	0	0	0	0	0	0	0	1	0	0	0	0	0
La wf d	0	0	0	0	0	0	0	0	0	0	0	0	1	0	0	1	0	0	0
La wf e	0	0	0	0	0	0	0	0	0	0	0	1	0	0	0	0	0	2	0
La wf f	1	2	0	0	0	0	0	0	0	0	1	0	0	0	1	0	0	0	0
La wf g	2	0	0	0	0	0	0	0	0	1	0	0	0	1	0	0	0	0	0
La wf h	0	0	0	0	0	0	0	0	0	0	0	1	0	0	0	0	0	0	0
La wf i	0	0	0	0	0	0	0	0	0	0	0	0	0	0	0	0	0	0	0
La wf j	1	0	0	0	0	0	1	0	0	0	0	0	2	0	0	0	0	0	0
La wf k	0	0	0	0	0	0	0	0	0	0	0	0	0	0	0	0	0	0	0

Table C.2: Symmetric connectivity matrix for the 2D model (Part B)

Appendix D

3D radii

Element	Radius ($10^{-1}\mu m$)		
	Distal	Central	Proximal
R1	8.90	7.21	6.02
R2	7.47	6.65	5.74
R3	6.30	6.97	6.15
R4	6.74	7.02	5.82
R5	7.35	7.12	6.42
R6	8.64	7.47	6.73
L1	5.59	5.43	5.42
L2	7.11	8.01	7.58
L3	5.43	4.11	3.28
L4	2.21	2.20	3.07
L4col a	-	-	3.30
L4col b	-	2.53	3.89
L5	1.85	1.41	1.76
Am b	4.03	3.16	1.93
Am l 1	2.91	3.37	3.05
Am l 2	2.98	3.75	2.63
Am l 3	4.80	4.23	2.39
Am g	2.98	3.08	1.71
Am a	4.28	3.74	2.34
C2	3.56	1.37	1.30
C3	2.62	3.14	1.67
T1 a	2.26	1.61	-
T1 b	2.20	1.97	-
T1 c	2.14	2.15	-
T1 d	2.80	1.99	-
T1 e	2.62	2.28	-
T1 f	2.47	1.81	-

Element	Radius ($10^{-1}\mu m$)		
	Distal	Central	Proximal
La wf a	2.59	-	-
La wf b	3.99	-	-
La wf c	4.00	-	-
La wf d	2.30	-	-
La wf e	3.22	-	-
La wf f	4.79	-	-
La wf g	4.27	-	-
La wf h	2.50	-	-
La wf i	2.50	-	-
La wf j	3.36	-	-
La wf k	3.83	-	-

Table D.1: Sizes of the elements in the 3D model

Appendix E

3D connectivity matrices

	R1	R2	R3	R4	R5	R6	L1	L2	L3	L4	L5	Am b	Am l 1	Am l 2	Am l 3	Am g	Am a	C2
R1	0	0	0	0	0	10	12	6	0	0	0	0	0	0	0	1	0	0
R2	0	0	0	0	0	13	12	7	0	0	1	1	0	0	0	0	0	0
R3	0	0	0	0	0	7	7	3	0	0	0	0	1	0	0	0	0	0
R4	0	0	0	0	0	7	8	2	0	0	0	0	1	1	0	0	0	0
R5	0	0	0	0	0	7	6	1	0	0	0	0	0	2	0	0	0	1
R6	0	0	0	0	0	10	11	5	0	0	0	0	0	0	0	1	0	0
L1	10	13	7	7	7	10	0	0	0	0	0	0	0	0	0	0	0	0
L2	12	12	7	8	6	11	0	0	0	0	0	0	0	0	0	0	0	6
L3	6	7	3	2	1	5	0	0	0	0	0	1	0	1	0	0	0	0
L4	0	0	0	0	0	0	0	0	0	0	0	0	0	1	0	0	0	0
L5	0	0	0	0	0	0	0	0	0	0	0	0	0	1	0	0	0	0
Am b	0	1	0	0	0	0	0	0	0	0	0	0	0	0	0	0	0	1
Am l 1	0	1	0	0	0	0	0	1	0	0	0	0	0	0	0	0	0	1
Am l 2	0	0	1	1	0	0	0	0	0	0	0	0	0	0	0	0	0	2
Am l 3	0	0	0	1	2	0	0	1	1	1	0	0	0	0	0	0	0	0
Am g	0	0	0	0	0	0	0	0	0	0	0	0	0	0	0	0	0	1
Am a	1	0	0	0	1	0	0	0	0	0	1	0	0	0	0	0	1	0
C2	0	0	0	0	0	0	6	0	0	0	0	0	2	0	0	1	0	0
C3	0	0	0	0	0	0	0	0	0	0	0	1	1	0	0	0	0	0
Tl a	0	0	0	0	0	0	0	0	0	0	2	0	0	0	0	0	0	0
Tl b	0	1	0	0	0	0	0	0	0	0	0	1	0	0	0	0	0	0
Tl c	0	0	1	1	0	0	0	0	0	0	0	0	1	0	0	0	0	0
Tl d	0	0	0	0	0	0	0	0	0	0	0	0	0	3	0	0	0	0
Tl e	0	0	0	0	0	0	0	0	0	0	0	0	0	0	0	0	0	0
Tl f	0	0	0	0	0	0	0	0	0	0	1	0	0	0	0	3	0	0
La wf a	0	1	0	0	0	1	1	2	0	0	0	0	0	0	0	0	1	0
La wf b	0	1	0	0	0	0	1	2	0	0	0	0	0	0	0	0	1	0
La wf c	0	0	0	0	0	0	0	1	0	0	0	0	0	1	2	1	3	3
La wf d	0	0	1	0	0	0	2	1	0	0	0	0	0	0	0	0	0	0
La wf e	0	0	0	0	0	0	0	0	0	1	0	0	0	4	0	0	0	0
La wf f	0	0	0	0	0	0	0	1	0	0	1	0	0	2	0	1	1	1
La wf g	0	0	0	0	0	0	0	4	0	0	3	0	0	4	2	1	2	2
La wf h	0	1	0	0	0	0	2	1	0	0	0	0	1	0	0	0	0	0
La wf i	0	0	0	0	0	0	0	3	0	0	0	0	0	0	1	0	0	0
La wf j	0	0	0	1	0	1	3	4	0	0	0	0	0	0	0	0	0	1
La wf k	2	0	0	0	0	0	0	2	0	0	0	0	0	0	0	0	0	0

Table E.1: Symmetric connectivity matrix for distal layer in the 3D model (Part A)

	C3	T1 1	T1 2	T1 3	T1 4	T1 5	T1 6	Lawf a	Lawf b	Lawf c	Lawf d	Lawf e	Lawf f	Lawf g	Lawf h	Lawf i	Lawf j	Lawf k
R1	0	0	0	0	0	0	0	0	0	0	0	0	0	0	0	0	0	2
R2	0	0	1	0	0	0	0	1	1	0	0	0	0	0	1	0	0	0
R3	0	0	0	1	0	0	0	0	0	0	1	0	0	0	0	0	0	0
R4	0	0	0	1	0	0	0	0	0	0	0	0	0	0	0	0	1	0
R5	0	0	0	0	0	0	0	0	0	0	0	0	0	0	0	0	0	0
R6	0	0	0	0	0	0	0	0	0	0	0	0	0	0	0	0	1	0
L1	0	0	0	0	0	0	0	1	0	0	0	0	0	0	0	0	1	0
L2	0	0	0	0	0	0	0	1	1	0	2	0	0	0	2	0	3	0
L3	0	0	0	0	0	0	0	2	2	1	1	0	1	4	1	3	4	2
L4	0	0	0	0	0	0	0	0	0	0	0	0	0	0	0	0	0	0
L5	0	0	0	0	0	0	0	0	0	0	0	1	0	0	0	0	0	0
Am b	0	2	0	0	0	0	1	0	0	0	0	0	1	3	0	0	0	0
Am l 1	1	0	1	0	0	0	0	0	0	0	0	0	0	0	0	0	0	0
Am l 2	1	0	0	1	0	0	0	0	0	0	0	0	0	0	1	0	0	0
Am l 3	0	0	0	0	3	0	0	0	0	1	0	4	2	4	0	0	0	0
Am g	0	0	0	0	0	0	0	0	0	2	0	0	0	2	0	1	0	0
Am a	0	0	0	0	0	0	3	0	1	1	0	0	1	1	0	0	0	0
C2	0	0	0	0	0	0	0	0	0	3	0	0	1	2	0	0	1	0
C3	0	0	0	0	0	0	0	0	0	0	0	0	2	0	0	0	0	0
T1 a	0	0	0	0	0	0	0	0	0	0	0	0	0	0	0	0	0	0
T1 b	0	0	0	0	0	0	0	0	0	0	0	0	0	0	0	0	0	0
T1 c	0	0	0	0	0	0	0	0	1	0	0	0	0	0	0	0	0	0
T1 d	0	0	0	0	0	0	0	0	0	1	0	0	0	0	0	0	0	0
T1 e	0	0	0	0	0	0	0	0	0	0	0	0	0	0	0	0	1	0
T1 f	0	0	0	0	0	0	0	0	0	0	0	0	0	0	0	0	0	0
La wf a	0	0	0	0	0	0	0	0	0	0	0	0	0	0	0	0	0	0
La wf b	0	0	0	1	0	0	0	0	0	0	0	0	0	1	0	0	0	0
La wf c	0	0	0	0	1	0	0	0	0	0	0	0	1	0	0	0	0	0
La wf d	0	0	0	0	0	0	0	0	0	0	0	1	0	0	1	0	0	0
La wf e	0	0	0	0	0	0	0	0	0	0	1	0	0	0	0	0	2	0
La wf f	2	0	0	0	0	0	0	0	0	1	0	0	0	1	0	0	0	0
La wf g	0	0	0	0	0	0	0	0	1	0	0	0	1	0	0	0	0	0
La wf h	0	0	0	0	0	0	0	0	0	0	1	0	0	0	0	0	0	0
La wf i	0	0	0	0	0	0	0	0	0	0	0	0	0	0	0	0	0	0
La wf j	0	0	0	0	0	1	0	0	0	0	0	2	0	0	0	0	0	0
La wf k	0	0	0	0	0	0	0	0	0	0	0	0	0	0	0	0	0	0

Table E.2: Symmetric connectivity matrix for distal layer in the 3D model (Part B)

Table E.3: Symmetric connectivity matrix for central layer in the 3D model (Part A)

	R1	R2	R3	R4	R5	R6	L1	L2	L3	L4	L4col b	L5	Am b
R1	0	0	0	0	0	0	22	26	4	0	0	0	14
R2	0	0	0	0	0	0	21	23	3	0	0	0	11
R3	0	0	0	0	0	0	23	23	1	0	0	0	0
R4	0	0	0	0	0	0	23	24	4	0	0	0	0
R5	0	0	0	0	0	0	21	23	3	0	1	0	0
R6	0	0	0	0	0	0	25	27	5	0	0	0	1
L1	22	21	23	23	21	25	0	0	0	0	0	0	1
L2	26	23	23	24	23	27	0	0	0	0	1	0	1
L3	4	3	1	4	3	5	0	0	0	0	0	0	1
L4	0	0	0	0	0	0	0	0	0	0	1	0	0
L4col b	0	0	0	0	1	0	0	1	0	1	0	0	0
L5	0	0	0	0	0	0	0	0	0	0	0	0	0
Am b	14	11	0	0	0	1	0	1	1	0	0	0	0
Am l 1	0	17	13	0	0	0	0	1	0	0	0	0	0
Am l 2	0	0	15	9	0	0	0	0	1	0	0	0	0
Am l 3	0	0	0	11	18	2	0	0	1	0	0	2	0
Am g	0	0	0	5	6	11	0	0	4	3	0	0	0
Am a	14	1	0	0	0	14	0	1	1	0	0	0	0
C2	0	0	0	0	0	0	0	0	0	0	0	1	0
C3	0	0	2	0	0	0	6	8	1	0	0	0	1
T1 a	0	0	0	0	0	0	0	0	0	0	0	0	6
T1 b	0	1	0	0	0	0	0	0	0	0	0	0	0
T1 c	0	0	1	1	0	0	0	0	0	0	0	0	0
T1 d	0	0	0	0	0	0	0	0	0	0	0	0	0
T1 e	0	0	0	0	0	0	0	0	0	0	0	0	0
T1 f	0	0	0	0	0	0	0	0	0	0	0	0	0

	Am l 1	Am l 2	Am l 3	Am g	Am a	C2	C3	T1 1	T1 2	T1 3	T1 4	T1 5	T1 6
R1	0	0	0	0	14	0	0	0	0	0	0	0	0
R2	17	0	0	0	1	0	0	0	1	0	0	0	0
R3	13	15	0	0	0	0	2	0	0	1	0	0	0
R4	0	9	11	5	0	0	0	0	0	1	0	0	0
R5	0	0	18	6	0	0	0	0	0	0	0	0	0
R6	0	0	2	11	14	0	0	0	0	0	0	0	0
L1	0	0	0	0	0	0	6	0	0	0	0	0	0
L2	1	0	0	0	1	0	8	0	0	0	0	0	0
L3	0	1	1	4	1	0	1	0	0	0	0	0	0
L4	0	0	0	3	0	0	0	0	0	0	0	0	0
L4col b	0	0	0	0	0	0	0	0	0	0	0	0	0
L5	0	0	2	0	0	1	0	0	0	0	0	0	0
Am b	0	0	0	0	0	0	1	6	0	0	0	0	0
Am l 1	0	0	0	0	0	0	3	0	5	0	0	0	0
Am l 2	0	0	0	0	0	0	3	0	0	6	0	0	0
Am l 3	0	0	0	0	0	0	3	0	0	0	6	3	0
Am g	0	0	0	0	0	0	4	0	0	0	0	3	0
Am a	0	0	0	0	0	0	5	0	0	0	0	0	10
C2	0	0	0	0	0	0	0	0	0	0	0	0	0
C3	3	3	3	4	5	0	0	0	1	1	0	0	0
T1 a	0	0	0	0	0	0	0	0	0	0	0	0	0
T1 b	5	0	0	0	0	0	1	0	0	0	0	0	0
T1 c	0	6	0	0	0	0	1	0	0	0	0	0	0
T1 d	0	0	6	0	0	0	0	0	0	0	0	0	0
T1 e	0	0	3	3	0	0	0	0	0	0	0	0	0
T1 f	0	0	0	0	10	0	0	0	0	0	0	0	0

Table E.4: Symmetric connectivity matrix for central layer in the 3D model (Part B)

	R1	R2	R3	R4	R5	R6	L1	L2	L3	L4	L4col a	L4col b	L5	Am b	Am l 1	Am l 2	Am l 3	Am g	Am a	C2	C3
R1	0	0	0	0	0	8	9	1	0	1	1	0	5	0	0	0	0	3	0	0	0
R2	0	0	0	0	0	9	12	0	0	0	1	0	4	5	0	0	0	0	0	0	0
R3	0	0	0	0	0	8	10	0	0	2	2	0	0	5	4	0	0	0	0	0	1
R4	0	0	0	0	0	8	10	2	0	1	1	0	0	0	6	6	0	0	0	0	0
R5	0	0	0	0	0	10	10	2	1	0	2	0	0	0	0	7	0	0	0	0	0
R6	0	0	0	0	0	11	11	3	2	2	2	0	0	0	0	0	3	7	0	0	0
L1	8	9	8	8	10	11	0	3	0	2	0	0	0	1	0	0	0	0	0	0	0
L2	9	12	10	10	10	11	3	0	0	9	11	7	1	0	0	0	0	1	0	0	1
L3	1	0	0	2	2	3	0	0	0	0	1	1	0	0	0	1	1	0	0	0	0
L4	0	0	0	0	1	2	9	0	0	0	2	2	0	0	0	0	1	0	0	0	0
L4col a	1	0	2	1	0	2	11	1	2	0	2	4	0	0	0	0	0	0	0	0	0
L4col b	1	1	2	1	2	2	7	1	2	4	0	2	0	0	0	0	0	0	0	0	0
L5	0	0	0	0	0	0	1	0	2	3	2	0	0	0	0	1	0	0	0	0	0
Am b	5	4	0	0	0	0	0	0	0	0	0	0	0	0	0	0	0	0	0	0	0
Am l 1	0	5	5	0	0	1	0	0	0	0	0	0	0	0	0	0	0	0	0	0	1
Am l 2	0	0	4	6	0	0	0	0	0	0	0	0	0	0	0	0	0	0	0	0	0
Am l 3	0	0	0	6	7	0	0	1	0	0	0	1	0	0	0	0	0	0	0	0	0
Am g	0	0	0	0	3	0	0	1	1	0	0	0	0	0	0	0	0	0	0	0	0
Am a	3	0	0	0	7	0	1	0	0	1	0	0	0	0	0	1	0	0	0	0	0
C2	0	0	0	0	0	0	0	0	0	0	0	0	0	0	0	0	0	0	0	0	0
C3	0	0	1	0	0	0	1	0	0	0	0	0	0	1	0	0	0	0	0	0	0

Table E.5: Symmetric connectivity matrix for proximal layer in the 3D model.

Bibliography

[1] S. R. y Cajal. *Textura del sistema nervioso del hombre y de los vertebrados*. Nicolás Moya, Madrid (Spanish), 1899.

[2] D. B. Chklovskii and A. Koulakov. A wire length minimization approach to ocular dominance patterns in mammalian visual cortex. *Physica A*, 284, 1-4:318–334, 2000.

[3] D. B. Chklovskii, T. Schikorski, and C. F. Stevens. Wiring optimization in cortical circuits. *Neuron*, 34(3):341–347, 2002.

[4] V. A. Klyachko and F. Stevens. Connectivity optimization and the positioning of cortical areas. *Proceedings of the National Academy of Sciences of the United States of America*, 100(13):7937–7141, 2003.

[5] C. Cherniak, Z. Mokhtarzada, R. Rodriguez-Esteban, and K. Changizi. Global optimization of cerebral cortex layout. *Proceedings of the National Academy of Sciences of the United States of America*, 101(4):1081–1086, 2004.

[6] G. Buzsaki, C. Geisler, D. A. Henze, and X.-J. Wang. Interneuron diversity series: Circuit complexity and axon wiring economy of cortical interneurons. *Trends in neurosciences*, 27(4):186–193, 2004.

[7] D. B. Chklovskii. Synaptic connectivity and neuronal morphology: two sides of the same coin. *Neuron*, 43(5):609–617, 2004.

[8] D. B. Chklovskii. Exact solution for the optimal neuronal layout problem. *Neural Comput*, 16(10):2067–2078, 2004.

[9] B. L. Chen, D. H. Hall, and D. B. Chklovskii. Wiring optimization can relate neuronal structure and function. *Proc Natl Acad Sci U S A*, 103(12):4723–4728, 2006.

[10] A. Pérez-Escudero and G. G. de Polavieja. Optimally wired subnetwork determines neuroanatomy of caenorhabditis elegans. *Proc Natl Acad Sci U S A*, 104(43):17180–17185, 2007.

[11] A. Pérez-Escudero, M. Rivera-Alba, and G. G. de Polavieja. Structure of deviations from optimality in biological systems. *Proc Natl Acad Sci U S A*, 106(48):20544–20549, 2009.

[12] V. Braitenberg. Patterns of projection in the visual system of the fly. i. retina-lamina projections. *Exp Brain Res*, 3(3):271–298, 1967.

[13] I. A. Meinertzhagen and S. D. O'Neil. Synaptic organization of columnar elements in the lamina of the wild type in *Drosophila melanogaster*. *J Comp Neurol*, 305(2):232–263, 1991.

[14] I. A. Meinertzhagen and K. E. Sorra. Synaptic organization in the fly's optic lamina: few cells, many synapses and divergent microcircuits. *Prog Brain Res*, 131:53–69, 2001.

[15] M. Helmstaedter, K. L. Briggman, and W. Denk. 3d structural imaging of the brain with photons and electrons. *Curr Opin Neurobiol*, 18(6):633–641, 2008.

[16] D. B. Chklovskii, S. Vitaladevuni, and L. K. Scheffer. Semi-automated reconstruction of neural circuits using electron microscopy. *Curr Opin*

Neurobiol, 20(5):667–675, 2010.

[17] H. Cuntz, F. Forstner, A. Borst, and M. Hüsser. One rule to grow them all: a general theory of neuronal branching and its practical application. *PLoS Comput Biol*, 6(8), 2010.

[18] J. G. White. The structure of the nervous system of the nematode caenorhabditis elegans. *Philosophical Transactions of the Royal Society B: Biological Sciences*, 314(1165):1–, 1986.

[19] M. Heisenberg. Mushroom body memoir: from maps to models. *Nat Rev Neurosci*, 4(4):266–275, 2003.

[20] S. R. y Cajal and D. Sánchez. *Contribución al conocimiento de los centros nerviosos de los insectos*. Nicolás Moya, Madrid (Spanish), 1915.

[21] S. Gao, S.-Y. Takemura, C.-Y. Ting, S. Huang, Z. Lu, H. Luan, J. Rister, A. S. Thum, M. Yang, S.-T. Hong, J. W. Wang, W. F. Odenwald, B. H. White, I. A. Meinertzhagen, and C.-H. Lee. The neural substrate of spectral preference in drosophila. *Neuron*, 60(2):328–342, 2008.

[22] K.-F. Fischbach and A. P. M. Dittrich. The optic lobe of *Drosophila melanogaster*. i. a golgi analysis of wild-type structure. *Cell and Tissue Research*, 258:441–475, 1989. 10.1007/BF00218858.

[23] W. Reichardt. *Autocorrelation, a principle for the evaluation of sensory information by the central nervous system*. New York/London: MIT Press/Wiley, 1961.

[24] A. Borst, J. Haag, and D. F. Reiff. Fly motion vision. *Annu Rev Neurosci*, 33:49–70, 2010.

[25] M. Juusola, A. S. French, R. O. Uusitalo, and M. Weckström. Information processing by graded-potential transmission through tonically

active synapses. *Trends Neurosci*, 19(7):292–297, 1996.

[26] L. Zheng, G. G. de Polavieja, V. Wolfram, M. H. Asyali, R. C. Hardie, and M. Juusola. Feedback network controls photoreceptor output at the layer of first visual synapses in drosophila. *J Gen Physiol*, 127(5):495–510, 2006.

[27] L. Zheng, A. Nikolaev, T. J. Wardill, C. J. O'Kane, G. G. de Polavieja, and M. Juusola. Network adaptation improves temporal representation of naturalistic stimuli in drosophila eye: I dynamics. *PLoS One*, 4(1):e4307, 2009.

[28] A. Nikolaev, L. Zheng, T. J. Wardill, C. J. O'Kane, G. G. de Polavieja, and M. Juusola. Network adaptation improves temporal representation of naturalistic stimuli in drosophila eye: Ii mechanisms. *PLoS One*, 4(1):e4306, 2009.

[29] S. B. Laughlin. Form and function in retinal processing. *Trends Neurosci*, 10:478–483, 1987.

[30] M. V. Srinivasan, S. B. Laughlin, and A. Dubs. Predictive coding: a fresh view of inhibition in the retina. *Proc R Soc Lond B Biol Sci*, 216(1205):427–459, 1982.

[31] J. H. Van Hatered. Theoretical predictions of spatiotemporal receptive-fields of fly lmcs, and experimental validation. *J Comp Physiol A Neuroethol Sens Neural Behav Physiol*, 171:157–170, 1992.

[32] J. Rister, D. Pauls, B. Schnell, C.-Y. Ting, C.-H. Lee, I. Sinakevitch, J. Morante, N. J. Strausfeld, K. Ito, and M. Heisenberg. Dissection of the peripheral motion channel in the visual system of drosophila melanogaster. *Neuron*, 56(1):155–170, 2007.

[33] D. F. Reiff, J. Plett, M. Mank, O. Griesbeck, and A. Borst. Visualizing

retinotopic half-wave rectified input to the motion detection circuitry of drosophila. *Nat Neurosci*, 13(8):973–978, 2010.

[34] J. E. Niven, J. C. Anderson, and S. B. Laughlin. Fly photoreceptors demonstrate energy-information trade-offs in neural coding. *PLoS Biol*, 5(4):e116, 2007.

[35] T. N. Edwards and I. A. Meinertzhagen. The functional organisation of glia in the adult brain of drosophila and other insects. *Prog Neurobiol*, 90(4):471–497, 2010.

[36] D. Hadjieconomou, K. Timofeev, and I. Salecker. A step-by-step guide to visual circuit assembly in drosophila. *Current Opinion in Neurobiology*, 21(1):76 – 84, 2011.

[37] S. E. Perez and H. Steller. Migration of glial cells into retinal axon target field in drosophila melanogaster. *J Neurobiol*, 30(3):359–373, 1996.

[38] B. Poeck, S. Fischer, D. Gunning, S. L. Zipursky, and I. Salecker. Glial cells mediate target layer selection of retinal axons in the developing visual system of drosophila. *Neuron*, 29(1):99–113, 2001.

[39] T. R. Clandinin and S. L. Zipursky. Making connections in the fly visual system. *Neuron*, 35(5):827–841, 2002.

[40] J. Morante and C. Desplan. Building a projection map for photoreceptor neurons in the drosophila optic lobes. *Semin Cell Dev Biol*, 15(1):137–143, 2004.

[41] P. R. Hiesinger, R. G. Zhai, Y. Zhou, T.-W. Koh, S. Q. Mehta, K. L. Schulze, Y. Cao, P. Verstreken, T. R. Clandinin, K.-F. Fischbach, I. A. Meinertzhagen, and H. J. Bellen. Activity-independent prespecification of synaptic partners in the visual map of drosophila. *Curr Biol*,

16(18):1835–1843, 2006.

[42] T. R. Clandinin and S. L. Zipursky. Afferent growth cone interactions control synaptic specificity in the drosophila visual system. *Neuron*, 28(2):427–436, 2000.

[43] R. C. Lee, T. R. Clandinin, C.-H. Lee, P.-L. Chen, I. A. Meinertzhagen, and S. L. Zipursky. The protocadherin flamingo is required for axon target selection in the drosophila visual system. *Nat Neurosci*, 6(6):557–563, 2003.

[44] Pei-Ling Chen and Thomas R Clandinin. The cadherin flamingo mediates level-dependent interactions that guide photoreceptor target choice in drosophila. *Neuron*, 58(1):26–33, Apr 2008.

[45] G. A. Horridge and I. A. Meinertzhagen. The accuracy of the patterns of connections of the first- and second-order neurons of the visual system of *Calliphora*. *Proc Roy Soc Lond B*, 175:6982, 1970.

[46] A. Fröhlich and I. A. Meinertzhagen. Regulation of synaptic frequency: comparison of the effects of hypoinnervation with those of hyperinnervation in the fly's compound eye. *J Neurobiol*, 18(4):343–357, 1987.

[47] C. B. Boschek. On the fine structure of the peripheral retina and lamina ganglionaris of the fly, musca domestica. *Z Zellforsch Mikrosk Anat*, 118(3):369–409, 1971.

[48] A. Kolodziejczyk, X. Sun, I. A. Meinertzhagen, and D. R. Nässel. Glutamate, gaba and acetylcholine signaling components in the lamina of the drosophila visual system. *PLoS One*, 3(5):e2110, 2008.

[49] S. V. Raghu and A. Borst. Candidate glutamatergic neurons in the visual system of ¡italic¿drosophila¡/italic¿. *PLoS ONE*, 6(5):e19472, 2011.

[50] C. Gengs, H.-T. Leung, D. R. Skingsley, M. I. Iovchev, Z. Yin, E. P. Semenov, M. G. Burg, R. C. Hardie, and W. L. Pak. The target of drosophila photoreceptor synaptic transmission is a histamine-gated chloride channel encoded by ort (hcla). *J Biol Chem*, 277(44):42113–42120, 2002.

[51] A. Pantazis, A. Segaran, C.-H. Liu, A. Nikolaev, J. Rister, A. S. Thum, T. Roeder, E. Semenov, M. Juusola, and R. C. Hardie. Distinct roles for two histamine receptors (hcla and hclb) at the drosophila photoreceptor synapse. *J Neurosci*, 28(29):7250–7259, 2008.

[52] S. J. Sims and E. R. Macagno. Computer reconstruction of all the neurons in the optic ganglion of daphnia magna. *J Comp Neurol*, 233(1):12–29, 1985.

[53] S.-Y. Takemura, Z. Lu, and I. A. Meinertzhagen. Synaptic circuits of the drosophila optic lobe: the input terminals to the medulla. *J Comp Neurol*, 509(5):493–513, 2008.

[54] C. Golgi. Sulla sostanza grigia del cervello. *Gazzeta medica italiana*, 1:91–98, 1873.

[55] J. Livet, T. A. Weissman, H. Kang, R. W. Draft, J. Lu, R. A. Bennis, J. R. Sanes, and J. W. Lichtman. Transgenic strategies for combinatorial expression of fluorescent proteins in the nervous system. *Nature*, 450(7166):56–62, 2007.

[56] Jeff W Lichtman, Jean Livet, and Joshua R Sanes. A technicolour approach to the connectome. *Nat Rev Neurosci*, 9(6):417–422, 2008.

[57] S. Hampel, P. Chung, C. E. McKellar, D. Hall, L. L. Looger, and J. H. Simpson. Drosophila brainbow: a recombinase-based fluorescence labeling technique to subdivide neural expression patterns. *Nat Meth*,

8(3):253–259, 2011.

[58] D. Hadjieconomou, S. Rotkopf, C. Alexandre, D. M. Bell, B. J. Dickson, and I. Salecker. Flybow: genetic multicolor cell labeling for neural circuit analysis in *Drosophila melanogaster*. *Nat Methods*, 2011.

[59] A. Peters and M. L. Feldman. The projection of the lateral geniculate nucleus to area 17 of the rat cerebral cortex. i. general description. *J Neurocytol*, 5(1):63–84, 1976.

[60] V. Braitenberg and A. Schüz. *Cortex: statistics and geometry of neuronal connectivity*. Belin: Springer, 1998.

[61] A. Stepanyants and D. B. Chklovskii. Neurogeometry and potential synaptic connectivity. *Trends Neurosci*, 28(7):387–394, 2005.

[62] Y. Mishchenko, T. Hu, J. Spacek, J. Mendenhall, K. M. Harris, and D. B. Chklovskii. Ultrastructural analysis of hippocampal neuropil from the connectomics perspective. *Neuron*, 67(6):1009–1020, 2010.

[63] E. H. Feinberg, M. K. Vanhoven, A. Bendesky, G. Wang, R. D. Fetter, K. Shen, and C. I. Bargmann. Gfp reconstitution across synaptic partners (grasp) defines cell contacts and synapses in living nervous systems. *Neuron*, 57(3):353–363, 2008.

[64] Y. Mishchenko. Reconstruction of complete connectivity matrix for connectomics by sampling neural connectivity with fluorescent synaptic markers. *J Neurosci Methods*, 196(2):289–302, 2011.

[65] K. J. Hayworth, N. Kasthuri, R. Schalek, and J. W. Lichtman. Automating the collection of ultrathin serial sections for large volume tem reconstructions. *Microscopy and Microanalysis*, 12(Supplement):86–87, 2006.

[66] W. Denk and H. Horstmann. Serial block-face scanning electron mi-

croscopy to reconstruct three-dimensional tissue nanostructure. *PLoS Biol*, 2(11):e329, 2004.

[67] G. Knott, H. Marchman, D. Wall, and B. Lich. Serial section scanning electron microscopy of adult brain tissue using focused ion beam milling. *J Neurosci*, 28(12):2959–2964, 2008.

[68] Y. Mishchenko. Automation of 3d reconstruction of neural tissue from large volume of conventional serial section transmission electron micrographs. *J Neurosci Methods*, 176(2):276–289, 2009.

[69] A. Cardona, S. Saalfeld, S. Preibisch, B. Schmid, A. Cheng, J. Pulokas, P. Tomancak, and V. Hartenstein. An integrated micro- and macroarchitectural analysis of the drosophila brain by computer-assisted serial section electron microscopy. *PLoS Biol*, 8(10), 2010.

[70] M. Hortsch. *The Sticky Synapse. A short history of the synapse - Golgi versus Ramón y Cajal*. Springer, 2009.

[71] T. Binzegger, R. J. Douglas, and K. A. C. Martin. A quantitative map of the circuit of cat primary visual cortex. *J Neurosci*, 24(39):8441–8453, 2004.

[72] A. Stepanyants, J. A. Hirsch, L. M. Martinez, Z. F. Kisvárday, A. S. Ferecskó, and D. B. Chklovskii. Local potential connectivity in cat primary visual cortex. *Cereb Cortex*, 18(1):13–28, 2008.

[73] K. L. Briggman and W. Denk. Towards neural circuit reconstruction with volume electron microscopy techniques. *Curr Opin Neurobiol*, 16(5):562–570, 2006.

[74] S. J. Smith. Circuit reconstruction tools today. *Curr Opin Neurobiol*, 17(5):601–608, 2007.

[75] L. Luo, E. M. Callaway, and K. Svoboda. Genetic dissection of neural

circuits. *Neuron*, 57(5):634–660, 2008.

[76] E. Jurrus, R. Whitaker, B. W. Jones, R. Marc, and T. Tasdizen. An optimal-path approach for neural circuit reconstruction. *Proc IEEE Int Symp Biomed Imaging*, 2008(4541320):1609–1612, 2008.

[77] J. R. Anderson, B. W. Jones, J.-H. Yang, M. V. Shaw, C. B. Watt, P. Koshevoy, J. Spaltenstein, E. Jurrus, K. U. V., R. T. Whitaker, D. Mastronarde, T. Tasdizen, and R. E. Marc. A computational framework for ultrastructural mapping of neural circuitry. *PLoS Biol*, 7(3):e1000074, 2009.

[78] G. von Bonin and W. R. Mehler. On columnar arrangement of nerve cells in cerebral cortex. *Brain Res*, 27(1):1–9, 1971.

[79] C. S. Potter, H. Chu, B. Frey, C. Green, N. Kisseberth, T. J. Madden, K. L. Miller, K. Nahrstedt, J. Pulokas, A. Reilein, D. Tcheng, D. Weber, and B. Carragher. Leginon: A system for fully automated acquisition of 1000 electron micrographs a day. *Ultramicroscopy*, 77 (3-4):153–161, 1999.

[80] D. J. Olbris, P. Winston, and Chklovskii D. B. Raveler a software for editing large segmented electron microscopy datasets. *In preparation.*

[81] B. Schmid, J. Schindelin, A. Cardona, M. Longair, and M. Heisenberg. A high-level 3d visualization api for java and imagej. *BMC Bioinformatics*, 11:274, 2010.

[82] E. Pyza and I. A. Meinertzhagen. Daily rhythmic changes of cell size and shape in the first optic neuropil in drosophila melanogaster. *J Neurobiol*, 40(1):77–88, 1999.

[83] M. Barth. Circadian plasticity in photoreceptor cells controls visual coding efficiency in drosophila melanogaster. *PLoS ONE*, 5(2):e9217–,

2010.

[84] J. Görska-Andrzejak, A. Keller, T. Raabe, L. Kilianek, and E. Pyza. Structural daily rhythms in gfp-labelled neurons in the visual system of drosophila melanogaster. *Photochem Photobiol Sci*, 4(9):721–726, Sep 2005.

[85] N. J. Strausfeld and J. A. Campos-Ortega. Vision in insects: pathways possibly underlying neural adaptation and lateral inhibition. *Science*, 195(4281):894–897, 1977.

[86] I. A. Meinertzhagen. Ultrastructure and quantification of synapses in the insect nervous system. *J Neurosci Methods*, 69(1):59–73, 1996.

[87] W. A. Ribi. Gap junctions coupling photoreceptor axons in the first optic ganglion of the fly. *Cell Tissue Res*, 195(2):299–308, 1978.

[88] M. Joesch, B. Schnell, S. V. Raghu, D. F. Reiff, and A. Borst. On and off pathways in drosophila motion vision. *Nature*, 468(7321):300–304, 2010.

[89] J. E. Lennard-Jones. On the determination of molecular fields. *Proc Roy Soc Lond A*, 106:436–477, 1924.

[90] S. Kirkpatrick, C. D. Jr. Gelatt, and M. P. Vecchi. Optimization by simulated annealing. *Science*, 220:671–680, 1983.